Historical Pattern Effects and Climate Sensitivity Revisited with Novel Constraints on Past Warming Patterns

Vincent T. Cooper,[a] Kyle C. Armour,[b,c] Jonathan M. Gregory,[d,e] Timothy Andrews,[e,f] Moritz Günther,[g] Chongxing Fan[h]

[a] *Department of Earth, Atmospheric, and Planetary Sciences, Massachusetts Institute of Technology, Cambridge, MA, USA*
[b] *Department of Atmospheric and Climate Science, University of Washington, Seattle, WA, USA*
[c] *School of Oceanography, University of Washington, Seattle, WA, USA*
[d] *National Centre for Atmospheric Science, University of Reading, UK*
[e] *Met Office Hadley Centre, Exeter, UK*
[f] *School of Earth, Environment and Sustainability, University of Leeds, Leeds, UK*
[g] *Climate Dynamics Department, Max Planck Institute for Meteorology, Hamburg, Germany*
[h] *Atmospheric and Oceanic Sciences Program, Princeton University, Princeton, New Jersey, USA*

ABSTRACT: The historical record (1850–present) can constrain equilibrium climate sensitivity (ECS) only if we know the patterns of sea-surface temperature (SST) and sea ice concentration (SIC) that shape radiative feedbacks. Feedbacks depend on spatial patterns of SST and SIC ("pattern effects"), yet the impact of historical SST/SIC uncertainty on feedback estimates has not been systematically quantified. Here we use a new coupled reanalysis of SST/SIC to quantify feedbacks over 1850–2023. We prescribe 3–14 ensemble members of SST/SIC in six atmospheric models with constant preindustrial forcings. Compared to previous estimates, our ensemble-mean feedbacks vary less over time and are consistent with coupled models' *abrupt-4xCO$_2$* feedbacks over 1901–1960. With this context, the strongly stabilizing feedback over 1975–2014 is even more anomalous than previously identified. Importantly, feedbacks have become less stabilizing since 2014 in simulations and observations, but this development has little impact on feedbacks over the full record. From anomalies over 2006–2023 relative to 1850–1900, we estimate a pattern effect (i.e., the long-term 2xCO$_2$ feedback minus the historical feedback) of 0.62 W m^{-2} K^{-1} (−0.05 to 1.03, 5–95%). SST/SIC tends to be a larger source of pattern-effect uncertainty than intermodel spread. Revising historical constraints on ECS through 2023 (including increases in global warming, Earth's energy imbalance, and radiative forcing) yields a maximum likelihood of 3.4 K from the historical record alone, and combining lines of evidence yields a median of 2.8 K (2.1–3.9 K, 5–95%; approximate robust upper bound at 4.4 K).

SIGNIFICANCE STATEMENT: Historical constraints on climate sensitivity depend on the patterns of change in sea-surface temperature (SST) and sea ice since the 1800s. Using a new ensemble reconstruction of these changes, we find that SST and sea ice tend to be the largest source of uncertainty in the historical pattern effect, i.e., the difference between historical feedbacks and the expected long-term response to CO$_2$ forcing. Recent warming patterns make feedbacks less stabilizing over 2001–2023, but feedbacks over the full historical record remain more stabilizing than the long-term response to CO$_2$. Thus, climate sensitivity estimates from historical warming must still be adjusted upward for pattern effects, and historical evidence remains consistent with climate sensitivity near 3 K.

1. Introduction

The historical record (c. 1850–present) of changes in Earth's energy budget is a nuanced line of evidence for equilibrium climate sensitivity (ECS), which is the long-term change in global-mean surface temperature from a sustained doubling of atmospheric CO$_2$ relative to preindustrial levels. Historical warming is influenced by natural variability, ocean heat uptake, and the transient evolution of historical forcings, including contributions from non-CO$_2$ forcing agents. However, changes in the historical energy budget can constrain ECS if these influences are accounted for. To estimate ECS from the historical record, we use the standard energy-balance model of perturbations to the global energy budget (Gregory et al. 2002),

$$\Delta N = \Delta F + \lambda \Delta T, \tag{1}$$

where N is the net top-of-atmosphere (TOA) radiation (units W m^{-2}), F is the effective radiative forcing, λ is the net radiative feedback (units W m^{-2} K^{-1}), and T is the near-surface air temperature. ΔN, ΔF, and ΔT are global-mean anomalies from a reference state, and λ is defined as negative for a stable climate. From Eq. (1), we can estimate the historical feedback (λ_{Hist}) from observational estimates of ΔN, ΔF, and ΔT.

ECS is defined using Eq. (1), with $\Delta N = 0$ at equilibrium:

$$\mathrm{ECS} = -\Delta F_{2\mathrm{xCO}_2} / \lambda_{2\mathrm{xCO}_2}, \tag{2}$$

where the 2xCO$_2$ subscript denotes that ΔF and λ arise from doubling CO$_2$. In the past, λ was commonly as-

Corresponding author: Vincent T. Cooper, vcooper@mit.edu

sumed to be approximately constant, i.e., $\lambda_{\text{Hist}} \approx \lambda_{2\text{xCO}_2}$ and ECS $\approx -\Delta F_{2\text{xCO}_2}/\lambda_{\text{Hist}}$ (e.g., Otto et al. 2013). However, the past decade of research has shown that assuming constant λ produces ECS estimates from the historical record that are biased low (Marvel et al. 2016; Armour 2017; Proistosescu and Huybers 2017; Andrews et al. 2018, 2022). We now appreciate the importance of pattern effects, i.e., the dependence of radiative feedbacks on the spatial pattern of temperature change (e.g., Armour et al. 2013; Andrews et al. 2015; Gregory and Andrews 2016; Zhou et al. 2016; Stevens et al. 2016; Proistosescu and Huybers 2017; Ceppi and Gregory 2017, 2019; Andrews and Webb 2018; Dong et al. 2019, 2020, 2021; Rugenstein et al. 2016, 2023; Williams et al. 2023; Günther et al. 2024; Mackie et al. 2025; Kawaguchi and Ceppi 2025; Fredericks et al. 2026; Tam et al. 2026; Proistosescu et al. 2026).

In brief, pattern effects arise because identical amounts of surface warming/cooling in different regions have different impacts on clouds and the global energy budget. Warming in convective regions warms the free troposphere, which increases reflective low-cloud cover in remote regions, producing negative (i.e., more-stabilizing) feedbacks (Ceppi and Gregory 2017; Andrews and Webb 2018; Dong et al. 2019; Fueglistaler 2019). On the other hand, warming in subsidence regions weakens local temperature inversions and reduces low-cloud cover (Klein and Hartmann 1993; Wood and Bretherton 2006), producing positive (i.e., less-stabilizing) feedbacks. Compared to the Tropics, temperature changes at higher latitudes tend to produce less-negative feedbacks due to cloud, lapse-rate, and ice-albedo feedbacks (Kang and Xie 2014; Ceppi and Gregory 2019; Cooper et al. 2024, 2026).

Historical warming patterns and feedbacks differ from the expected long-term response to CO_2 due to differences between the fast and slow responses to CO_2 forcing, the distinct responses to various historical forcings, and natural variability (e.g., Senior and Mitchell 2000; Shindell 2014; Gregory and Andrews 2016; Marvel et al. 2016; Armour et al. 2016; Proistosescu and Huybers 2017; Armour 2017; Persad and Caldeira 2018; Paynter et al. 2018; Dong et al. 2019; Gregory et al. 2020; Rugenstein et al. 2020; Andrews et al. 2022; Günther et al. 2022; Huusko et al. 2022; Salvi et al. 2022, 2023; Hwang et al. 2024). The warming pattern over c. 1980–2014 has been particularly surprising compared to expectations from CO_2 forcing (Wills et al. 2022; Watanabe et al. 2024): the tropical Pacific warmed in the west and cooled over much of the east (Fig. 1) (Fueglistaler and Silvers 2021), and Antarctic sea ice expanded over the Southern Ocean while SST cooled, although the SST cooling has uncertain magnitude (Cooper et al. 2025). The projected long-term response to CO_2 forcing is opposite to the 1980–2014 pattern (and also differs from the 1901–2022 patterns in Fig. 1): coupled atmosphere–ocean general circulation models (AOGCMs) show amplified long-term warming in the eastern Pacific and Southern Ocean (Andrews et al. 2015; Dong et al. 2020). If the warming pattern eventually resembles model projections under sustained CO_2 forcing, feedbacks are expected to become less negative, leading to higher ECS estimates compared to those that implicitly assume a constant warming pattern (Dong et al. 2021; Armour et al. 2024).

To account for pattern effects in ECS estimates from historical evidence, we must estimate the difference in feedbacks between the period providing evidence and the equilibrium response to 2xCO_2 (Armour 2017; Andrews et al. 2018):

$$\Delta\lambda = \lambda_{2\text{xCO}_2} - \lambda_{\text{Hist}}. \tag{3}$$

Because this $\Delta\lambda$ arises due to differences in the historical versus 2xCO_2 pattern of temperature change, it is often called the historical pattern effect.

Historical $\Delta\lambda$ is typically estimated by comparing the λ_{Hist} from atmospheric general circulation models (AGCMs) using prescribed observational SST/SIC versus $\lambda_{2\text{xCO}_2}$ in corresponding coupled models, which is approximated using simulations of *abrupt-4xCO2* (Andrews et al. 2018, 2022). Combining Eq. (3) with Eq. (2), ECS from historical evidence becomes:

$$\text{ECS} = \frac{-\Delta F_{2\text{xCO}_2}}{\lambda_{\text{Hist}} + \Delta\lambda}. \tag{4}$$

Eq. (4) is now standard for historical constraints on ECS (Sherwood et al. 2020; Forster et al. 2021), and the same logic applies to ECS estimates from paleoclimates (Cooper et al. 2024, 2026; Dvorak et al. 2025).

Previous studies found that accounting for pattern effects makes the historical record a weak constraint on the upper bound of ECS because $\Delta\lambda$ appears to be large and positive (Andrews et al. 2018, 2022), i.e., $\lambda_{2\text{xCO}_2}$ is less stabilizing (with less-negative feedbacks) than λ_{Hist}. Based primarily on results spanning 1871–2010 from Andrews et al. (2018), recent community assessments reported a central estimate of $\Delta\lambda \approx 0.5\ \text{W}\,\text{m}^{-2}\,\text{K}^{-1}$ (Sherwood et al. 2020; Forster et al. 2021). They inflated the uncertainty ($\pm 0.5\ \text{W}\,\text{m}^{-2}\,\text{K}^{-1}$ at 90% confidence) because the additional spread in $\Delta\lambda$ from SST/SIC uncertainty had not yet been quantified. Andrews et al. (2022) analyzed additional simulations from the Coupled Model Intercomparison Project Phase 6 (CMIP6, Eyring et al. 2016) and Cloud Feedback Model Intercomparison Project Phase 3 (CFMIP3, Webb et al. 2017) and found a mean $\Delta\lambda = 0.70\ \text{W}\,\text{m}^{-2}\,\text{K}^{-1}$ using the SST/SIC boundary condition for the Atmospheric Model Intercomparison Project (PCMDI-AMIP-1-1-9, commonly called "AMIP"; Hurrell et al. 2008) in 14 AGCMs. By substituting the SSTs from HadISST1 (Rayner et al. 2003) in 9 of the AGCMs, they found a mean $\Delta\lambda = 0.48\ \text{W}\,\text{m}^{-2}\,\text{K}^{-1}$. These values are based on 1871–2010, although some simulations were extended to 2014. Note that AMIP and HadISST1 have very similar SSTs until 1981 and similar sea ice by design, so they do not fully capture the structural uncertainty in SST/SIC trends.

Since the studies of Sherwood et al. (2020) and Andrews et al. (2022), there are two key developments that impact our understanding of historical constraints on ECS. The first is the realization that uncertainty in historical SST/SIC patterns is a formidable obstacle when quantifying the historical pattern effect, not only in the distant past but even over the satellite era. The second development is that several key climate features have evolved over the past decade. Importantly, the warming pattern has evolved, which could modify the magnitude of $\Delta\lambda$ compared to previous estimates (which were based on simulations ending between 2010 and 2014). Moreover, global temperature has increased more rapidly over the past decade, coinciding with increases in Earth's energy imbalance, and estimates of historical radiative forcing have been revised. These developments, which we review below, motivate revisiting the historical pattern effect and ECS.

Although uncertainty in SST datasets has been a topic of study for decades (e.g., Deser et al. 2010; Hurrell and Trenberth 1999), only recently has a growing concern emerged that SST/SIC uncertainty could impact λ_{Hist}. Some recent studies report that the historical pattern effect could be negligible, implying lower ECS, and that the large pattern effect (especially from the AMIP dataset) is due to problems with the historical SST/SIC patterns (Lewis and Mauritsen 2021; Modak and Mauritsen 2023). SST uncertainties across datasets are substantial in regions that impact key mechanisms for pattern effects, e.g., the tropical Pacific (Fueglistaler and Silvers 2021) and Southern Ocean (Cooper et al. 2025). These uncertainties affect not only the quantification of $\Delta\lambda$ over the full historical record but also our understanding of decadal variations in feedbacks, even through the satellite era (Menemenlis et al. 2025; Cooper et al. 2025; Fan et al. 2025).

Figure 1 illustrates the disparity between SST patterns in different reconstructions. We show six datasets, which are described in Section 2: the new ensemble reanalysis of Cooper et al. (2025), which we refer to here as "C25"; AMIP (PCMDI-AMIP-1.1.9, Hurrell et al. 2008); NOAA ERSST (version 5, Huang et al. 2017); HadISST1 (Rayner et al. 2003); HadISST2.4 (Titchner and Rayner 2014); and a recently infilled product called DCENT-I (Chan et al. 2026).

The AMIP dataset has been the centerpiece for quantifying λ_{Hist} and $\Delta\lambda$ through CMIP6/CFMIP3 (Webb et al. 2017; Andrews et al. 2018, 2022) and is on track to play the same role in CMIP7/CFMIP4 simulations (Dunne et al. 2025; Ceppi et al. 2026). Lewis and Mauritsen (2021) criticize AMIP's merging of two datasets in 1981, which could be responsible for AMIP's strongly negative λ_{Hist} and possibly too-large pattern effect. Fueglistaler and Silvers (2021) attribute AMIP's large pattern effect to its especially strong strengthening in the tropical SST contrast between the warmest convective regions and the cooler subsiding regions over 1980–2014; other SST datasets show a weaker trend. In a single AGCM (MPI-ESM1.2-LR), Modak and Mauritsen (2023) tested an ensemble of opportunity (seven SST datasets) and found that AMIP produces the largest $\Delta\lambda$ of 0.5 W m^{-2} K^{-1}, whereas the Vaccaro et al. (2021) dataset produced $\Delta\lambda \approx 0$. This wide range of 0.0–0.5 W m^{-2} K^{-1} does not even consider uncertainty in SIC. Clearly, the contribution of SST/SIC to uncertainty in historical feedbacks needs to be systematically quantified and propagated through to historical ECS constraints.

To address this need, Cooper et al. (2025)—hereafter C25—use coupled data assimilation to reconstruct SST, SIC, T, and sea level pressure (SLP) over 1850–2023. C25's 1600-member ensemble of monthly gridded SST/SIC is simultaneously constrained by coupled dynamics and in situ observations of SST, marine SLP, land T, and satellite observations of SIC. The ensemble is designed to span the plausible range of historical SST/SIC patterns and is described further in Section 2. In this study, we primarily use C25's ensemble to quantify historical feedbacks.

New questions have emerged with recent changes in the SST pattern (cf. trends over 2001–2022 with 1980–2014 in Fig. 1). The northeastern Pacific has switched from cooling to warming, as have portions of the Southern Ocean. Antarctic SIC has decreased rapidly since 2014, in contrast to its steady increase over 1980–2014 (Roach and Polvani 2026). Meanwhile, the North Atlantic has switched from widespread warming to a tripole pattern of high-latitude cooling, midlatitude warming, and subtropical cooling. From the net effect of these recent changes, which apparently reduce the differences between the historical SST pattern and model projections of *abrupt-4xCO$_2$*, we might expect λ_{Hist} to be less negative and the historical pattern effect to be smaller compared to previous estimates (Andrews et al. 2022; Van Loon et al. 2026).

Furthermore, the global-warming rate, Earth's energy imbalance, and radiative forcing all appear to have increased over the past 10–20 years. Trends in global-mean T have become stronger since 2014 (Foster and Rahmstorf 2026; Richardson 2022), with record warmth in 2023–2024 augmented by El Niño (Raghuraman et al. 2024b; Blanchard-Wrigglesworth et al. 2025; Tsuchida et al. 2026). Earth's energy imbalance (ΔN) has increased by 0.45 W m^{-2} dec^{-1} over 2001–2024 (Loeb et al. 2018, 2024; Raghuraman et al. 2021; Olonscheck and Rugenstein 2024; Hodnebrog et al. 2024; Allan and Merchant 2025; Mauritsen et al. 2025; Stevens et al. 2026), implying increased planetary heat uptake. Radiative forcing has increased since 2014 from ongoing greenhouse-gas emissions and reductions in the negative forcing from anthropogenic aerosols (Forster et al. 2025; Van Loon et al. 2025; Kramer et al. 2021). Importantly, estimates of aerosol forcing (1850–present) have also been revised since Bellouin et al. (2020), which was used in the ECS assessment of

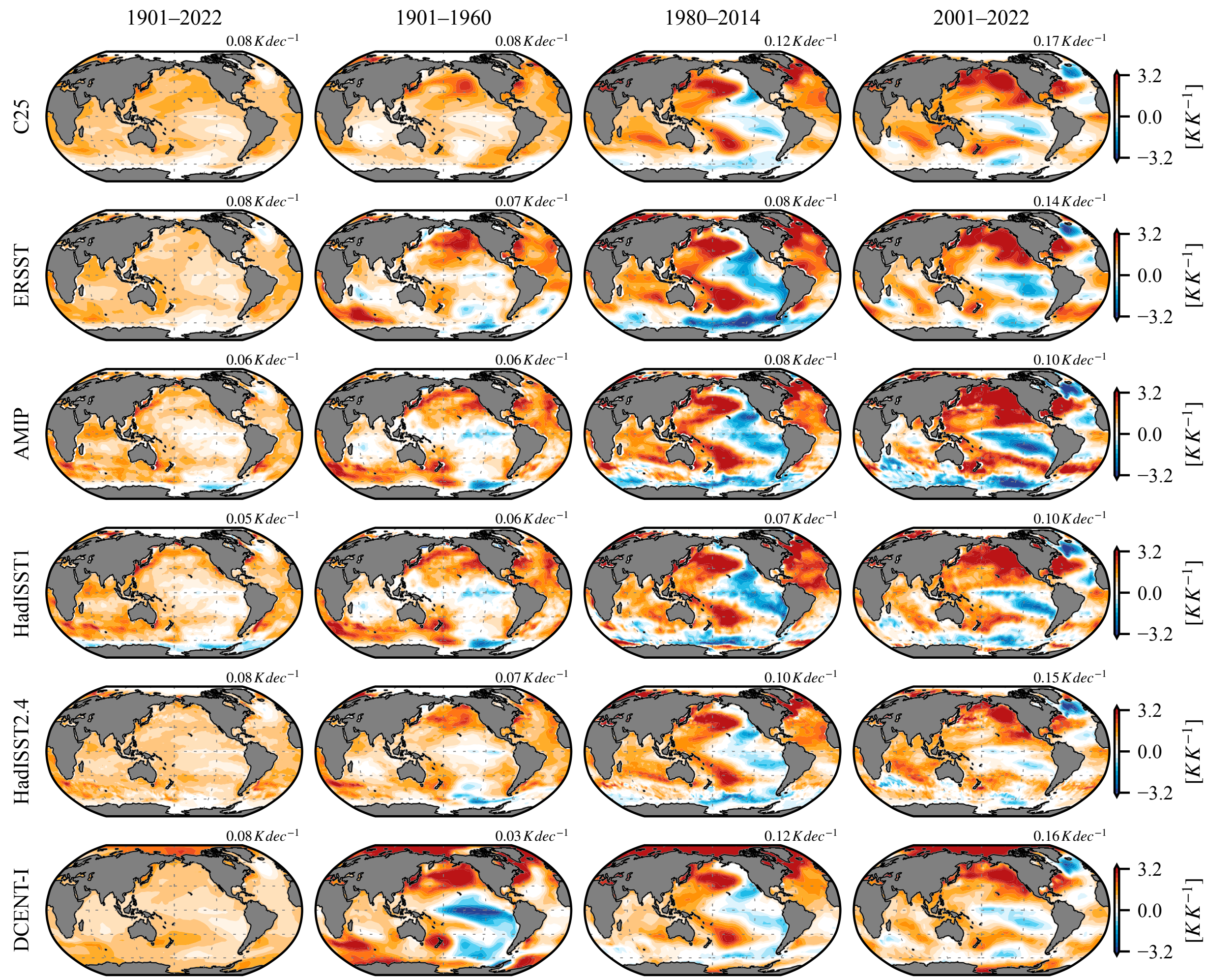

FIG. 1. **Trends in sea-surface temperature (SST) from various datasets.** First column shows long-term trends (1901–2022), and columns 2–4 show trends over selected periods that are relevant to changes in radiative feedbacks. Top row shows the ensemble mean of 14 members used in this study from C25 (Cooper et al. 2025). Other rows show ERSSTv5 (Huang et al. 2017), PCMDI-AMIP-1.1.9 (AMIP, Hurrell et al. 2008), HadISST1 (Rayner et al. 2003), HadISST2.4 (Titchner and Rayner 2014), and DCENT-I (Chan et al. 2026). Note that HadISST2.4 trends end in 2021, and DCENT-I differs over polar regions because it transitions to air temperature where sea ice is assumed to be present. Local SST trends in each panel are divided by corresponding trends in global-mean SST (shown in upper right).

Sherwood et al. (2020): uncertainty remains large, but recent assessments no longer support ΔF from aerosol-cloud interactions more negative than $-2\ \mathrm{W\,m^{-2}}$ (Forster et al. 2021, 2025; Park et al. 2025; Zelinka et al. 2026; Roi-Cohen et al. 2026; Yuan et al. 2026).

In summary, research over the past decade has largely explained why feedbacks depend on the pattern of temperature change. However, we do not yet have a conclusive explanation for what caused the peculiar pattern of SST trends over 1980–2014 and whether its strongly negative feedback is unique compared to past variations in λ, especially considering the uncertainty in historical SST/SIC patterns. Changes over the past 10 years suggest that feedbacks may be evolving, and ECS constraints from the historical energy budget ought to be revisited.

The primary aims of this paper are quantifying time-varying feedbacks and the historical pattern effect over 1850–2023 and producing a novel quantification of the spread in $\Delta\lambda$ from SST/SIC uncertainty. We prescribe SST/SIC ensemble members from C25 in six AGCMs to assess the relative contributions to uncertainty in $\Delta\lambda$ from SST/SIC versus atmospheric model physics, and we compare our results with previous $\Delta\lambda$ estimates using existing SST/SIC datasets (Andrews et al. 2022; Modak and Mauritsen 2023). Finally, we revise Sherwood et al. (2020)'s ECS constraints from the historical record with data through 2023 and our revised $\Delta\lambda$. Section 2 describes the SST/SIC datasets, AGCM simulations, and observational data. Section 3 shows time series of historical temperature, sea ice, net radiation, and forcing, while Section 4 shows how feedbacks vary over 1850–2023. Section 5 evaluates the historical pattern effect over the full historical record, and Section 6 revises ECS constraints. Section 7 reviews the conclusions.

2. Methods and data

To quantify feedbacks over the historical record, we perform simulations with a multi-model ensemble of AGCMs using prescribed time-varying SST/SIC over 1850–2023 and constant preindustrial forcings. This AGCM setup is called *"piForcing"* (Gregory and Andrews 2016; Webb et al. 2017; Ceppi et al. 2026), or specifically *"AMIP-piForcing"* when using the AMIP SST/SIC boundary conditions, and is an accurate way to diagnose the TOA response to changes in surface temperature (Andrews et al. 2015; He and Soden 2016; Haugstad et al. 2017). By design, *piForcing* simulations maintain $\Delta F = 0$ in Eq. (1), hence $\lambda = \mathrm{d}N/\mathrm{d}T$ in differential form or $\lambda = \Delta N/\Delta T$ using finite differences in the means between two periods (Gregory et al. 2002, 2004); these two methods of estimating λ are known as "differential" and "effective" λ, respectively (Rugenstein and Armour 2021). In reality, ΔF is non-zero and time-varying in Eq. (1), in which case $\lambda = \mathrm{d}(N - F)/\mathrm{d}T$ or $\lambda = (\Delta N - \Delta F)/\Delta T$. We use the differential form to estimate λ from satellite-era observations (following Gregory et al. 2020; Andrews et al. 2022). We describe the SST/SIC boundary conditions and AGCM simulations in the following sub-sections, as well as estimates of N, T, and F.

a. SST and SIC boundary conditions

For our main AGCM simulations, we use Cooper et al. (2025)'s reanalysis (C25) of monthly gridded (1.9° lat. × 2.5° lon.) SST and SIC. C25 differs from the SST/SIC datasets used in previous studies because it is produced using coupled data assimilation, which gives C25 four key advantages:

1. For observational constraints, C25 includes land T from CRUTEM5 (Osborn et al. 2021), marine SLP from ICOADS (Freeman et al. 2017), and satellite-era SIC from NOAA/NSIDC CDR (Meier et al. 2021), in addition to the in situ SST data from HadSST4 (Kennedy et al. 2019); all observations inform both SST and SIC.

2. For physical constraints, C25 uses the dynamics of coupled models in its monthly forecasts and in using a Kalman filter to simultaneously assimilate observations across the coupled state; the forecasts are produced by computationally efficient linear inverse models (e.g., Penland and Sardeshmukh 1995) trained on eight CMIP6 AOGCMs, known as model priors.

3. For uncertainty quantification, C25 produces a wide range of SST/SIC boundary conditions (1600 ensemble members) that sample error in the observations (including bias-correction uncertainty from HadSST4), intermodel spread in the dynamics that informs unobserved regions, and intramodel spread from forecast uncertainty given the initial conditions.

4. For validation, C25 shows that the method works by reconstructing an out-of-sample model's historical simulation; existing infilled SST/SIC datasets have not, to our knowledge, performed this validation test.

From C25's 1600 members, we select 14 members to use for our AGCM boundary conditions. In choosing the 14 members, we aim to capture the spread in $\Delta\lambda$ across the full 1600 member ensemble. We use Green's functions from CAM4 (Dong et al. 2019), CAM5 (Zhou et al. 2017), and GFDL-AM4 (Zhang et al. 2023) to rank ensemble members by estimates of their $\Delta\lambda$. As expected, most of C25's spread is from different model priors, so we select the median and one additional member from each model prior. This choice leads to endmembers of the 14-member ensemble that approximate the 5$^{\text{th}}$ and 95$^{\text{th}}$ percentiles of the full 1600-member ensemble, and the remaining members are distributed approximately uniformly across the 90% range. The ranking is consistent across all three Green's functions. Finally, we inspect the ensemble to ensure that the spread in modes of climate variability and sea ice is well sampled (see Fig. 5 of Cooper et al. 2025). This inspection led to excluding the EC-Earth3 prior due to its inability to reconstruct the full decline of Arctic sea ice in recent decades, hence the 14 members are from 7 priors × 2 members per prior.

C25 reconstructs anomalies relative to 1961–1990 rather than the actual SST/SIC values that we need for boundary conditions. To generate actuals, we add C25's anomalies to the 1961–1990 climatology of actual SST from HadISST2.3's ensemble mean (Titchner and Rayner 2014) and to a climatology of actual SIC developed by C25; HadISST2's SIC climatology over 1961–1990 (only available for version 2.1) appears unusable due to issues during its transition to satellite data (discussed in C25). From the monthly means, we generate mid-month values that are prescribed in AGCMs.

We compare with existing SST/SIC datasets listed below that have been used to estimate time-varying λ and $\Delta\lambda$. The distinctions between datasets have been described by Lewis and Mauritsen (2021) and Modak and Mauritsen (2023), and we refer readers to those papers for details. Here, we summarize what is most relevant to feedback uncertainty and current usage.

- AMIP (PCMDI-AMIP-1-1-9, Hurrell et al. 2008) is the standard SST/SIC dataset used in *AMIP-piForcing* simulations, which typically start in 1870 (Webb et al.

2017), and is the dataset most commonly used to quantify $\Delta\lambda$ (e.g., Gregory and Andrews 2016; Andrews et al. 2018, 2022). Note that version 1-1-10 is the main SST/SIC for CMIP7/CFMIP4 (Durack et al. 2025a; Dunne et al. 2025; Ceppi et al. 2026).

- HadISST1 (Rayner et al. 2003) has been used for alternative estimates of $\Delta\lambda$ (Andrews et al. 2022; Lewis and Mauritsen 2021), but AMIP and HadISST1 are tightly related; AMIP uses SST from HadISST1 before November 1981, and their SIC is nearly identical over most of the record (Cooper et al. 2025). HadISST1 is the alternative SST/SIC selected for CFMIP4 (Ceppi et al. 2026).

- NOAA ERSSTv5 (Huang et al. 2017), hereafter ERSST, only has $\Delta\lambda$ published from a single AGCM (MPI-ESM1.2-LR, Modak and Mauritsen 2023), but it appears frequently in studies of SST patterns and analyses of post-1980 SST trends, especially over the Southern Ocean (e.g., Watanabe et al. 2024; Kang et al. 2023; Hartmann 2022). ERSST does not include its own SIC, but its SST is informed by the SIC in HadISST2 (Titchner and Rayner 2014), which appears to be an outlier (Cooper et al. 2025). When prescribing SST boundary conditions from ERSST, we use AMIP's SIC for consistency with previous simulations (Modak and Mauritsen 2023; Philips and Simpson 2026). ERSSTv5 is an additional dataset available for CMIP7 (Durack et al. 2025b).

We focus on the C25 ensemble, AMIP, ERSST, and HadISST1, but we include results from the additional SST datasets used in MPI-ESM1.2-LR by Modak and Mauritsen (2023). These SST datasets, labeled as "Other" in our figures, are COBE-SST2 (Hirahara et al. 2014), had4-krig-v2-0-0 and had4sst4-krig-v2-0-0 (Cowtan and Way 2014), and Vaccaro et al. (2021). All "Other" SST simulations use AMIP's SIC.

Although we do not yet have any feedback estimates from HadISST2.4 (Titchner and Rayner 2014) or DCENT-I (Chan et al. 2026), we include them in Fig. 1 for comparison. HadISST2.4 is included because it uses improved in situ SST data (Kennedy et al. 2019) compared to HadISST1 and is planned for use in CERESMIP, a recent modeling protocol that aims to investigate the CERES satellite record with AGCMs (Schmidt et al. 2023). DCENT-I is a blended surface-temperature dataset with improved bias corrections on the non-infilled data (Chan and Huybers 2019, 2021; Chan et al. 2025). For infilling, Chan et al. (2026) use post-1980 SST patterns from Embury et al. (2024) to estimate a covariance and then apply it over 1850–2024 using anisotropic kriging.

Figure 1 shows SST trends from C25 (ensemble mean of the 14-member subset in this study), AMIP, ERSST, HadISST1, HadISST2.4, and DCENT-I for multiple historical periods.

b. AGCM simulations

We quantify feedbacks using *piForcing* simulations in AGCMs (summarized in Table 1), i.e., we prescribe constant radiative forcings at preindustrial levels with time-varying historical SST/SIC (Andrews 2014; Gregory and Andrews 2016).

Using the C25 ensemble, we run 14 SST/SIC boundary conditions spanning 1850–2023 in four AGCMs: CAM4 (Neale et al. 2013), CAM5 (Neale et al. 2012), CAM6 (Danabasoglu et al. 2020), and HadAM3 (Pope et al. 2000). In two AGCMs, MPI-ESM1.2-LR (Mauritsen et al. 2019) and GFDL-AM4 (Held et al. 2019), we run a subset of 3 boundary conditions from C25, which approximates the median and 66% likely range for λ_{Hist} based on estimates from Green's functions. We refer to the C25 simulations as *C25-piForcing*. In HadAM3, we run an initial-condition (IC) ensemble with 15 members, which uses a single SST/SIC boundary condition from C25 with atmospheric micro-perturbations.

For comparison, we also run *piForcing* IC ensembles (5 members) with the AMIP and ERSST boundary conditions through 2021 in CAM4 and CAM5. Our *AMIP-piForcing* runs span 1870–2021, which is an extension compared to the 1870–2010 and 1870–2014 simulations in Andrews et al. (2022). Our *ERSST-piForcing* runs span 1858–2021.

We leverage previously published *piForcing* simulations from Andrews et al. (2022) and Modak and Mauritsen (2023). Andrews et al. (2022) provide *piForcing* results from 14 AGCMs using AMIP and 9 AGCMs using HadISST1; 6 of 14 simulations using AMIP are averages over IC ensembles with 3-5 members, as are 4 of 9 simulations using HadISST1. Modak and Mauritsen (2023) provide 5-member IC ensembles for their seven boundary conditions, all using MPI-ESM1.2-LR.

Finally, we include results from a 10-member IC ensemble in CAM6 using ERSST (Philips and Simpson 2026). CAM6's ERSST ensemble is not a *piForcing* simulation but rather includes both time-varying SST/SIC and forcings, so we estimate its feedback (and its *piForcing* equivalent) by subtracting CAM6's estimate of the forcing. This approach to estimating feedbacks, e.g., $\lambda = (\Delta N - \Delta F)/\Delta T$, is analogous to observational estimates and has been validated with *amip-piForcing* and *piClim-histall* simulations (Dong et al. 2021; Salvi et al. 2023). We subtract the ensemble-mean ΔF from CAM6's 3-member IC ensemble with time-varying forcings and constant preindustrial SST/SIC (*piClim-histall* in CMIP language, Pincus et al. 2016).

TABLE 1. Summary of AGCM simulations using SST/SIC boundary conditions (BCs) from C25 (Cooper et al. 2025) and other reconstructions, some of which have initial-condition (IC) ensembles (n represents the number of ensemble members). The aggregated bottom section includes simulations from Andrews et al. (2022) and Modak and Mauritsen (2023).

SST	SIC	n BC	n IC	Start	End	n AGCM	AGCMs
New *piForcing* simulations in this study							
C25	C25	3–14	1	1850	2023	6	GFDL-AM4 (n BC = 3), MPI-ESM1.2-LR (3), HadAM3 (14), CAM4 (14), CAM5 (14), CAM6 (14)
C25	C25	1	15	1850	2023	1	HadAM3
AMIP	AMIP	1	5	1871	2021	2	CAM4, CAM5
ERSST	AMIP	1	5	1858	2021	2	CAM4, CAM5
Aggregated with previous studies							
AMIP	AMIP	1	1–5	1871	2010–2021	15	6 in C25 plus CNRM-CM6-1, CanESM5, ECHAM6.3, GFDL-AM3, HadGEM2, HadGEM3-GC31-LL, IPSL-CM6A-LR, MIROC6, MRI-ESM2-0
HadISST1	AMIP	1	1–5	1871	2010-2016	9	5 in C25 (excludes CAM5) plus ECHAM6.3, GFDL-AM3, HadGEM2, HadGEM3-GC31-LL
ERSST	AMIP	1	5-10	1858–1880	2010–2021	4	MPI-ESM1.2-LR, CAM4, CAM5, CAM6
Other	AMIP	4	5	1858–1880	2010–2017	1	MPI-ESM1.2-LR; See text for list of Other SST BCs

c. 2xCO$_2$ feedbacks from coupled models

To estimate $\Delta\lambda$ (Eq. 3), we compare λ_{Hist} from *piForcing* simulations in AGCMs with feedbacks from coupled simulations of *abrupt-4xCO$_2$* in the parent AOGCMs corresponding to each AGCM. In doing so, we assume $\lambda_{2\mathrm{xCO}_2} \approx \lambda_{4\mathrm{xCO}_2}$, which is practical because many more models provide *abrupt-4xCO$_2$* than *abrupt-2xCO$_2$*. The assumption appears accurate for many but not all models: $\lambda_{4\mathrm{xCO}_2}$ tends to be less negative than $\lambda_{2\mathrm{xCO}_2}$, but statistical significance of the difference is marginal (Poletti et al. 2024; Mitevski et al. 2023; Bloch-Johnson et al. 2021; Good et al. 2016).

We estimate $\lambda_{4\mathrm{xCO}_2}$ with ordinary least squares (OLS) regression over years 1–150 following abrupt quadrupling (Gregory method; Gregory et al. 2004; Zehrung et al. 2025). He et al. (2025) find that applying the Gregory method to years 1–150 accurately estimates the λ relevant to ECS, i.e., effective and differential λ are approximately equal under *abrupt-4xCO$_2$*, which supports our use of differential λ; however, they note the Gregory method underestimates the forcing, which does not affect our analysis. To be consistent with our regression method for λ_{Hist}, we regress 5-year block means of N and T, so each data point in the regression represents a 5-year mean (instead of the commonly used 12-month mean). Block averaging reduces bias in the regression from interannual variability (e.g., Lewis and Mauritsen 2021; Dunne et al. 2020), which can have a substantial impact on λ_{Hist} but typically has a small impact on $\lambda_{4\mathrm{xCO}_2}$ over years 1–150. We discuss block averaging in Section 4a and illustrate its impact in Fig. A1.

AOGCM results for GFDL-AM4, CAM4, CAM6, and MPI-ESM1.2-LR are from Andrews et al. (2022) while CESM1-CAM5 (2° resolution) is from Bacmeister et al. (2020). For CESM2.1-CAM6, we use *abrupt-2xCO$_2$* because of a well-documented nonlinearity in λ, which is caused by an inappropriate limiter in the ice-number microphysics scheme and is responsible for the high ECS in its *abrupt-4xCO$_2$* simulation (Zhu et al. 2022, 2024; Duffy et al. 2026). The *abrupt-2xCO$_2$* simulation uses 1° CAM6 resolution (Dvorak et al. 2025) while our *C25-piForcing* ensemble uses 2° CAM6, but Duffy et al. (2026) find that CESM2's ECS is consistent across resolutions. For simplicity we use *abrupt-4xCO$_2$* when referring to all coupled models, even though CESM2-CAM6's feedback comes from *abrupt-2xCO$_2$*. Note that HadAM3's parent AOGCM, HadCM3, uses a 100-year simulation of *abrupt-4xCO$_2$* instead of 150 years.

d. Observational estimates of N, F, and T

We use observational estimates of N, F, and T primarily for two purposes. First, we compare observational λ with results from *piForcing* simulations (in Section 4). Second, we revise ECS constraints with observational data through 2023 (Section 6).

For the feedback comparison with observational estimates over 1985–2023, we use ΔN from DEEP-C version 5.1 (Allan et al. 2014; Yang et al. 2025). ΔF is from the Indicators of Global Climate Change (Forster et al. 2025), which extends the methods of IPCC AR6 (Forster et al. 2021) through 2024. ΔT is from C25's reanalysis (see explanation below). We also show λ over 2001–2023 using ΔN observations from CERES EBAF Ed4.2.1 (Loeb et al. 2018). Note that DEEP-C and CERES share data sources and are intentionally aligned during their overlap period. To estimate λ from observations (Fig. 3b–c), we regress 5-year smoothed $(N - F)$ against T. CERES and DEEP-C do not include errors for ΔN, so we use the central estimates for ΔF and ΔT, and our error estimates for λ represent statistical errors in the regression. The regression error accounts for serial correlation by using the effective number of degrees of freedom from lag-1 autocorrelation of residuals (e.g., Wilks 2019; Santer et al. 2000).

To revise ECS estimates from the historical energy budget over 1850–2023 (following Sherwood et al. 2020), we need observational estimates through 2023 for ΔN, ΔF, and ΔT, and revised $\Delta\lambda$ from our *C25-piForcing* simulations. We discuss each component in detail in Section 6a, including central estimates and uncertainties. Briefly, Forster et al. (2025) extend IPCC AR6's methods to provide ΔF and ΔN, which is estimated by scaling the changes in ocean heat content (OHC) that comprise 91% of the total energy change. For ΔT, we use C25's reanalysis because it directly represents the desired metric (near-surface air temperature, T) rather than blended surface temperatures, i.e., merged SST over open ocean, T over land, and T over the time-varying regions where sea ice is expected (Cowtan et al. 2015; Richardson et al. 2016) and has improved methods for infilling unobserved regions. Sherwood et al. (2020) explain the preference for ΔT over blended surface temperature. Note that ΔT from the DCENT-I dataset is closer to C25 than Forster et al. (2025); see Section 6a for further details.

3. Surface temperature, sea ice area, and TOA radiation in AGCM simulations

a. Surface temperature

In Fig. 2a–b, we show historical time series of global ΔT and ΔN from CAM4 and CAM5 (the mean and full range of 28 ensemble members; 14 in each AGCM). We show only CAM4 and CAM5 to support comparison between *C25-piForcing* and *AMIP/ERSST-piForcing*; we only ran *AMIP/ERSST-piForcing* simulations through 2021 in those two AGCMs. *AMIP/ERSST-piForcing* each represent a mean of 10 members (5 from CAM4 and CAM5). The time series are similar in the other AGCMs where available.

Increases in ΔT over 1850–2023 in the *C25-piForcing* simulations are slightly smaller than in the corresponding 14 members from the C25 reconstruction because *piForcing* simulations do not include the warming that results directly from historical forcing (as discussed in Andrews et al. 2022). However, the missing warming is smaller than the spread in warming across C25's ensemble members, so the missing warming is not always obvious relative to the spread in Fig. 2a's *C25-piForcing* results. C25's ΔT is similar to Forster et al. (2025) and Chan et al. (2026) over most of the record.

At the end of the record, *AMIP/ERSST-piForcing* have large differences in ΔT relative to IPCC AR6, DCENT-I, and C25, which appears to be due both to missing forcing and the weaker SST warming in those datasets (which is also the case for HadISST1) compared to HadISST2.4,

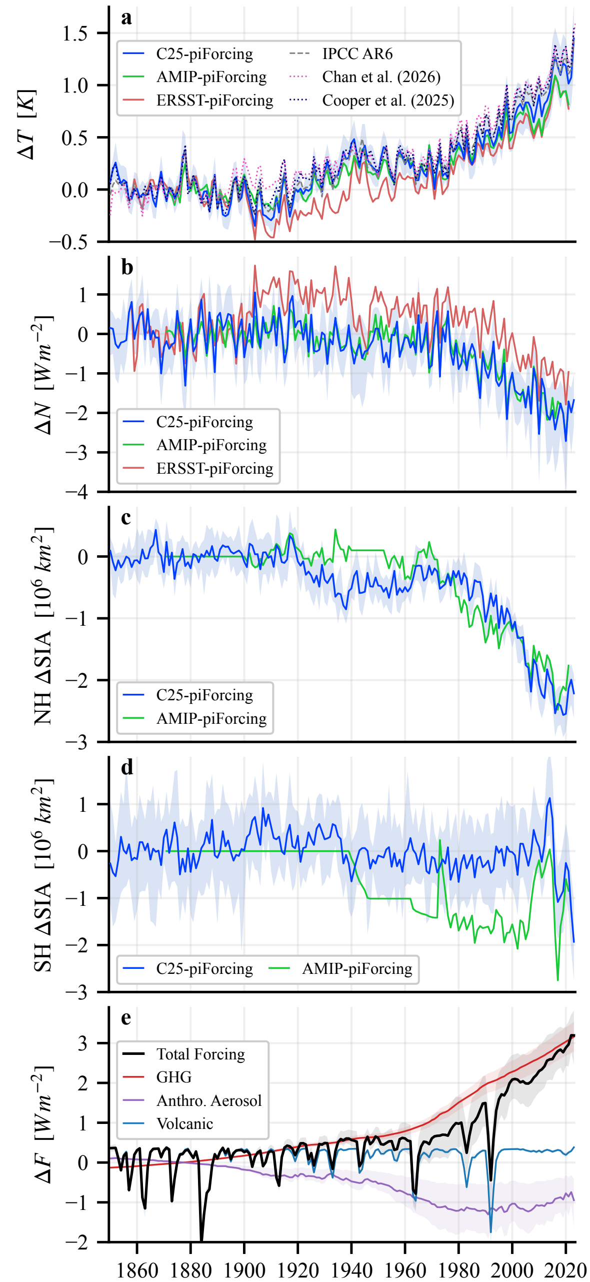

Fig. 2. **Temperature, radiation, and sea ice area (SIA) over 1850–2023.** **(a)** Global near-surface air temperature anomaly (ΔT) from time-varying SST and sea ice in *piForcing* simulations from a subset of AGCMs (mean of CAM4 and CAM5 for ease of comparison between SST/SIC datasets). C25's original reanalysis (Cooper et al. 2025) is shown to compare with *C25-piForcing*; blended T-SST datasets from extended IPCC AR6 (Forster et al. 2025) and Chan et al. (2026) are shown for reference. *C25-piForcing* shading shows range of 28 ensemble members (14 in CAM4 and CAM5). **(b)** Global top-of-atmosphere radiation anomaly (ΔN) from *piForcing*. **(c)** SIA over Northern and **(d)** Southern Hemisphere. **(e)** Global effective radiative forcing (ΔF) and 90% ranges for a subset of forcings from Forster et al. (2025). Anomalies are relative to 1850–1900 means, except *AMIP-piForcing* simulations start in 1871 and *ERSST-piForcing* in 1858.

C25, and DCENT-I (see global-mean trends in Fig. 1). For example, HadISST2.4's global-mean SST trend over 2001–2021 is approximately 50% larger than AMIP's and HadISST1's trends. These trend differences are consistent with known improvements in SST data over the Southern Hemisphere that are included in the non-infilled data from HadSST4, which is used by C25 and HadISST2.4 (Kennedy et al. 2019; Schmidt et al. 2023).

ERSST-piForcing's weaker warming at the end of the record appears largely attributable to its pronounced cooling in the early twentieth century (c. 1900–1910), which creates an offset relative to AR6, DCENT-I, and C25 that persists through the end of the record. A weaker cooling over 1900–1910 appears in *C25-piForcing* and *AMIP-piForcing* (Fig. 2a), and we discuss recent investigations of the early 20th century in Supplemental Text S1.

b. Sea ice area

Total sea ice area (SIA) in the Arctic and Antarctic (Fig. 2c,d) differs substantially between C25 and AMIP, even considering the large spread SIA across the C25 ensemble. We show only the C25 ensemble and AMIP because other *piForcing* simulations use AMIP's SIC. C25 differs from AMIP over the satellite record because C25 assimilates the NOAA/NSIDC CDR data (Meier et al. 2021). AMIP uses HadISST1's SIC before November 1981, with minor adjustments, and then uses NOAA/NCEP OI.v2.0 (Reynolds et al. 2002). OI.v2.0's SIC is intentionally similar to HadISST1's SIC because both rely on the NASA Team passive-microwave dataset (Hurrell et al. 2008; Rayner et al. 2003).

In the Arctic (Fig. 2c), C25 has ice loss during the early twentieth century warming (c. 1920–1940), while SIA is roughly steady in AMIP. The trajectories differ over the satellite era primarily because of differences in the satellite products used.

In the Antarctic (Fig. 2d), there are multiple large differences in SIA. AMIP shows declining SIA over 1980–2000, rather than the increase that has been confirmed in multiple satellite products (e.g., Roach and Polvani 2026). In 2009, AMIP has a large, spurious increase in SIA due to a switch in source data that affects both the SH and NH SIA (Screen 2011), which is not present in C25. This spurious increase could be responsible for AMIP having more SH SIA in 2021 than in any year over 1980–2000, while C25 shows major losses of SIA since 2014 that result in 2021–2023 having less SIA than 1980–2000 (consistent with Roach and Polvani 2026). Furthermore, AMIP shows a large loss of SIA between 1900 and 2000, whereas C25's ensemble mean is approximately flat with large uncertainty and temporal variability. We also note that over 1979–2024, SIC has been declining slightly in the southeastern Pacific sector of the Southern Ocean (Amundsen-Bellingshausen, west of the Drake Passage) and shows little change over 2001–2022 (Roach and Polvani 2026); however, ERSST, AMIP, and HadISST1 all show SST cooling in that region over 2001–2022, unlike C25 and DCENT-I (Fig. 1).

c. TOA radiation

As ΔT increases, ΔN becomes negative (recall that $\Delta N = \lambda \Delta T$ in *piForcing*, with $\lambda < 0$) because Earth exports more energy to space at warmer temperatures (Fig. 2b). C25 and AMIP show approximately similar time-evolution of ΔN compared to ERSST, which follows a distinct trajectory starting c. 1900. We show ΔF from IPCC AR6's extension (Fig. 2e) for comparison. In the following section, we quantify λ from ΔN and ΔT.

4. Time-varying historical feedbacks

a. Time series of the net feedback

Past studies have found large variations in λ over the historical record, but some of these variations could reflect errors in reconstructed SST/SIC rather than real changes in the radiative response to ΔT. We consider two versions of time-varying λ: differential λ, estimated from regression over 30-year windows, and effective λ, estimated from mean anomalies over 18-year rolling windows relative to the preindustrial (pre-1900) mean. The effective λ is most directly relevant to ECS constraints, which is our focus in Section 6. In this section, we focus mainly on the 30-year differential λ because it diagnoses how the relationship between N and T changes as SST/SIC patterns evolve. The differential λ is particularly relevant for investigating whether λ estimated from one historical interval can be extrapolated to represent the response to sustained CO_2 forcing.

Before estimating differential λ over 30-year rolling windows (e.g., Gregory and Andrews 2016), we apply a 5-year running mean to N and T. We then estimate λ as the slope of N against T using OLS regression. Previous studies regressed annual means, but correlated errors in N and T from ENSO and other modes of variability (Yang and Fueglistaler 2026; Miyamoto et al. 2026; Lin et al. 2025; Tsuchida et al. 2023; Ceppi and Fueglistaler 2021; Lutsko 2018) can bias λ toward a value associated with natural variability rather than the desired value associated with forcing. The bias is exaggerated over 30-year windows when forced changes in T are small compared to interannual noise. Lewis and Mauritsen (2021) use 5-year block means of N and T in OLS regression over the full historical record, and Dunne et al. (2020) also use 5-year block means for estimating ECS from *abrupt-4xCO*$_2$ simulations. Our 5-year smoothing similarly reduces biases from natural variability when estimating λ over 30-year windows. We illustrate the impact of 5-year averaging in Fig. A1.

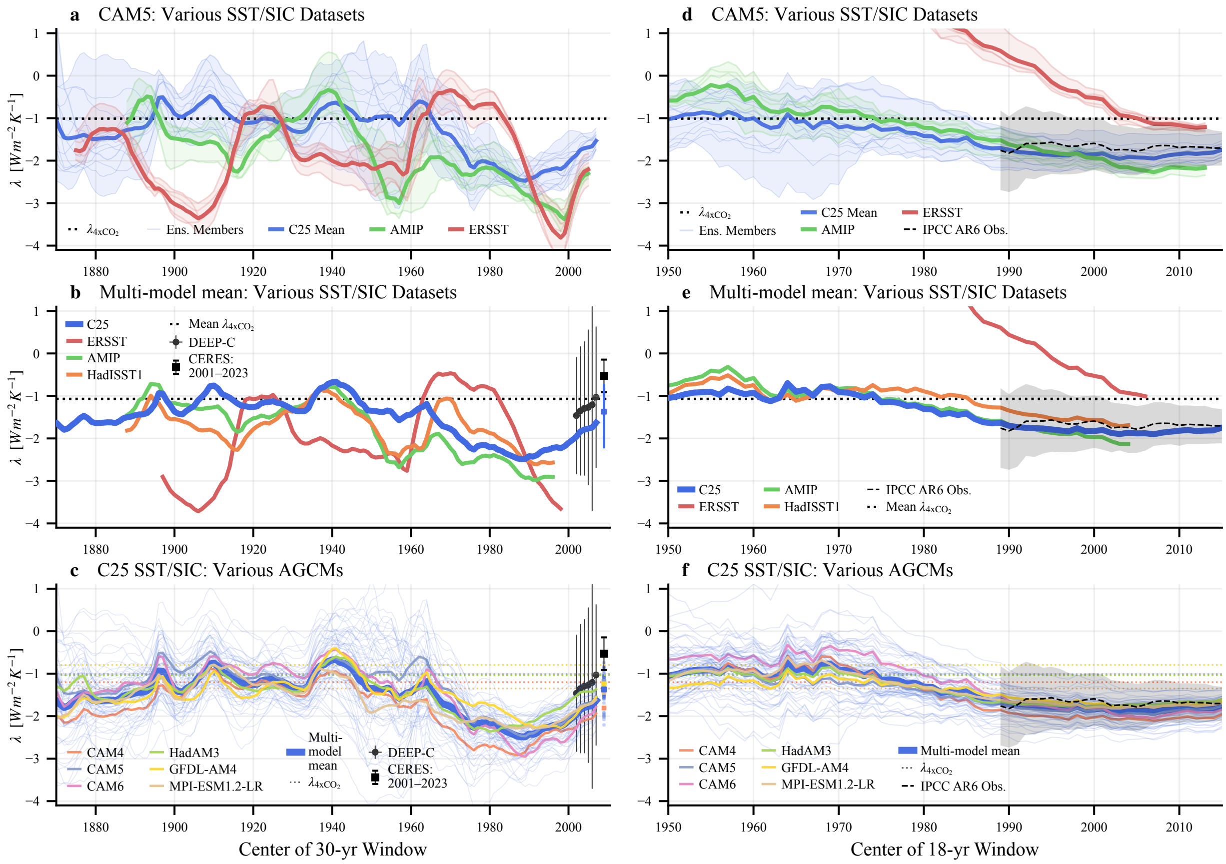

FIG. 3. **Time-varying feedbacks in AGCM *piForcing* simulations: (left column) differential feedbacks ($\lambda = \mathrm{d}N/\mathrm{d}T$) from regression over 30-year windows and (right column) effective feedbacks ($\lambda = \Delta N/\Delta T$) from finite differences over 18-year windows.** Note different horizontal axes in left vs. right columns. **(a)** λ in a single AGCM (CAM5) from various SST/SIC boundary conditions. C25 ensemble members each have distinct SST/SIC, whereas AMIP and ERSST ensembles differ only by initial conditions. CESM1-CAM5's $\lambda_{4\mathrm{xCO_2}}$ is shown for comparison. **(b)** Average λ across six AGCMs in this study and their coupled models' mean $\lambda_{4\mathrm{xCO_2}}$; note ERSST includes only four AGCMs. Observation-based differential λ using DEEP-C is shown for 30-year windows over 1985–2023 and from CERES over 2001–2023; error bars only account for regression errors. C25's λ over 2001–2023 is shown for comparison, and error bars represent the ensemble range. **(c)** C25 ensemble-mean λ for each AGCM, including ensemble members as thin lines and each model's $\lambda_{4\mathrm{xCO_2}}$. **(d–f)** Repeats panels **a–c** using finite differences, where ΔN and ΔT are running-mean anomalies (over 18 years) from the preindustrial mean (1850–1900 for C25, 1871–1900 for AMIP/HadISST1/ERSST; see text for details). Observation-based effective λ is estimated using N and F from extended IPCC AR6 methods (Forster et al. 2025) and T from Cooper et al. (2025), following methods in Sherwood et al. (2020). $\lambda_{4\mathrm{xCO_2}}$ is estimated with 150-year regression of 5-year block means in all panels.

Figure 3a–c shows time-varying net λ over 30-year windows, and each panel highlights different aspects of uncertainty in estimating λ. First, we isolate differences between SST/SIC boundary conditions using CAM5 (Fig. 3a), which includes the *C25-piForcing* ensemble (1850–2023) and 5-member IC ensembles using *AMIP-piForcing* (1871–2021) and *ERSST-piForcing* (1858–2021). The multi-model mean (Fig. 3b) includes six AGCMs for C25 and AMIP, while HadISST1 is missing CAM5 and ERSST is missing HadAM3 and GFDL-AM4. Figure 3c shows all members of the *C25-piForcing* ensemble and illustrates the differences across AGCMs by showing the ensemble mean for each AGCM. We also show observation-based feedbacks from DEEP-C and CERES (Methods). CERES has smaller error despite its shorter window because the autocorrelation of residuals is much weaker after 2000.

We identify four key differences in Fig. 3a–c compared to Andrews et al. (2022)'s AMIP and HadISST1 results:

- First, C25 shows more consistent (i.e., less variable) differential λ over the historical record. C25's ensemble-mean λ does not vary much until after 1960, and the λ variations of individual ensemble members are smaller than variations in AMIP, HadISST1, and especially ERSST.

- Second, C25's ensemble-mean differential λ shows no pattern effect, i.e., $\Delta\lambda \approx 0$, for most of the historical record (Fig. 3c). Only after 1965 does an anomalously stabilizing (negative) λ emerge. The 5-year smoothing of N and T prior to regression tends to make λ less negative, but that change only explains a small part of the difference versus AMIP/HadISST1 in Andrews et al. (2022). SST/SIC explains most of the difference: using C25 reduces the differences between λ and λ_{4xCO_2} over most of the record compared to AMIP, HadISST1, and ERSST (Fig. 3a–b).

- Third, the spread in differential λ due to SST/SIC uncertainty across the C25 ensemble is larger than previously appreciated based on differences between AMIP and HadISST1. This confirms concerns about SST/SIC uncertainty (Lewis and Mauritsen 2021; Fueglistaler and Silvers 2021; Modak and Mauritsen 2023).

- Fourth, by including the most recent decade (2014–2023), we find a particularly noteworthy difference with respect to Andrews et al. (2022) and many other CMIP6-era studies, whose data and simulations ended in 2014. In those studies, the last 30-year window (centered in 2000) showed differential λ at an anomalously negative value (see AMIP, HadISST1, and ERSST in Fig. 3b), but we find that a strong trend toward less-negative feedbacks since 2014 has brought differential λ nearly in line with λ_{4xCO_2}.

In the C25 ensemble, the most-negative differential λ over the entire record occurs for the 30-year window centered around 1988 (multi-AGCM mean of $-2.5\ \mathrm{W\,m^{-2}\,K^{-1}}$ in Fig. 3b–c). Our six AGCMs estimate that, since then, the 30-year λ has become less negative by $0.9\ \mathrm{W\,m^{-2}\,K^{-1}}$, reaching $-1.6\ \mathrm{W\,m^{-2}\,K^{-1}}$ for the 1994–2023 window. A concurrent study by Van Loon et al. (2026) finds a similar trend in the feedback using a convolutional neural network.

Observation-based feedbacks using DEEP-C begin with the 1985–2014 window and show a similar trend toward less-negative λ through 2023, although the central estimate of λ using DEEP-C is less negative than in our six AGCMs. The shorter period (2001–2023) for CERES's λ emphasizes that the post-2000 years produce less-negative λ (Fig. 3b–c).

In Fig. 3d–f, we show the effective λ using finite differences from rolling-mean anomalies over 18-year windows. This method aligns with ECS estimates, for which we use 2006–2023 to quantify changes in the historical energy budget relative to 1850–1900 (Section 6). We include the observational λ using ΔN and ΔF from Forster et al. (2025) and ΔT from C25 (see Section 6).

With finite differences, estimates of the effective λ only become reliable when ΔN and ΔT are sufficiently large, which occurs around 1950 for *C25/AMIP/HadISST1-piForcing* but not before 1990 for *ERSST-piForcing*. *ERSST-piForcing*'s positive feedback before 1990 is due to its unique ΔN and ΔT trajectories (Fig. 2), not its shorter baselines (1871–1900, or 1880–1900 in CAM6); when using the shorter baselines, λ in *C25-piForcing* and *AMIP-piForcing* changes little. Changes in effective λ are smaller than those in the differential λ, but effective λ also becomes much more negative over c. 1975–2005 while differential λ is anomalously negative.

Recent changes in the SST/SIC pattern since 2014 only have a small impact on the effective λ: it is slightly less negative in *C25-piForcing* when the most recent 10 years are included but has changed little since c. 1995 (i.e., since the 1986–2003 window). Despite differential λ over 2001–2023 in *C25-piForcing* approaching λ_{4xCO_2} from coupled models, the effective λ at the end of the record (2006–2023) is still much more negative than λ_{4xCO_2}. Based on this result for effective λ (and further investigation of $\Delta\lambda$ in Section 5), there is still a significant pattern effect when evaluating the historical record as a whole (over 1850–2023). Thus an adjustment for $\Delta\lambda$ is still necessary when estimating ECS per Eq. (4), which we revisit in Section 6.

In summary, we find that c. 1975–2010 is the only period where differential λ in *C25-piForcing*'s ensemble mean is clearly different from λ_{4xCO_2}. The strongly negative differential λ over 1975–2010 has waned, and recent years (especially 2001–2023) show a substantially less-stabilizing λ. Over 2001–2023, the differential λ is nearly back in line with λ_{4xCO_2} in coupled models. Interestingly, the pattern of SST trends since 2001 (Fig. 1) still differs substantially from *abrupt-4xCO$_2$*: recent trends show strongly amplified warming in the North Pacific, which could compensate for the cooling in the central and southeastern Pacific. Thus it could partially be coincidental that the 2001–2023 differential λ and λ_{4xCO_2} are so similar. The effective λ (from differences with respect to 1850–1900) has been relatively constant since 1995 and continues to be much more negative than λ_{4xCO_2} (Fig. 3d–f). Uncertainty in both measures of λ before c. 1975 is large, however.

b. *Sources of uncertainty in feedbacks*

Figure 4a–c shows time-varying spread in estimates of differential λ from the *piForcing* simulations, which arises from different model physics, SST/SIC boundary conditions, and internal variability due to different initial conditions (ICs). Figure B1 shows analogous results for the effective λ. Note that we cannot completely remove the IC spread from estimates of the intermodel or SST/SIC spread with the simulations available; that would require IC ensembles for every SST/SIC and AGCM.

All sources of spread in Fig. 4 show local maxima between 1940–1970, which we attribute to the near-zero trend in T over that period (Fig. 4e). To understand why T trends influence the spread in λ, consider that $\lambda = \mathrm{d}N/\mathrm{d}T$ could be estimated as $\lambda = (\mathrm{d}N/\mathrm{d}t)/(\mathrm{d}T/\mathrm{d}t)$. That alternative method highlights that $\mathrm{d}T/\mathrm{d}t \approx 0$ produces noisy estimates of λ, amplifying spread from all sources. An important

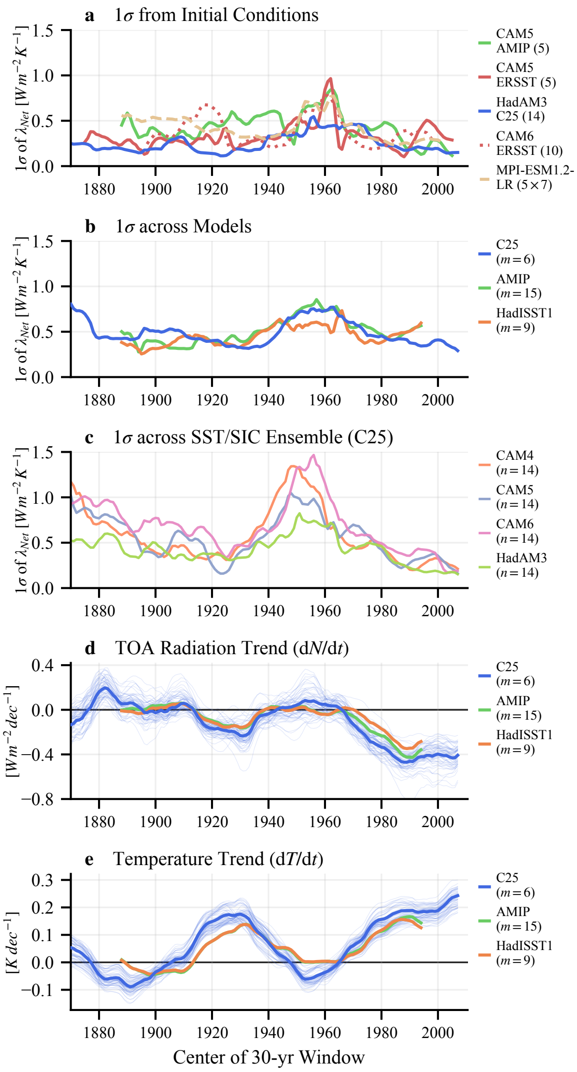

FIG. 4. **Sources of spread in differential feedbacks (λ) over 30-yr windows.** **(a)** Sample standard deviation (1σ) of λ across initial condition (IC) ensembles in various AGCMs, with ensemble size in parentheses; note CAM6 ERSST is from a simulation with time-varying historical forcings (not *piForcing*), and MPI-ESM1.2-LR shows pooled variance from 7 datasets in Modak and Mauritsen (2023). **(b)** 1σ across models using a common SST/SIC dataset, after taking the mean over any IC ensemble members. C25 (Cooper et al. 2025) is based on pooled variance from the three boundary conditions used in all six AGCMs. **(c)** 1σ across C25's SST/SIC boundary conditions for the four AGCMs that used 14 ensemble members. **(d–e)** Multi-model mean of 30-yr trends in N and T, including C25 ensemble members as thin lines.

consideration is that when $dT/dt \approx 0$, regressing annual (instead of 5-year block) means can produce a confident and incorrect estimate of λ due to interannual variability in N and T.

Estimates of IC spread (Fig. 4a) are noisy due to small sample sizes, but the range of 1σ values (typically 0.2–0.5 $\mathrm{W\,m^{-2}\,K^{-1}}$) suggests that IC ensembles of 4–25 members are required to reduce the IC contribution to standard error in differential λ over a 30-year window to below 0.1 $\mathrm{W\,m^{-2}\,K^{-1}}$, although ensemble size could be reduced when the forced trend is large.

We show the intermodel spread (Fig. 4b) from the C25 ensemble (based on the mean intermodel 1σ of the three C25 ensemble members common to all six AGCMs) alongside the spread using 15 AGCMs with AMIP and 9 AGCMs with HadISST1 from Andrews et al. (2022). Intermodel spread in differential λ is similar when quantified using C25, AMIP, or HadISST1.

In Fig. 4c, we show the spread from uncertainty in the SST/SIC BCs, quantified using the C25 ensemble. This spread is largest before 1900 and between 1940–1970; its minimum is at the end of the record, when observational coverage is extensive and forced signals in N and T are large (Fig. 4d–e). Notably, the global-warming rate (dT/dt) is at its maximum at the very end of the record (Fig. 4e). For reference, we also include rolling 1σ for ΔN and ΔT from each source of uncertainty in the Supplemental Information (SI Figs. S1–S2).

For estimates of the effective λ (Fig. B1), atmospheric internal variability from ICs can contribute substantially to spread when the forced signals in ΔN and ΔT are small, but the IC contribution is small after 2010. Intermodel spread is relatively large and approximately constant after 1990, whereas the SST/SIC spread is also large but decreasing. We quantify SST/SIC spread using the C25 ensemble, but note that the SST/SIC spread is much larger if ERSST is included as a plausible estimate of the effective λ.

c. *Component feedbacks: shortwave, longwave, clear-sky, and cloud radiative effect*

Figure 5 shows time-varying components of differential λ, separated by shortwave (SW) versus longwave (LW) and clear sky (CS) versus cloud radiative effects (CRE). SI Figure S3 shows analogous results for the 18-year effective λ. As reported in many analyses of pattern effects and time-varying historical feedbacks, λ_{CRE}^{SW} is responsible for the majority of feedback variations and spread across AGCMs and SST/SIC boundary conditions. Although C25's ensemble-mean λ_{CRE}^{SW} is less variable over the historical record compared to AMIP, HadISST1, and ERSST (Fig. 5a), the range of C25's ensemble members often spans the other datasets' feedbacks (Fig. 5b).

We find substantial differences in λ_{CS}^{SW} across SST/SIC boundary conditions (Fig. 5e), largely due to C25's SIC differing from AMIP's. The AMIP SIC, which is used in all *AMIP/HadISST1/ERSST-piForcing* simulations, produces a λ_{CS}^{SW} that trends positively from approximately 0.5 $\mathrm{W\,m^{-2}\,K^{-1}}$ in 1900 to 1.0 $\mathrm{W\,m^{-2}\,K^{-1}}$ in 1980, then has a strong negative trend after 1980 that yields $\lambda_{CS}^{SW} \approx 0.0$ $\mathrm{W\,m^{-2}\,K^{-1}}$ over 1985–2014; that period approximately

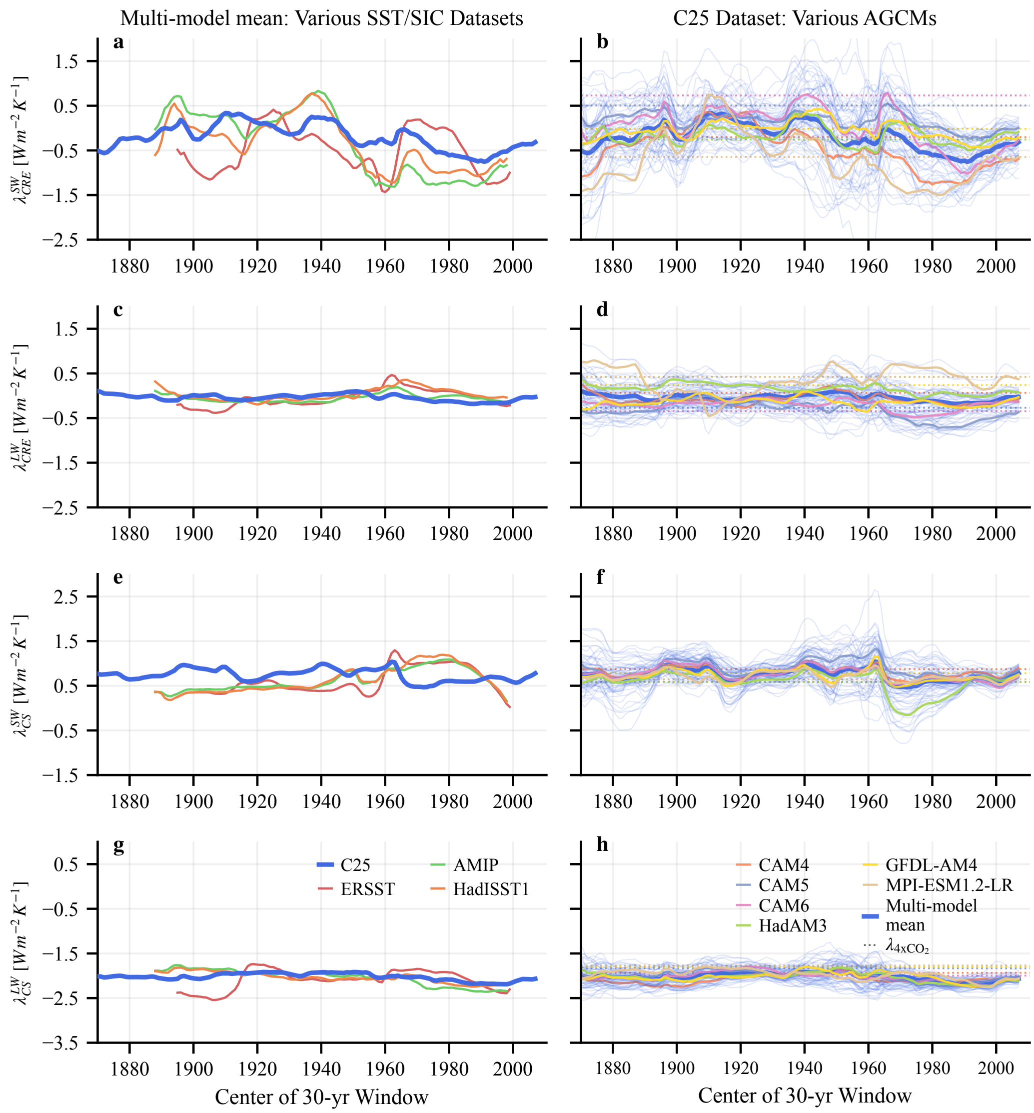

FIG. 5. **Components of the differential feedback (λ) from shortwave (SW) and longwave (LW) cloud radiative effects (CRE) and clear-sky (CS) radiation over 30-yr windows in AGCM *piForcing* simulations.** Left column corresponds to Fig. 3b and shows means across AGCMs for various SST/SIC boundary conditions; C25's multi-model mean is taken after averaging λ across C25 ensemble members within each AGCM. Right column shows the various C25 ensemble members and the C25 ensemble mean within each AGCM, as in Fig. 3c. Component feedbacks from coupled models' *abrupt-4xCO$_2$* simulations are included for comparison.

produces the most-negative λ^{SW}_{CS} over the full record for *AMIP/HadISST1/ERSST-piForcing*. On the other hand, C25 shows less variation in λ^{SW}_{CS} and no trend over 1980–2000. λ^{SW}_{CS} becomes less negative at the end of the record (1994–2023) due to the abrupt loss of Antarctic sea ice (Fig. 2d).

All feedback components become less negative after 2014 in the C25 ensemble (Fig. 5). The positive trend begins earliest for λ^{SW}_{CRE}, starting c. 1990 (i.e., in the 30-year window spanning 1975–2004). All other feedbacks become less negative after the 30-year window centered around 2000 (1985–2014). Thus the recent trend toward less-negative net λ since 2014 is not simply due to shortwave CRE but rather a combined effect due to sea ice (through SW CS), LW CRE, and LW CS.

In general, the ensemble means of C25's component feedbacks are much less variable over the historical record compared to AMIP, HadISST1, and ERSST. However, we caution against overconfidence in the ensemble mean, as C25's ensemble spread leaves ample room for variation in feedbacks beyond that suggested by the means.

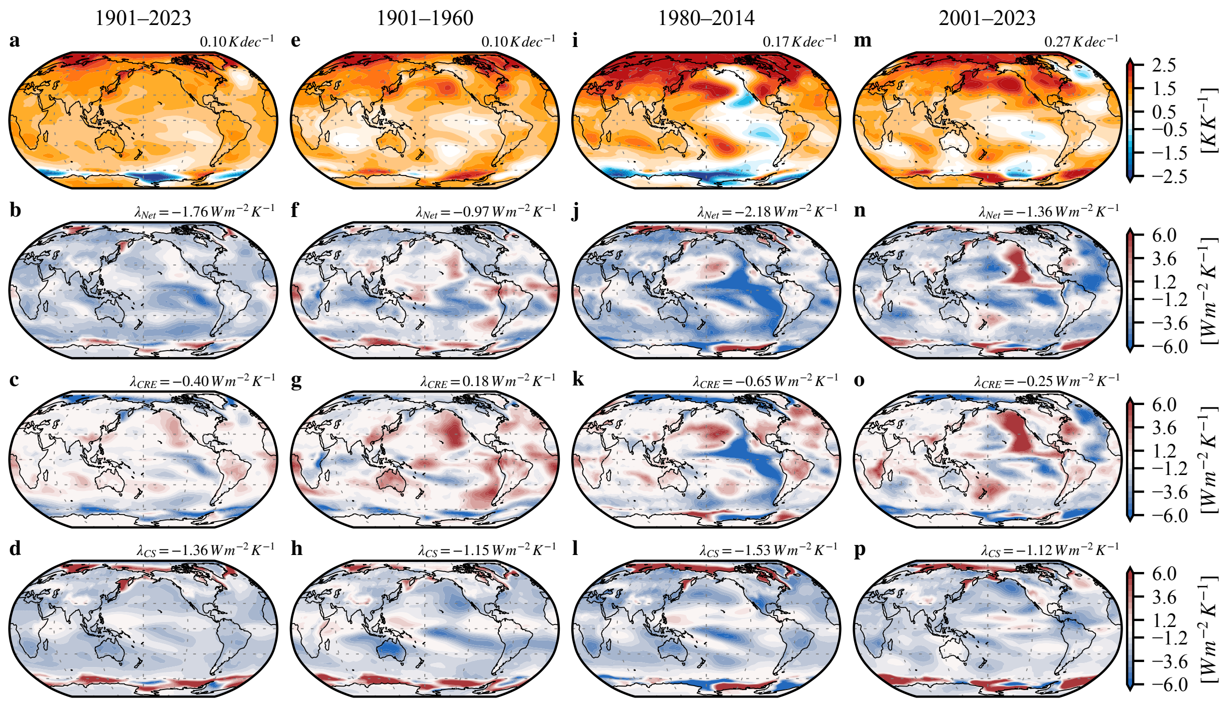

FIG. 6. **Spatial patterns of near-surface air temperature (T) trends and radiative feedbacks in AGCM *piForcing* simulations.** First column **(a–d)** shows results for 1901–2023. **(a)** Multi-model mean of local trends in T from *C25-piForcing* simulations with prescribed SST/SIC from Cooper et al. (2025), divided by global-mean trends. **(b)** Multi-model mean of differential net feedbacks ($\lambda = \mathrm{d}N_{\mathrm{local}}/\mathrm{d}T_{\mathrm{global}}$) from *C25-piForcing* simulations; global-mean λ is shown in upper right. 5-year running means are applied to N and T prior to estimating λ with OLS regression. **(c)** As in panel **b** but for λ from cloud radiative effects (CRE). **(d)** As in panel **b** but for λ from clear-sky (CS) radiation. Columns 2–4 repeat the first column for periods 1901–1960, 1980–2014, and 2001–2023.

In Fig. 6, we show spatial patterns of net, CRE, and clear-sky feedbacks (bottom three rows) alongside T trends (top row) for four periods (columns). Over 1980–2014, net λ is strongly stabilizing (negative) due to cloud feedbacks over the northeast, southeast, and equatorial Pacific Ocean, and clear-sky feedbacks from increasing Antarctic SIC. Comparing 2001–2023 versus 1980–2014, we show that λ_{CRE} over the northeast Pacific Ocean changes sign from negative to positive, while λ_{CRE} over the equatorial and southeast Pacific Ocean remains negative but with reduced magnitude. λ_{CS} becomes positive over the Southern Ocean from major losses of Antarctic sea ice after 2014. The changes in global-mean λ_{CRE} and λ_{CS} are similar for 2001–2023 versus 1980–2014 (both change by $+0.4\ \mathrm{W\,m^{-2}\,K^{-1}}$), but the spatial patterns of λ_{CS} are much steadier over time compared to λ_{CRE}, consistent with the time series in Fig. 5.

d. CERES comparison of TOA trends

Over 2001–2023, CERES observations show a rapid increase in Earth's energy imbalance (ΔN), indicating that ΔF is increasing faster than $\lambda\Delta T$ per Eq. (1). Recent studies have found that AGCM simulations with prescribed SST/SIC and historical forcings slightly underestimate the increases in ΔN, and issues with the prescribed SST/SIC could contribute to the model-observation discrepancy (Raghuraman et al. 2021; Hodnebrog et al. 2024; Fan et al. 2025; Schmidt et al. 2023; Olonscheck and Rugenstein 2024). Our *piForcing* simulations cannot be directly compared with CERES observations because *piForcing* simulations estimate only $\lambda\Delta T$ rather than $\Delta N = \Delta F + \lambda\Delta T$. However, one key aspect of the model-observation discrepancy—Antarctic sea ice and SW clear-sky radiation—appears to be improved in *C25-piForcing*. Comparing SW clear-sky trends over 30–90° S in *piForcing* simulations versus CERES is more reasonable because sea ice (and thus $\lambda\Delta T$) is expected to play a large role relative to ΔF, but the comparison is still imperfect.

Figure 7 shows 2001–2021 trends in SW clear-sky radiation over 30–90°S for CERES, *AMIP/ERSST-piForcing* (which both use the AMIP SIC), and *C25-piForcing*, which assimilates the NOAA/NSIDC CDR satellite product (Meier et al. 2021). Compared to the CERES trend (approximately $+0.25\ \mathrm{W\,m^{-2}\,dec^{-1}}$), *AMIP/ERSST-piForcing* simulations have a trend of the opposite sign (approximately $-0.15\ \mathrm{W\,m^{-2}\,dec^{-1}}$) (Raghuraman et al. 2021; Hodnebrog et al. 2024; Fan et al. 2025). *C25-*

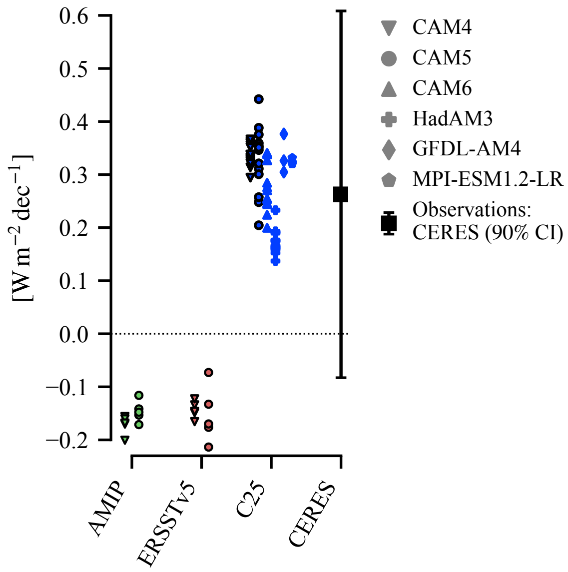

FIG. 7. **2001–2021 trends in shortwave clear-sky radiation (SW CS) over the southern extratropics (30–90°S) in CERES satellite data versus *piForcing* results in atmospheric GCMs.** Note that 30–90°S trends in SW CS are strongly influenced by sea ice concentration (SIC). *AMIP/ERSST-piForcing* include five members from initial-condition ensembles in CAM4 and CAM5, all of which use AMIP's SIC. *C25-piForcing* uses various C25 SST/SIC boundary conditions in six AGCMs, but only CAM4 and CAM5 (dots outlined in black) are directly comparable to AMIP/ERSST results. Datasets have colored dots to match other figures, e.g., Figs. 2–5. Trend error in CERES only accounts for regression uncertainty, which is estimated using the effective degrees of freedom from lag-1 autocorrelation of residuals.

piForcing shows SW CS trends that are similar to CERES, suggesting that much of the reported model-observation discrepancy in SW CS trends over 30–90°S could be due to the issues with AMIP's SIC (see Fig. 2d, described in Section 3b), which also affect HadISST1's SIC. The LW CS trends over 30–90°S in *C25-piForcing* partially offset the change in the SW CS trend, hence the difference in *C25-piForcing*'s net CS trend relative to *AMIP/ERSST-piForcing* is smaller than the difference in SW CS alone (SI Figs. S4–S5). To support future analyses of CERES trends versus AGCM simulations that include forcing (Schmidt et al. 2023), we include additional figures that indirectly compare 2001–2021 *piForcing* results with CERES in SI Figs. S4–S5.

5. The historical pattern effect

How do feedbacks over the full historical record (λ_{Hist}) compare to $\lambda_{2\text{xCO}_2}$ projections? To estimate the historical pattern effect ($\Delta\lambda = \lambda_{2\text{xCO}_2} - \lambda_{\text{Hist}}$), we use our AGCM simulations to estimate λ_{Hist} and coupled simulations of $\lambda_{4\text{xCO}_2}$ in corresponding AOGCMs (Methods).

a. AGCM results for $\Delta\lambda$

Multiple feedback definitions are considered: differential λ from OLS regression over 1871–2023 (only available for *C25-piForcing*) and 1871–2010 (available for other *piForcing* simulations); and effective λ from finite differences, based on the 2006–2023 anomaly with respect to 1850–1900 (available for *C25-piForcing*) and the 1993–2010 anomaly w.r.t. 1871–1900 (available for other *piForcing* simulations). Table 2 summarizes results for both methods and periods. The finite-difference method applied to 2006–2023 aligns with ECS constraints in Section 6, and the differences in $\Delta\lambda$ between periods and methods are described below.

Figure 8a–b shows AGCM results for $\Delta\lambda$ and its components (net, LW CS, SW CS, and total CRE) using regression, and Figure B2 shows analogous results using finite differences. We confirm that net $\Delta\lambda$ is positive ($\lambda_{4\text{xCO}_2} > \lambda_{\text{Hist}}$; data points lie above the 1:1 line) largely due to $\Delta\lambda_{CRE}$, which also has the largest spread among components of $\Delta\lambda$. $\Delta\lambda_{CS}^{LW}$ is also positive, while $\Delta\lambda_{CS}^{SW}$ is near zero with some models slightly negative. AMIP/HadISST1/ERSST estimates of λ_{CS}^{SW}, which all rely on the AMIP SIC, are all less negative than C25's λ_{CS}^{SW}.

C25-piForcing's 14 ensemble members generally span the range (spread in the horizontal direction) of feedbacks produced using other datasets, although AMIP/HadISST1/ERSST often fall near the ends of the C25 ensemble. For five of the six models with *C25-piForcing* simulations, the ensemble-mean net $\Delta\lambda$ in C25 (the top of the blue bars in Fig. 8b) has a smaller magnitude than the mean AMIP $\Delta\lambda$ (green dots) but larger than the ERSST and HadISST1 $\Delta\lambda$ (red and orange dots); in HadAM3, AMIP and C25 have similar $\Delta\lambda$. If we focus on the common period of 1871–2010 and the six models that have *C25-piForcing* simulations, we find that *AMIP-piForcing*'s mean $\Delta\lambda$ of 0.77 W m^{-2} K^{-1} is larger than *C25-piForcing*'s value of 0.61 W m^{-2} K^{-1} (from regression over 1871–2010, Table 2).

Table 2 shows that differences in $\Delta\lambda$ between the finite-difference and regression methods can be large for the period ending in 2010 (0.16 W m^{-2} K^{-1} for C25's mean) but appear smaller for the period ending in 2023 (0.05 W m^{-2} K^{-1} for C25's mean). Differences between the late (end in 2023) and early (end in 2010) periods are 0.02 W m^{-2} K^{-1} for regression and −0.09 W m^{-2} K^{-1} for finite differences, based on C25's mean.

The similarity between regression estimates over 1871–2010 (0.61 W m^{-2} K^{-1}) and 1871–2023 (0.63 W m^{-2} K^{-1}) could seem surprising, given that differential λ has changed substantially since 2010 (Fig. 3a–c). We show Gregory plots in Fig. A2 that clarify these results: the strongly negative λ over 1975–2014 was rather brief with relatively small increases in T (because of the negative λ), and its data fall both above and below the longer-term λ_{Hist}. Thus

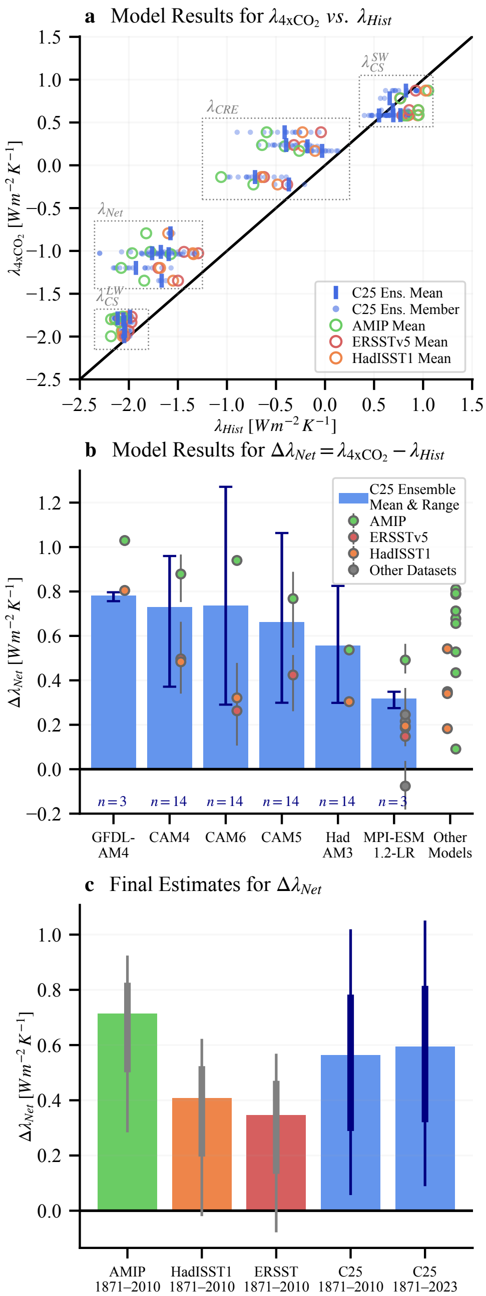

FIG. 8. **Historical feedbacks (λ_{Hist}) and pattern effects ($\Delta\lambda = \lambda_{4xCO_2} - \lambda_{\mathrm{Hist}}$). (a)** λ_{4xCO_2} from coupled models vs. λ_{Hist} from *piForcing* in AGCMs. Results show six AGCMs with *C25-piForcing* simulations. AMIP/ERSST/HadISST1 use 1871–2010, whereas C25 uses 1871–2023; results are similar if C25 uses 1871–2010. **(b)** Net $\Delta\lambda$ using results from panel **a**. The number of C25 simulations for each AGCM is shown on the horizontal axis. Gray errors (AMIP, ERSST, HadISST1, and Other Datasets) are ranges from initial condition ensembles. Other Models are listed in Table 1. **(c)** Median estimates of $\Delta\lambda$ from combining intermodel and SST/SIC spread with a crossed random-effects model. Errors denote 66% (thick) and 90% (thin) ranges; C25 ranges include both intermodel and SST/SIC spread.

differential λ_{Hist} is barely changed by including 2010–2023 because those data fall along the same line, whereas effective λ_{Hist} is slightly more affected because it depends only on the endpoints. Figure A2 also illustrates how the differential λ from short windows (e.g., 1980–2014 or 2001–2023) can be misleading if assumed to hold for longer-term warming.

For *ERSST-piForcing*, the $\Delta\lambda$ estimates are extremely sensitive to the method: regression produces a positive $\Delta\lambda = 0.33$ W m^{-2} K^{-1} while finite differences produce a negative value of $\Delta\lambda = -0.38$ W m^{-2} K^{-1} (Table 2). The discordant results for ERSST appear to be due to its large changes in ΔT and ΔN that occur around the early twentieth century, which create a persistent offset relative to other datasets (Fig. 2a–b). A statistical explanation is that the effective λ depends wholly on how the end of the record compares to the pre-1900 mean, whereas the differential λ is strongly influenced by the most extreme values of ΔN and ΔT regardless of their timing; ERSST's extremes occur after 1900, so the pre-1900 mean has less influence on its regression. A physical explanation could be that ERSST cools strongly in tropical convective regions over 1880–1940, especially in the West Pacific, which have a strong influence on N. This strong trend is clear in time series of tropical SST$^{\#}$, a metric that represents the contrast between the warmest convective regions and cooler subsiding regions; 1880–1940 trends in SST$^{\#}$ are weaker/insignificant in C25, AMIP, and HadISST1 (Fueglistaler and Silvers 2021; Cooper et al. 2025).

Figure 9 and the 1σ values in Table 2 attempt to distinguish spread from initial conditions (ICs), model physics, and SST/SIC boundary conditions for the differential λ, and we later address combining the uncertainties in Section 5b. Figure B3 shows analogous results for the effective λ from finite differences. We show variances (rather than standard deviations) because they are additive for independent sources of error. We do not have the exhaustive suite of simulations required to completely remove IC spread from estimates of the intermodel and SST/SIC spreads, but we find that IC spread is much smaller than the other sources when evaluating $\Delta\lambda$ over the entire record.

Figure 9a shows the available IC ensembles for model–dataset pairs; the pooled IC variance for 1871–2010 across AGCMs is approximately 0.08^2 [W m^{-2} K^{-1}]^2. Although sample sizes are small (5–15 members), it appears that CAM4, CAM5, and CAM6 have more IC spread than MPI-ESM1.2-LR and HadAM3. The HadAM3 IC ensemble using a single C25 member is the largest ensemble (15 members), and a 5–95% range on its sample variance subsampled to 5 members (from bootstrap resampling 10,000 subsets of 5 members) does not overlap with the spread from any of CAM4/5/6's IC ensembles.

Differences in IC spread could be partly from AGCMs having different magnitudes of internal atmospheric variability in N and T. The relative magnitude of an-

TABLE 2. Feedbacks from *piForcing* simulations in AGCMs. Values shown include results from this study using C25 SST/SIC (Cooper et al. 2025), AMIP, and ERSST, plus results from Andrews et al. (2022) and Modak and Mauritsen (2023). Finite difference columns are based on mean anomalies over 1993–2010 w.r.t. 1871–1900 and 2006–2023 w.r.t. 1850–1900. For multi-model means, we average ensemble members within AGCMs, then average across AGCMs for equal weighting. Sample standard deviations (1σ) are calculated across boundary conditions (BCs), initial conditions (ICs), or AGCMs depending on the row. All rows with n IC > 1 show 1σ from IC spread; C25 rows with various AGCMs show spread across the 3–14 SST/SIC BCs, but there is a contribution from IC spread given that each C25 BC has only one IC member; the C25 mean shows spread across the six AGCMs, which is a mean of three models' estimates of the 1σ from the three C25 ensemble members that are used in all six AGCMs; the C25 mean intentionally excludes SST/SIC spread because only four of the six AGCMs used all 14 SST/SIC BCs; AMIP mean shows spread across AGCMs for the same six AGCMs that have *C25-piForcing* simulations and separately for the 15 AGCMs with *AMIP-piForcing* available; note that we first average over ICs where available, but many *AMIP-piForcing* simulations have only one ensemble member; ERSST/HadISST1 means show spread across AGCMs after first averaging over ICs where available.

					OLS Regression						**Finite Differences**					
					1871–2010			**1871–2023**			**1993–2010**			**2006–2023**		
SST	**AGCM**	***n* BC**	***n* IC**	**AGCMs**	λ_{Hist}	$\Delta\lambda$	1σ	λ_{Hist}	$\Delta\lambda$	1σ	λ_{Hist}	$\Delta\lambda$	1σ	λ_{Hist}	$\Delta\lambda$	1σ
C25	GFDL-AM4	3	1		-1.56	0.77	0.07	-1.58	0.78	0.02	-1.72	0.92	0.08	-1.65	0.86	0.10
C25	MPI-ESM1.2-LR	3	1		-1.68	0.34	0.04	-1.67	0.32	0.04	-1.80	0.45	0.07	-1.69	0.35	0.07
C25	HadAM3	14	1		-1.64	0.60	0.19	-1.59	0.56	0.14	-1.76	0.72	0.19	-1.60	0.56	0.12
C25	CAM4	14	1		-1.87	0.67	0.22	-1.93	0.73	0.19	-2.00	0.80	0.26	-1.96	0.76	0.18
C25	CAM5	14	1		-1.66	0.65	0.26	-1.67	0.66	0.20	-1.86	0.85	0.27	-1.75	0.74	0.18
C25	CAM6	14	1		-1.65	0.62	0.36	-1.76	0.74	0.28	-1.88	0.86	0.43	-1.85	0.82	0.24
C25	Mean	3–14		6	-1.68	0.61	0.16	-1.70	0.63	0.18	-1.84	0.77	0.21	-1.75	0.68	0.20
C25	HadAM3 (IC ens.)	1	15		-1.66	0.62	0.05	-1.63	0.59	0.03	-1.78	0.74	0.07	-1.57	0.53	0.04
AMIP	GFDL-AM4	1	1		-1.82	1.03					-1.95	1.16				
AMIP	MPI-ESM1.2-LR	1	5		-1.84	0.49	0.05				-1.97	0.62	0.04			
AMIP	HadAM3	1	1		-1.57	0.54					-1.78	0.74				
AMIP	CAM4	1	5		-2.08	0.88	0.08				-2.20	1.00	0.11			
AMIP	CAM5	1	5		-1.78	0.77	0.13				-2.07	1.06	0.14			
AMIP	CAM6	1	1		-1.97	0.94					-2.30	1.27				
AMIP	Mean (C25 group)	1		6	-1.84	0.77	0.22				-2.05	0.98	0.25			
AMIP	Mean (all)	1		15	-1.62	0.68	0.23				-1.79	0.84	0.31			
ERSST	CAM4	1	5		-1.70	0.50	0.13				-0.73	-0.47	0.12			
ERSST	CAM5	1	5		-1.44	0.42	0.10				-0.77	-0.24	0.17			
ERSST	CAM6	1	10		-1.29	0.27	0.10				-0.70	-0.33	0.16			
ERSST	MPI-ESM1.2-LR	1	5		-1.49	0.15	0.04				-0.86	-0.49	0.08			
ERSST	Mean	1		4	-1.48	0.33	0.16				-0.76	-0.38	0.12			
HadISST1	Mean	1		9	-1.36	0.39	0.19				-1.52	0.55	0.24			

nual intra-ensemble variance in N pooled over all shared years (1880–2010) and datasets with IC ensembles are (units $[\mathrm{W\,m^{-2}}]^2$): 0.026 (HadAM3), 0.043 (MPI-ESM1.2-LR), 0.044 (CAM5), 0.049 (CAM4), and 0.064 (CAM6). The pooled annual variance for T differs less across AGCMs in *piForcing* simulations (units K^2): 0.0010 (HadAM3), 0.0016 (MPI-ESM1.2-LR), 0.0011 (CAM5), 0.0012 (CAM4), and 0.0013 (CAM6). Including the additional 14 simulation years (1871–2023 instead of 1871–2010) substantially reduces spread in $\Delta\lambda$ from ICs based on the HadAM3 ensemble, which appears due to a larger signal-to-noise ratio from changes in N and T since 2010 and can also be seen in time series of spread sources for the effective feedback (Fig. B1a).

Figure 9b compares SST/SIC spread using the C25 ensemble with intermodel spread using AMIP and HadISST1 (Andrews et al. 2022). It is a noteworthy result that the spread from SST/SIC uncertainty is comparable to or larger than the intermodel spread across the 15 AGCMs with *AMIP-piForcing* simulations. Error ranges (5–95% from bootstrap resampling) on the variance estimates are substantial and typically overlap across the four AGCMs with full C25 SST/SIC ensembles. However, paired permutation tests on the variance differences indicate that CAM6 has larger SST/SIC spread than HadAM3 (statistically significant at $p = 0.03$), while the CAM6–CAM4 difference is marginal ($p = 0.07$). CAM4/5/6 simulations have identical resolution, so the increasing sensitivity to SST/SIC uncertainty between CAM4 and CAM6 could be related to model complexity.

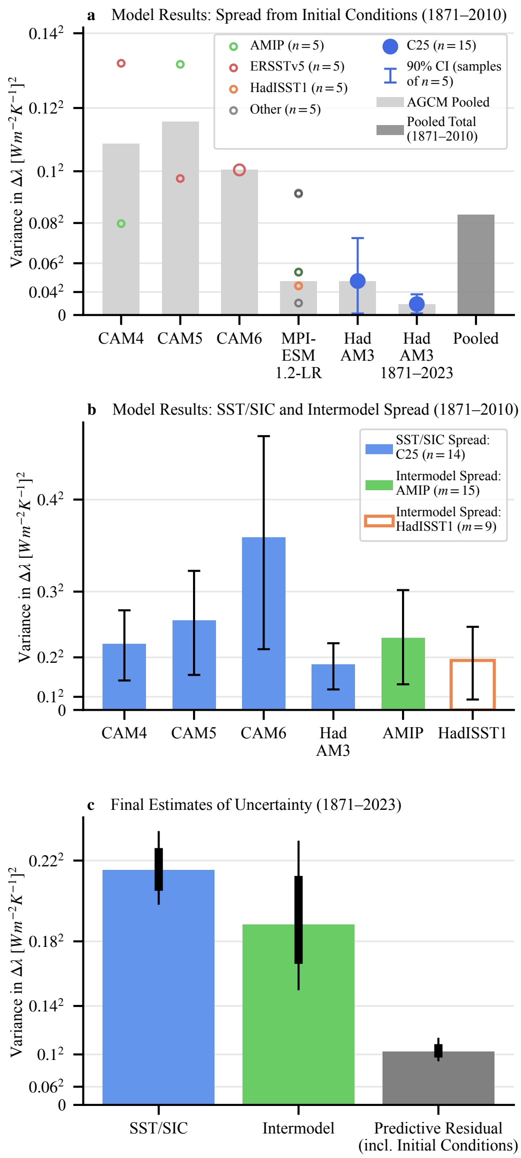

FIG. 9. **Sources of spread in historical pattern effects ($\Delta\lambda$). (a)** Sample variance from initial conditions (ICs) using various AGCMs and SST/SIC boundary conditions. Bars show pooled variance over 1871–2010, except for 1871–2023 in HadAM3. Circles show individual IC ensembles. HadAM3 shows 90% ranges from bootstrap subsampling to 5 members, testing whether the spread differs from other AGCMs' smaller ensembles. **(b)** Sample variance using 1871–2010 across C25's SST/SIC in various AGCMs, compared with sample variance from intermodel spread across AGCMs using AMIP/HadISST1 (Andrews et al. 2022). Errors are 90% ranges using bootstrap resampling. **(c)** Spread from various sources for 1871–2023 based on the crossed random-effects model. Errors are 66% (thick) and 90% (thin) ranges. SST/SIC and intermodel spread are structural errors, whereas the predictive residual represents error for individual $\Delta\lambda$ estimates, given an AGCM and SST/SIC, largely from ICs.

b. Crossed random-effects model for $\Delta\lambda$

We have many estimates of $\Delta\lambda$ (Table 2) from different AGCMs, SST/SIC boundary conditions, and time periods. A best estimate of $\Delta\lambda$ and its uncertainty should incorporate both the broad range of SST/SIC patterns across the C25 ensemble and the full suite of AGCMs with $\Delta\lambda$ estimates using other SST/SIC datasets. To produce this best estimate of $\Delta\lambda$, we combine our C25 ensemble with the full suite of AGCMs in Andrews et al. (2022) using a Bayesian hierarchical model with "crossed random effects" (Gelman and Hill 2006). We estimate group-specific offsets ("random effects") for each AGCM and SST/SIC, which are "crossed" because any SST/SIC could be prescribed in any AGCM. The goal is to answer this question: if we were able to run all 14 *C25-piForcing* ensemble members in all 15 AGCMs with *AMIP-piForcing* simulations, what would be our estimate of $\Delta\lambda$ and its uncertainty?

Let $\Delta\lambda_{m,bc,t}$ represent the $\Delta\lambda$ for a given AGCM m, boundary condition bc, and time period t. Assuming $\Delta\lambda_{m,bc,t} \sim \mathcal{N}(\mu_{m,bc,t}, \sigma)$ with mean $\mu_{m,bc,t}$ and standard deviation σ (for all m, bc, t), the crossed random-effects model is

$$\mu_{m,bc,t} = \alpha + \beta_t + u_m + v_{bc}, \tag{5}$$

where α represents the average $\Delta\lambda$ for the reference period that is common across all AGCM simulations and SST/SIC datasets (1871–2010 using OLS regression; 1993–2010 w.r.t. 1871–1900 using finite differences), β_t is the incremental $\Delta\lambda$ if post-2010 data are included (i.e., the period is changed to 1871–2023 using OLS regression, or 2006–2023 w.r.t. 1850–1900 using finite differences), u_m is the AGCM-specific offset, and v_{bc} is the BC-specific offset. The random effects are $u_m \sim \mathcal{N}(0, \tau_{\text{model}})$ and $v_{bc} \sim \mathcal{N}(0, \tau_{\text{BC}})$. Time period ($\beta_t$) is treated as a fixed effect because that term estimates a single offset from changing between two periods (e.g., 1871–2010 versus 1871–2023) across the C25 ensemble members. We found that treating the period as part of the BC random effect produced similar results. We fit separate models based on our regression and finite differences results, so only two time periods are included for each fit, and β_t is only informed by C25. We include CAM6 ERSST estimates of $\Delta\lambda$ despite those simulations beginning in 1880 instead of 1871; excluding 1871–1879 from CAM4, CAM5, and MPI-ESM1.2-LR regression estimates of ERSST's $\Delta\lambda$ changed the result by only ±0.01 in each AGCM.

Model fitting uses Bambi/PyMC's Bayesian method (Capretto et al. 2022), which samples from the joint posterior distribution of fixed effects, random effects, and variance parameters. The Markov Chain Monte Carlo algorithm repeatedly proposes combinations of the parameters, and proposals are retained more frequently when they make the $\Delta\lambda$ data more likely while being consistent with the priors. Bambi employs PyMC's No-U-Turn Sampler (Hoffman and Gelman 2014), an adaptive Hamiltonian

TABLE 3. Summary of posterior best estimates for $\Delta\lambda$ using a crossed random-effects model. Finite-difference columns use mean anomalies over 1993–2010 w.r.t. 1871–1900 and 2006–2023 w.r.t. 1850–1900.

		OLS Regression						Finite Differences					
		1871–2010			1871–2023			1993–2010			2006–2023		
SST	*n* BC	$\Delta\lambda$	1σ	5–95% range	$\Delta\lambda$	1σ	5–95% range	$\Delta\lambda$	1σ	5–95% range	$\Delta\lambda$	1σ	5–95% range
C25	14	0.56	0.28	[0.06, 1.02]	0.59	0.28	[0.09, 1.05]	0.70	0.33	[0.04, 1.12]	0.62	0.33	[-0.05, 1.03]
AMIP	1	0.71	0.19	[0.28, 0.92]				0.90	0.25	[0.27, 1.14]			
ERSST	1	0.35	0.19	[-0.08, 0.57]				-0.37	0.26	[-1.00, -0.11]			
HadISST1	1	0.41	0.19	[-0.02, 0.62]				0.56	0.26	[-0.07, 0.80]			

Monte Carlo, which uses gradients of the log posterior to efficiently explore the parameter space. After warmup, the retained draws approximate the joint posterior distribution of the model parameters.

We use weakly informative priors (units $\mathrm{W\,m^{-2}\,K^{-1}}$): $\alpha \sim \mathcal{N}(0.5, 1.5)$, $\beta \sim \mathcal{N}(0, 0.2)$, $\tau_{\mathrm{model}}, \tau_{\mathrm{BC}} \sim$ HalfNormal(0.7), and $\sigma \sim$ HalfNormal(0.15). The posterior mean and range were not sensitive to changes in the prior, e.g., changing to $\alpha \sim \mathcal{N}(0.0, 1.5)$, unless the priors were restrictive. The posterior means (± standard deviation) using the regression estimates are $\alpha = 0.53 \pm 0.09$, $\beta = 0.03 \pm 0.02$, $\tau_{\mathrm{model}} = 0.21 \pm 0.05, \tau_{\mathrm{BC}} = 0.23 \pm 0.05$, and $\sigma = 0.10 \pm 0.01$ $\mathrm{W\,m^{-2}\,K^{-1}}$. Posteriors using finite-difference estimates are $\alpha = 0.59 \pm 0.12$, $\beta = -0.09 \pm 0.02$, $\tau_{\mathrm{model}} = 0.29 \pm 0.07, \tau_{\mathrm{BC}} = 0.36 \pm 0.07$, and $\sigma = 0.13 \pm 0.01$ $\mathrm{W\,m^{-2}\,K^{-1}}$. The predictive residual variance σ^2 represents the remaining spread in an individual estimate of $\Delta\lambda$ after accounting for AGCM, SST/SIC, and time-period effects. For example, atmospheric internal variability from ICs likely comprises much of the predictive residual. Note that these posteriors only describe the fitted model; they are not the final $\Delta\lambda$ estimates reported below, which are separated by dataset.

The final $\Delta\lambda$ estimates come from posterior predictions of $\mu_{m,bc,t}$ for every AGCM, SST/SIC boundary condition, and time period from each posterior draw. For quantities involving multiple BCs and models, such as the C25 5–95% range, we pool the relevant predicted $\mu_{m,bc,t}$ values across posterior draws, AGCMs, and SST/SIC boundary conditions, and summarize the resulting distribution.

We show the results of the crossed random-effects model in Table 3. Figures 8c and 9c use differential λ, while Figs. B2c and B3c use effective λ. Because the six models with *C25-piForcing* simulations have a slightly larger mean $\Delta\lambda$ in their *AMIP-piForcing* simulations compared to the other AGCMs (Table 2), the crossed random-effects model's estimates of C25's mean $\Delta\lambda$ for all 15 AGCMs are slightly smaller than the direct estimates from the six AGCMs with *C25-piForcing* (Tables 2 and 3). C25's central estimate from OLS regression for 1871–2010 is between AMIP and HadISST1/ERSST. AMIP is at the high end of C25's 66% range, while HadISST1 and ERSST are near the low end. However, using finite differences to estimate $\Delta\lambda$ places ERSST (with its negative $\Delta\lambda$ of -0.37 $\mathrm{W\,m^{-2}\,K^{-1}}$) far outside of C25's 90% range (Tables 2–3).

C25's estimates of $\Delta\lambda$ and uncertainty through 2023 are consistent using regression (0.59 $\mathrm{W\,m^{-2}\,K^{-1}}$, 5–95%: 0.09 to 1.05) or finite differences (0.62 $\mathrm{W\,m^{-2}\,K^{-1}}$, 5–95%: -0.05 to 1.03). SST/SIC appears to be the largest source of spread using regression over 1871–2023 (Fig. 9c). The residual predictive variance, given an AGCM and SST/SIC, is 0.10^2 $[\mathrm{W\,m^{-2}\,K^{-1}}]^2$, similar to but slightly larger than the pooled IC spread alone (Fig. 9a). Using finite differences, intermodel spread appears to contribute more to uncertainty than does SST/SIC, but this is only true if SST/SIC's contribution is limited to C25's ensemble; if AMIP/HadISST1/ERSST datasets are included in the spread from SST/SIC, then SST/SIC is the dominant source of uncertainty (Fig. B3c).

In summary, we have quantified the spread in $\Delta\lambda$ from uncertainty in historical SST/SIC and model physics and find that SST/SIC tends to be the largest source of uncertainty. Next, we revise ECS constraints based on our estimates of $\Delta\lambda$ and its uncertainty. To be consistent with the ECS methods in Section 6, we select the finite-difference estimate of $\Delta\lambda$ based on 2006–2023 mean anomalies relative to 1850–1900. We use results from C25's SST/SIC ensemble and assign $\Delta\lambda$ a median of 0.62 (-0.05 to 1.03, 5–95%) $\mathrm{W\,m^{-2}\,K^{-1}}$ (Table 3). If we were to use the full posterior of the crossed random effects model, i.e., $\alpha + \beta_t$ from Eq. (5), which includes ERSST, AMIP, and HadISST1 BCs, the median would be 0.51 $\mathrm{W\,m^{-2}\,K^{-1}}$. Note that C25's median is essentially unchanged if we use OLS regression instead of finite differences. A key point is that our $\Delta\lambda$ estimates align with Sherwood et al. (2020), although our central estimate's magnitude is larger by 0.12 $\mathrm{W\,m^{-2}\,K^{-1}}$, while σ is larger by only 0.03 $\mathrm{W\,m^{-2}\,K^{-1}}$.

6. Climate sensitivity

a. Revisions to components of the historical energy budget

Our ECS revisions consist of 1) our estimate of $\Delta\lambda$ and its uncertainty and 2) estimates of ΔT, ΔN, and ΔF through 2023. We follow the methods of Sherwood et al. (2020), "SW20" hereafter, in using the following equation for the historical energy budget:

$$\Delta T = -\frac{\Delta F - \Delta N}{\lambda_{2\mathrm{xCO_2}} - \Delta\lambda}, \tag{6}$$

where λ is related to the effective climate sensitivity (S) defined in SW20 by $S = -\Delta F_{2\mathrm{xCO_2}}/\lambda_{2\mathrm{xCO_2}}$. SW20 used differences between means over 2006–2018 and 1861–1880 for ΔT, ΔN, and ΔF, but they showed that results were similar using 1850–1900 as the preindustrial baseline. SW20 estimated $\Delta\lambda \sim \mathcal{N}(\mu = 0.5, \sigma = 0.3)$ W m^{-2} K^{-1} based primarily on Andrews et al. (2018), which used OLS regression over 1871–2010 with the AMIP dataset.

We obtain a revised estimate of $\lambda_{2\mathrm{xCO_2}}$ and S by using our best estimate of $\Delta\lambda$ (0.62 W m^{-2} K^{-1}, 5–95% from −0.05 to 1.03 W m^{-2} K^{-1}; Section 5b) and ΔT, ΔN, and ΔF from differences between the period means over 2006–2023 and 1850–1900, as described below.

We assign $\Delta T \sim \mathcal{N}(1.13, 0.12)$ K based on the C25 reanalysis; σ includes the spread across C25's ensemble members (0.10 K), plus SW20's estimate of the uncertainty contribution from internal variability of 0.07 K, added in quadrature. 0.07 K is a slight overestimate given that we are averaging over more years compared to SW20, which assigned $\Delta T \sim \mathcal{N}(1.03, 0.09)$ K. C25's median ΔT is larger than the extended IPCC AR6 estimate using blended surface temperature (1.07 K) and is more aligned with DCENT-I (1.15 K). C25 has larger uncertainty than DCENT-I (σ = 0.10 K versus 0.05 K), possibly due to C25's ensemble having temporal correlation whereas DCENT-I has independent infilling at each time step.

We assign $\Delta N \sim \mathcal{N}(0.71, 0.20)$ W m^{-2} based on extended IPCC AR6 estimates for 2006–2023 (Forster et al. 2025), which compares to $\mathcal{N}(0.6, 0.18)$ W m^{-2} in SW20's baseline. We follow SW20 in assuming an imbalance of 0.2 W m^{-2} over 1850–1900 with 5–95% range of 0.0–0.4 W m^{-2}, which SW20 assessed to span values from AOGCMs (Lewis and Curry 2015), energy-balance modeling (Armour 2017), and inverse modeling of ocean heat uptake from SST reconstructions (Gebbie and Huybers 2019; Zanna et al. 2019). Our range for ΔN appears broadly consistent with Wu et al. (2025)'s more recent reconstruction of ocean heat uptake, which found $\Delta N = 0.78 \pm 0.27$ (2σ) W m^{-2} for 2010–2020 relative to 1870–1880. We use Forster et al. (2025)'s error estimates for 2006–2023 and add the preindustrial error in quadrature. We also add an uncertainty contribution of 0.07 W m^{-2} from internal variability following SW20, although this slightly overestimates the error because we are averaging more years.

Revisions to ΔF cause the most substantial change relative to SW20. We use Forster et al. (2025)'s ΔF, which is produced from an ensemble time series with 100,000 members (Smith et al. 2025). ΔF for 2006–2023 has a median of 2.61 (1.98 to 3.25, 5–95%) W m^{-2}, which compares to 1.83 (−0.03 to 2.71, 5–95%) W m^{-2} for 2006–2018 in SW20. Unlike SW20's ΔF, skewness is approximately zero in Forster et al. (2025). For reference, IPCC AR6 reported ΔF for 2006–2019 compared to 1850–1900 of 2.20 (1.53 to 2.91, 5–95%) W m^{-2} (Forster et al. 2021).

ΔF consists of CO_2 forcing, which has increased its mean from 1.73 W m^{-2} (2006–2018) to 1.78 W m^{-2} (2006–2023), and non-CO_2 forcing, which includes non-CO_2 greenhouse gases, aerosols, and other forcing agents. For aerosols, SW20 used Bellouin et al. (2020)'s unconstrained range, which excludes energy-budget constraints to avoid circularity with constraints on climate sensitivity. IPCC AR6's main assessment of ΔF also excludes energy-budget constraints on aerosol ERF (as described by Forster et al. 2021), but their range is narrower than SW20's.

The key difference in IPCC AR6's ΔF (whose methods we adopt here) is the narrower range from aerosol-cloud interactions (ERFaci), discussed by Forster et al. (2021) and Lewis (2023). In SW20, the ERFaci distribution is skewed toward negative values, whereas IPCC AR6 is approximately normal. IPCC AR6's range reflects a convergence of observational and model-based estimates of ERFaci, which do not support total aerosol forcing being more negative (causing cooling) than −2.0 W m^{-2}. Down-weighting the likelihood of very negative aerosol forcing also reduces the likelihood of high ECS; strong aerosol cooling relies on high ECS to explain the historical temperature record. Multiple studies since IPCC AR6 have examined ERFaci (e.g., Possner et al. 2020; Glassmeier et al. 2021; Wall et al. 2022; Zelinka et al. 2023; Michibata et al. 2025; Duran et al. 2025; Park et al. 2025; Zelinka et al. 2026; Roi-Cohen et al. 2026; Yuan et al. 2026). Their findings vary, but none support a skewed distribution toward very negative ERFaci. We therefore adopt Forster et al. (2025)'s estimates of ΔF, given that a comprehensive assessment of ERFaci is beyond the scope of this study.

b. Results for climate sensitivity

Figure 10 shows the historical likelihood and combined evidence for S. In terms of the maximum likelihood from historical evidence alone (Fig. 10a), we find that updating only $\Delta\lambda$ leads to higher S of 4.2 K versus 3.7 K in SW20. Updating ΔN or ΔT also shifts the maximum likelihood to higher S. However, updating ΔF through 2023 with IPCC AR6 methods (Forster et al. 2025) substantially lowers the likelihood of high S values and reduces the maximum likelihood to 3.4 K. Pattern effects continue to have a large impact on the maximum likelihood: setting $\Delta\lambda = 0$ reduces the most likely value of S to 2.3 K and reduces the high tail to normalized likelihoods less than 0.2 at S = 4.0 K.

When combined with SW20's process and paleoclimate evidence, our revision of the historical evidence (for $\Delta\lambda$, ΔT, ΔN and ΔF through 2023) does not have a large impact on the combined PDF (Fig. 10b) for S (median 3.0 K,

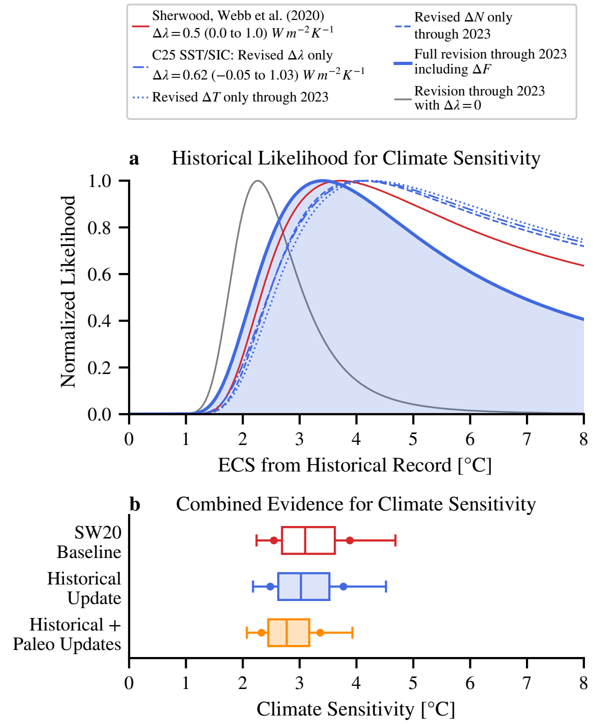

FIG. 10. **Climate sensitivity to a doubling of CO_2 from the historical and combined lines of evidence.** **(a)** Normalized likelihoods (maximum of 1.0) from historical evidence following SW20 (Sherwood et al. 2020) and including revisions to the historical pattern effect ($\Delta\lambda$) from this study, ΔT from Cooper et al. (2025), and ΔN and ΔF through 2023 from Forster et al. (2025). The likelihood with $\Delta\lambda = 0$ shows the impact of neglecting pattern effects. **(b)** Probability distributions for climate sensitivity after combining historical with process and paleoclimate evidence, assuming a uniform-λ prior. SW20's baseline is shown (in red) for comparison with the full historical revision from this study (in blue); the result if paleoclimate evidence is also revised following Cooper et al. (2024, 2026) is included (in orange).

5–95%: 2.2–4.5 K) compared to SW20 (3.1 K, 5–95%: 2.2–4.7 K) because SW20's upper bound was constrained most strongly by paleoclimate evidence; it reduces the 95% bound by 0.2 K and the median by 0.1 K.

Accounting for pattern effects in the paleoclimate evidence, which was not done in SW20, puts an even stronger constraint on high ECS (Cooper et al. 2024, 2026). If we combine our revised historical likelihood with these paleoclimate revisions, the posterior median becomes 2.8 K (5–95%: 2.1–3.9 K).

SW20 also presented a robust range that spanned various robustness tests, and they found that switching from the baseline's uniform-λ prior to a uniform-S prior generally spanned the robustness tests. We report ranges from the uniform-S prior as an approximation of the robust range: for the historical revision alone, the uniform-S prior produces a median of 3.4 K (2.4–5.4 K, 5–95%); after combining with Cooper et al. (2024, 2026), we find a median of 3.0 K (2.2–4.4 K, 5–95%).

7. Conclusions

Historical feedbacks depend on spatial patterns of SST and sea ice, which are uncertain over the entire historical record (1850–present). The uncertainty is especially large in earlier decades because of the sparseness of observations, yet inter-dataset differences are also large in recent decades because of errors from homogenizing data sources (Fig. 1). To quantify how SST/SIC uncertainty, intermodel spread, and atmospheric internal variability affect feedback estimates, we ran simulations in six atmospheric models using SST/SIC ensemble members (3–14 per model) from Cooper et al. (2025)'s coupled reanalysis, alongside the AMIP, HadISST1, and ERSST datasets used in previous studies.

Time-varying feedbacks. We consider two definitions of time-varying feedbacks: the differential feedback (from regression over 30-year windows) and the effective feedback (from finite differences between the mean anomaly over rolling 18-year windows and the preindustrial mean). The effective feedback is more applicable to estimates of climate sensitivity, whereas the 30-year differential feedback illustrates decadal variability from changing SST/SIC patterns and the potential problems that arise when extrapolating a short-term feedback to long-term warming. Over most of the historical record, the ensemble mean of differential feedbacks from Cooper et al. (2025) is largely consistent with coupled models' $4xCO_2$ feedbacks (Fig. 3), whereas results based on other SST datasets tend to show more-negative (stabilizing) feedbacks in the early 20^{th} century and larger variations before c. 1960 (Gregory and Andrews 2016; Andrews et al. 2022; Modak and Mauritsen 2023). Our results agree with previous studies in finding c. 1975–2014 to be an exceptional period with anomalously negative (stabilizing) feedbacks, although this period appears even more anomalous relative to the smaller variations before 1975 in results using Cooper et al. (2025).

A major update is that the differential feedback has become much less stabilizing since 2014 according to both prescribed-SST/SIC simulations and CERES-based observational estimates, although the effective feedback has only changed by approximately 0.1 $W\,m^{-2}\,K^{-1}$ between 1993–2010 and 2006–2023 (Tables 2–3). The changes in feedbacks are driven by clouds over the North and East Pacific and the loss of Antarctic sea ice (Figs. 3, 6), and the 2001–2023 differential feedback is now approaching models' long-term feedback from CO_2 forcing. If this pattern persists without compensating changes in the efficiency of ocean heat uptake (e.g., Gregory et al. 2015, 2020, 2024; Armour et al. 2024; Newsom et al. 2020), the rate of global warming is expected to increase. We also investigate a key model-observation discrepancy in shortwave clear-sky trends over 2001–2023 (30–90°S): AMIP's sea ice produces a trend of opposite sign compared to CERES, whereas trends using Cooper et al. (2025)'s sea ice align with CERES (Fig. 7).

Historical pattern effect. Over the full record (1850–2023), we estimate a historical pattern effect (defined as the difference between the net feedback for 2xCO_2 versus the observed historical period) of 0.62 $\mathrm{W\,m^{-2}\,K^{-1}}$ (−0.05 to 1.03, 5–95%) based on finite differences between the 2006–2023 mean relative to 1850–1900; we find a similar result of 0.59 $\mathrm{W\,m^{-2}\,K^{-1}}$ (0.09 to 1.05, 5–95%) for the differential feedback from OLS regression over 1871–2023. Our central estimates are slightly larger than Sherwood et al. (2020)'s, and our 90% range is similar. Including the additional years from 2011–2023 causes a small decrease of 0.1 $\mathrm{W\,m^{-2}\,K^{-1}}$ in estimates of the historical pattern effect over the full record when using Cooper et al. (2025)'s SST/SIC, and these additional years have little influence on the observation-based feedback over the full record (Fig. 3d–f). SST/SIC uncertainty tends to be a larger source of spread in the historical pattern effect than inter-model differences across 15 AGCMs, especially if structural inter-dataset differences are included in the SST/SIC spread (Figs. 9, B3).

Climate sensitivity. Revisions to the historical pattern effect, surface temperature, and Earth's energy imbalance through 2023 each shift ECS estimates marginally higher (Fig. 10). However, the largest revision comes from aerosol forcing: using IPCC AR6's extended forcing (Forster et al. 2025) reduces the maximum likelihood from historical evidence to 3.4 K. Combining our revised historical evidence with recent studies of paleoclimate pattern effects (Cooper et al. 2024, 2026) yields a median ECS estimate of 2.8 K (2.1–3.9 K, 5–95%).

Limitations and outlook. Our ECS estimates do not yet incorporate potential revisions to the statistical methods, paleoclimate forcings, or process evidence (e.g., Marvel and Webb 2025; Sokol et al. 2024; Raghuraman et al. 2024a; McKim et al. 2024; Ceppi et al. 2024; Zelinka et al. 2026), which could change the combined estimates from this study. There are recent bias corrections for SST data (e.g., Chan et al. 2025), which could be implemented in Cooper et al. (2025)'s data-assimilation framework, and reducing SST/SIC uncertainty through improved historical reconstructions could further clarify the evolution of historical feedbacks. Compared to previous studies, we find that the strongly stabilizing feedback over c. 1975–2014 is even more unusual relative to feedbacks before/after that period, which motivates further investigation of 1975–2014 and of the recent trend toward less-stabilizing feedbacks over 2001–2023. To compare modeled trends in TOA radiation with CERES observations (e.g., Schmidt et al. 2023), additional AGCM simulations with time-varying historical forcings are needed. We also recommend replacing or revising AMIP's sea ice in any new historical AGCM simulations (e.g., Ceppi et al. 2026). Finally, a quantitative synthesis of recent constraints on aerosol forcing is warranted given its impact on ECS estimates from the historical record.

Acknowledgments. We acknowledge funding from: a Houghton Postdoctoral Fellowship (V.T.C.); National Science Foundation (NSF) awards OPP-2213988 (V.T.C.), AGS-1752796 (V.T.C. and K.C.A.), AGS-2203543 (V.T.C. and K.C.A.); and a Calvin Professorship in Oceanography (K.C.A.). We acknowledge computing support from Casper (https://ncar.pub/casper) and Derecho (https://doi.org/10.5065/qx9a-pg09) provided by the NSF National Center for Atmospheric Research (NCAR). T.A. was supported by the Met Office Hadley Centre Climate Programme funded by DSIT. We thank C. Proistosescu, G. Hakim, S. P. Raghuraman, N. Lewis, and A. Modak for helpful discussions. The authors declare no conflicts of interest.

Data availability statement. AGCM results and SST/SIC boundary conditions from this study will be available in a Zenodo repository upon acceptance. Supporting data are available as follows: Cooper et al. (2025)'s ensemble reanalysis, https://doi.org/10.5281/zenodo.17714760; Extended IPCC AR6 Indicators, Smith et al. (2025) and https://github.com/ClimateIndicator/forcing-timeseries/releases/tag/v6.3.1; CERES EBAF Ed4.2.1, https://ceres.larc.nasa.gov/data/; DCENT-I, Chan et al. (2026); CAM6 AMIP simulations using ERSST, Philips and Simpson (2026); previously published AGCM *pi-Forcing* results, Andrews et al. (2022) and Modak and Mauritsen (2023). SST/SIC is available for: PCMDI-AMIP-1-1-9 at https://aims2.llnl.gov/; HadISST1 at https://www.metoffice.gov.uk/hadobs/hadisst/data/download.html; ERSSTv5 at https://www.ncei.noaa.gov/products/extended-reconstructed-sst.

APPENDIX A

ΔN vs. ΔT Gregory plots of 5-year block means

This appendix addresses two statistical points. First, we illustrate the impact of 5-year block averaging. Second, we show why differential λ over 1871–2023 is not strongly influenced by the anomalous λ over c. 1975–2014.

5-year block averaging reduces the imprint of natural variability (i.e., noise) on estimates of λ (Fig. A1) and is simple to implement. Sophisticated methods exist that attempt to remove ENSO and other modes of variability, but accurately removing variability in both N and T is difficult due to phase-lags and because ENSO itself varies, and these methods could accidentally remove part of the forced response. Over most of the record, correlated errors in N and T appear to bias λ toward a more-negative slope (Fig. A1). Note that the unusual 2023 anomalies in N and T contribute to a weakly negative feedback (slope closer to zero) when regressing annual means over recent decades. A simple way to reduce the influence of variability is by block averaging or smoothing. The trade-off is a reduction in the effective degrees of freedom, which affects estimates of the error.

Figure A2 shows Gregory plots of CAM6's ensemble mean from *C25-piForcing* simulations, including slopes estimated for different periods. Panel **a** illustrates why the strongly negative feedback over 1974–2013 has little influence on the differential λ over 1874–2023 and why adding the additional 10 years of data (2014–2023) also has little influence. In other words, the 1874–2013 differential λ is similar to λ over 1874–2023. Panel **b** similarly shows that the effective λ is not strongly affected by changing the end period from 1993–2010 to 2006–2023. Results are similar in the other AGCMs.

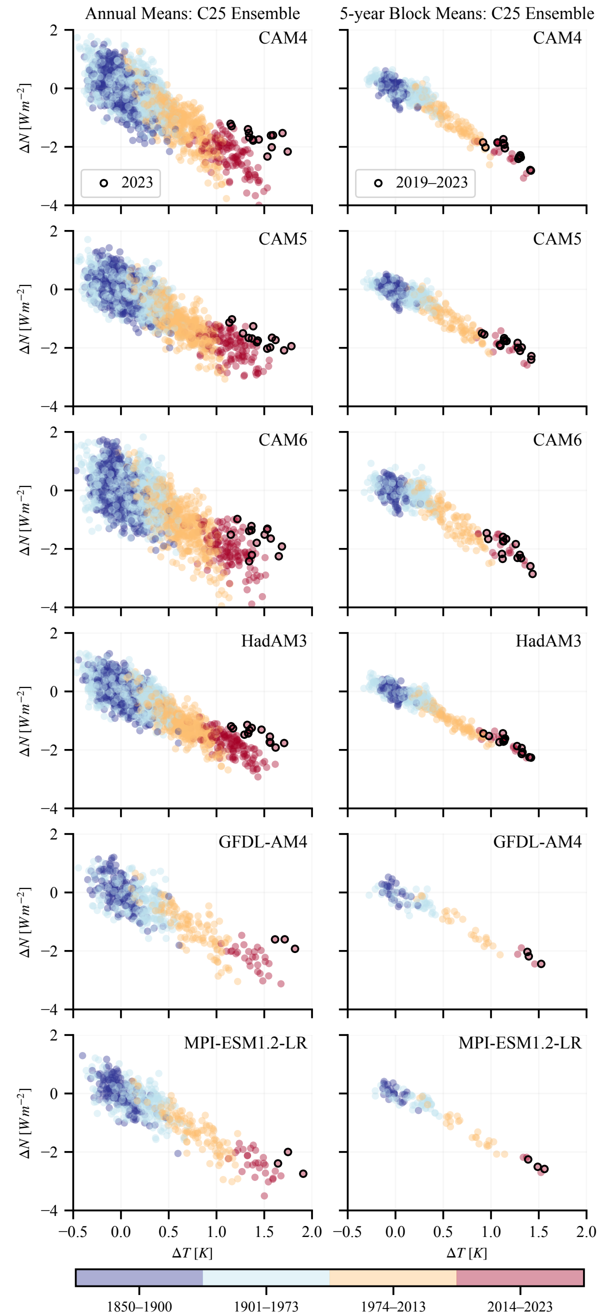

FIG. A1. **Comparison of annual versus 5-year block means in Gregory plots of ΔN and ΔT over 1850–2023.** Results show all ensemble members from *C25-piForcing* simulations as anomalies from their 1850–1900 means. Left column shows annual means and right column shows 5-year block means from the same simulations. Coloring of the scatter plot is a visual aid to see how regression-based feedbacks over short periods would be biased by correlated errors in N and T (i.e., the noise has a steep negative slope around the linear fit). The final year (2023) and 5-year block (2019–2023) are marked on all plots to illustrate the unusual N and T anomalies in 2023.

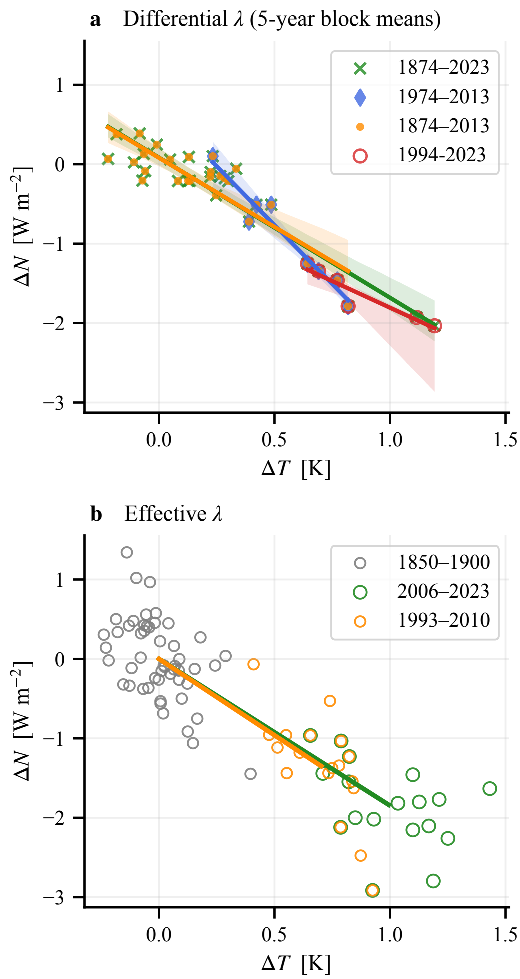

FIG. A2. **Gregory plots of ΔN vs. ΔT from *C25-piForcing* simulations in CAM6.** For illustrative purposes, each data point represents the mean across CAM6's 14 ensemble members from *C25-piForcing* as anomalies w.r.t. 1850–1900. **(a)** Differential λ from OLS regressions of 5-year block means for four time periods; endpoints are selected to maintain consistent 5-year blocks; shading represents the 95% range of regression errors based on bootstrap resampling. **(b)** Effective λ for two periods based on mean anomalies w.r.t. 1850–1900; scattered points represent annual means in each period; the lines show effective λ as the slope starting from the origin and ending at the mean anomaly over 1993–2010 or 2006–2023.

APPENDIX B

Additional results for effective λ from finite differences

Figures B1, B2, and B3 are analogous to Figs. 4, 8, and 9, respectively, but show results for the effective λ from finite differences rather than the differential λ.

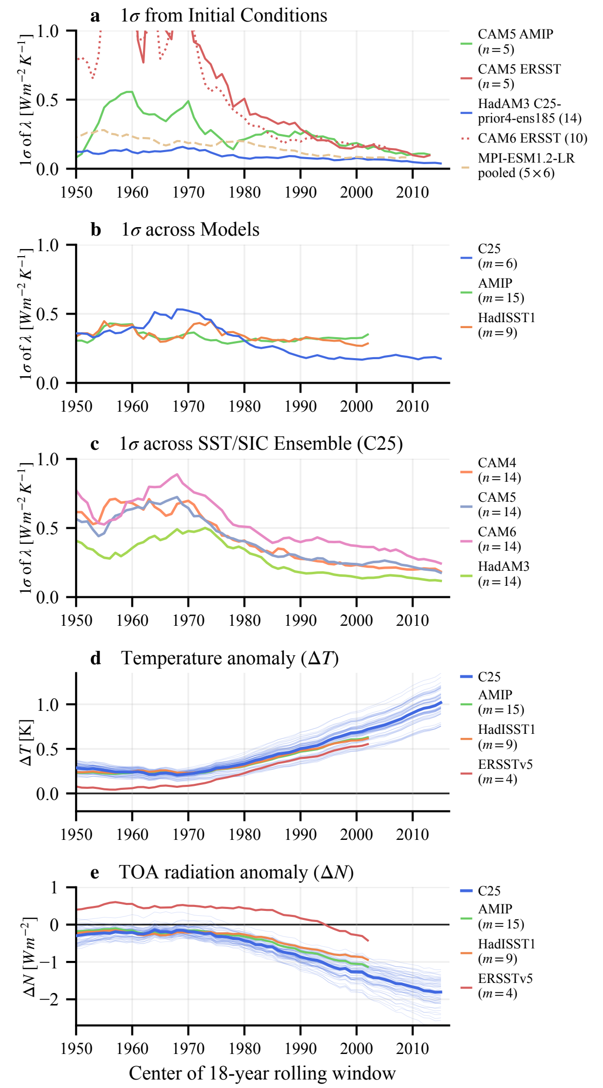

FIG. B1. **Sources of spread in effective feedbacks (λ) over 18-yr windows.** **(a)** Sample standard deviation (1σ) of λ across initial condition (IC) ensembles in various AGCMs. Note CAM6 ERSST is from a simulation with time-varying historical rather than constant preindustrial forcings, and MPI-ESM1.2-LR is based on pooled variance from Modak and Mauritsen (2023) simulations, excluding ERSST because it is an outlier before c. 1990. **(b)** 1σ across models using a common SST/SIC dataset, after taking the mean over any IC ensemble members. C25 is based on pooled variance from the three SST/SIC boundary conditions used in all six AGCMs. **(c)** 1σ across C25's SST/SIC boundary conditions for the four AGCMs that used 14 ensemble members. **(d–e)** Multi-model mean of anomalies in N and T over 18-year windows, with respect to the pre-1900 mean; C25 ensemble members from all AGCMs are shown as thin lines.

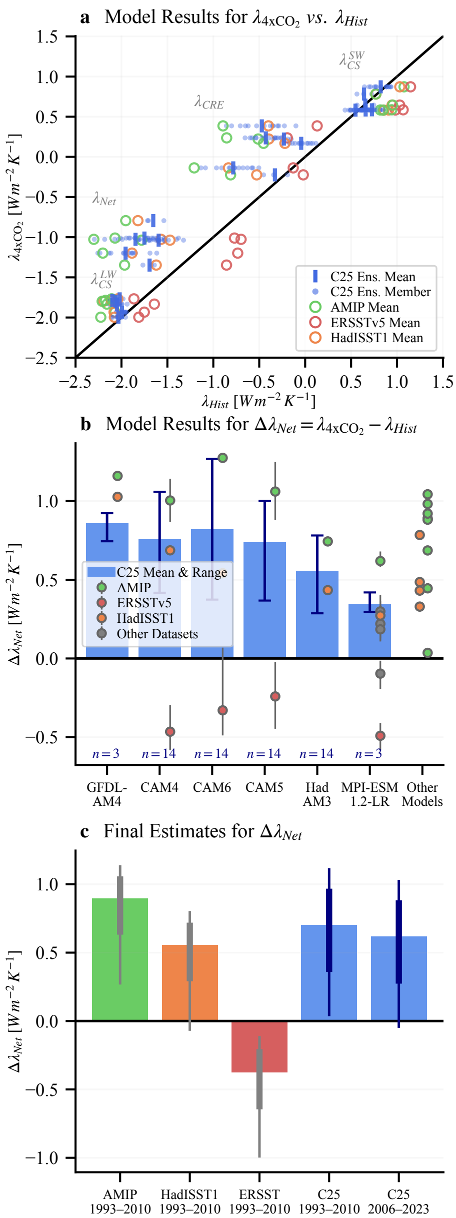

FIG. B2. **Effective feedbacks (λ_{Hist}) and pattern effects ($\Delta\lambda$).** **(a)** λ_{4xCO_2} vs. λ_{Hist} from *C25-piForcing* simulations in six AGCMs. AMIP/ERSST/HadISST1 are based on mean anomalies over 1993–2010 w.r.t. 1871–1900 (CAM6 ERSST is w.r.t. 1880–1900), whereas C25 is based on 2006–2023 w.r.t. 1850–1900; results are similar if C25 uses 1871–1900. **(b)** Net $\Delta\lambda$ using results in panel **a**. The number of C25 simulations for each AGCM is shown on the horizontal axis. Gray errors (for AMIP/ERSST/HadISST1/Other) are ranges from initial-condition ensembles. Other Models are listed in Table 1. **(c)** Median $\Delta\lambda$ from the crossed random-effects model; errors denote 66% (thick) and 90% (thin) ranges; C25 ranges include intermodel and SST/SIC spread.

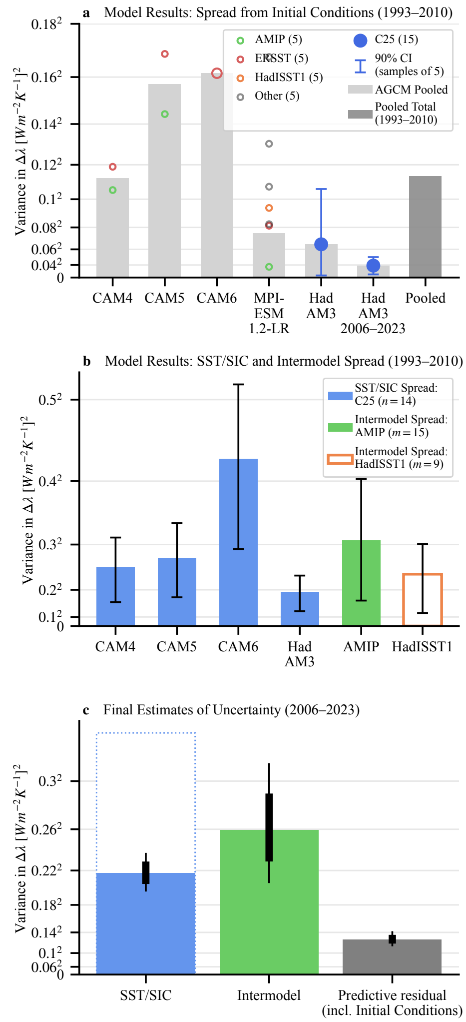

FIG. B3. **Sources of spread in $\Delta\lambda$ for effective λ.** Results for 1993–2010 use mean anomalies w.r.t. 1871–1900 (a common period across simulations); 2006–2023 results are w.r.t. 1850–1900. **(a)** Sample variance from initial conditions (ICs) using various AGCMs and SST/SIC datasets. Bars show pooled variance for 1993–2010, except for HadAM3's 2006–2023 result. Circles correspond to individual IC ensembles. HadAM3 errors are 90% ranges from bootstrap subsampling to 5 members, testing whether its spread differs from other AGCMs. **(b)** Sample variance for 1993–2010 across C25's SST/SIC ensemble in various AGCMs, compared with variance from intermodel spread across AGCMs using AMIP/HadISST1 (Andrews et al. 2022); errors are 90% ranges from bootstrap resampling. **(c)** Sources of spread for 2006–2023 based on the crossed random-effects model. Errors show 66% (thick) and 90% (thin) ranges. SST/SIC and intermodel spreads are structural, whereas the predictive residual is for individual estimates of $\Delta\lambda$, given an AGCM and SST/SIC (largely due to IC noise). SST/SIC bars represent spread across (blue) only the C25 ensemble, which informs our ECS estimates, and (white with blue-dotted outline) combining the C25 ensemble with AMIP, HadISST1, and ERSST.

References

Allan, R. P., C. Liu, N. G. Loeb, M. D. Palmer, M. Roberts, D. Smith, and P. Vidale, 2014: Changes in global net radiative imbalance 1985–2012. *Geophysical Research Letters*, **41 (15)**, 5588–5597, https://doi.org/10.1002/2014GL060962.

Allan, R. P., and C. J. Merchant, 2025: Reconciling Earth's growing energy imbalance with ocean warming. *Environmental Research Letters*, **20 (4)**, 044 002, https://doi.org/10.1088/1748-9326/adb448.

Andrews, T., 2014: Using an AGCM to Diagnose Historical Effective Radiative Forcing and Mechanisms of Recent Decadal Climate Change. *Journal of Climate*, **27 (3)**, 1193–1209, https://doi.org/10.1175/JCLI-D-13-00336.1.

Andrews, T., J. M. Gregory, and M. J. Webb, 2015: The Dependence of Radiative Forcing and Feedback on Evolving Patterns of Surface Temperature Change in Climate Models. *Journal of Climate*, **28 (4)**, 1630–1648, https://doi.org/10.1175/JCLI-D-14-00545.1.

Andrews, T., and M. J. Webb, 2018: The Dependence of Global Cloud and Lapse Rate Feedbacks on the Spatial Structure of Tropical Pacific Warming. *Journal of Climate*, **31 (2)**, 641–654, https://doi.org/10.1175/JCLI-D-17-0087.1.

Andrews, T., and Coauthors, 2018: Accounting for Changing Temperature Patterns Increases Historical Estimates of Climate Sensitivity. *Geophysical Research Letters*, **45 (16)**, 8490–8499, https://doi.org/10.1029/2018GL078887.

Andrews, T., and Coauthors, 2022: On the Effect of Historical SST Patterns on Radiative Feedback. *Journal of Geophysical Research: Atmospheres*, **127 (18)**, https://doi.org/10.1029/2022JD036675.

Armour, K. C., 2017: Energy budget constraints on climate sensitivity in light of inconstant climate feedbacks. *Nature Climate Change*, **7 (5)**, 331–335, https://doi.org/10.1038/nclimate3278.

Armour, K. C., C. M. Bitz, and G. H. Roe, 2013: Time-Varying Climate Sensitivity from Regional Feedbacks. *Journal of Climate*, **26 (13)**, 4518–4534, https://doi.org/10.1175/JCLI-D-12-00544.1.

Armour, K. C., J. Marshall, J. R. Scott, A. Donohoe, and E. R. Newsom, 2016: Southern Ocean warming delayed by circumpolar upwelling and equatorward transport. *Nature Geoscience*, **9 (7)**, 549–554, https://doi.org/10.1038/ngeo2731.

Armour, K. C., and Coauthors, 2024: Sea-surface temperature pattern effects have slowed global warming and biased warming-based constraints on climate sensitivity. *Proceedings of the National Academy of Sciences*, **121 (12)**, e2312093 121, https://doi.org/10.1073/pnas.2312093121.

Bacmeister, J. T., and Coauthors, 2020: CO2 Increase Experiments Using the CESM: Relationship to Climate Sensitivity and Comparison of CESM1 to CESM2. *Journal of Advances in Modeling Earth Systems*, **12 (11)**, https://doi.org/10.1029/2020MS002120.

Bellouin, N., and Coauthors, 2020: Bounding Global Aerosol Radiative Forcing of Climate Change. *Reviews of Geophysics*, **58 (1)**, https://doi.org/10.1029/2019RG000660.

Blanchard-Wrigglesworth, E., R. Bilbao, A. Donohoe, and S. Materia, 2025: Record Warmth of 2023 and 2024 was Highly Predictable and Resulted From ENSO Transition and Northern Hemisphere Absorbed Shortwave Anomalies. *Geophysical Research Letters*, **52 (10)**, e2025GL115 614, https://doi.org/10.1029/2025GL115614.

Bloch-Johnson, J., M. Rugenstein, M. B. Stolpe, T. Rohrschneider, Y. Zheng, and J. M. Gregory, 2021: Climate Sensitivity Increases Under Higher CO2 Levels Due to Feedback Temperature Dependence. *Geophysical Research Letters*, **48 (4)**, e2020GL089 074, https://doi.org/10.1029/2020GL089074.

Capretto, T., C. Piho, R. Kumar, J. Westfall, T. Yarkoni, and O. A. Martin, 2022: Bambi: A Simple Interface for Fitting Bayesian Linear Models in Python. *Journal of Statistical Software*, **103 (15)**, https://doi.org/10.18637/jss.v103.i15.

Ceppi, P., and S. Fueglistaler, 2021: The El Niño–Southern Oscillation Pattern Effect. *Geophysical Research Letters*, **48 (21)**, https://doi.org/10.1029/2021GL095261.

Ceppi, P., and J. M. Gregory, 2017: Relationship of tropospheric stability to climate sensitivity and Earth's observed radiation budget. *Proceedings of the National Academy of Sciences*, **114 (50)**, 13 126–13 131, https://doi.org/10.1073/pnas.1714308114.

Ceppi, P., and J. M. Gregory, 2019: A refined model for the Earth's global energy balance. *Climate Dynamics*, **53 (7-8)**, 4781–4797, https://doi.org/10.1007/s00382-019-04825-x.

Ceppi, P., T. A. Myers, P. Nowack, C. J. Wall, and M. D. Zelinka, 2024: Implications of a Pervasive Climate Model Bias for Low-Cloud Feedback. *Geophysical Research Letters*, **51 (20)**, https://doi.org/10.1029/2024GL110525.

Ceppi, P., and Coauthors, 2026: The Cloud Feedback Model Intercomparison Project (CFMIP) contribution to CMIP7. *EGUsphere*, https://doi.org/10.5194/egusphere-2026-398.

Chan, D., G. Gebbie, and P. Huybers, 2025: Re-Evaluating Historical Sea Surface Temperature Data Sets: Insights From the Diurnal Cycle, Coral Proxy Data, and Radiative Forcing. *Geophysical Research Letters*, **52 (13)**, https://doi.org/10.1029/2025GL116615.

Chan, D., and P. Huybers, 2019: Systematic Differences in Bucket Sea Surface Temperature Measurements among Nations Identified Using a Linear-Mixed-Effect Method. *Journal of Climate*, **32 (9)**, 2569–2589, https://doi.org/10.1175/JCLI-D-18-0562.1.

Chan, D., and P. Huybers, 2021: Correcting Observational Biases in Sea Surface Temperature Observations Removes Anomalous Warmth during World War II. *Journal of Climate*, **34 (11)**, 4585–4602, https://doi.org/10.1175/JCLI-D-20-0907.1.

Chan, D., and Coauthors, 2026: DCENT-I: A Globally Infilled Extension of the Dynamically Consistent ENsemble of Temperature Dataset. *Geoscience Data Journal*, **13 (2)**, 70 054, https://doi.org/10.1002/gdj3.70054.

Cooper, V. T., G. J. Hakim, and K. C. Armour, 2025: Monthly Sea Surface Temperature, Sea Ice, and Sea Level Pressure over 1850–2023 from Coupled Data Assimilation. *Journal of Climate*, **38 (19)**, 5461–5490, https://doi.org/10.1175/JCLI-D-25-0021.1.

Cooper, V. T., and Coauthors, 2024: Last Glacial Maximum pattern effects reduce climate sensitivity estimates. *Science Advances*, **10 (16)**, 9461, https://doi.org/10.1126/sciadv.adk9461.

Cooper, V. T., and Coauthors, 2026: Paleoclimate pattern effects help constrain climate sensitivity and 21st-century warming. *Proceedings of the National Academy of Sciences*, **123 (4)**, https://doi.org/10.1073/pnas.2511370123.

Cowtan, K., and R. G. Way, 2014: Coverage bias in the HadCRUT4 temperature series and its impact on recent temperature trends. *Quarterly*

Journal of the Royal Meteorological Society, **140 (683)**, 1935–1944, https://doi.org/10.1002/qj.2297.

Cowtan, K., and Coauthors, 2015: Robust comparison of climate models with observations using blended land air and ocean sea surface temperatures. *Geophysical Research Letters*, **42 (15)**, 6526–6534, https://doi.org/10.1002/2015GL064888.

Danabasoglu, G., and Coauthors, 2020: The Community Earth System Model Version 2 (CESM2). *Journal of Advances in Modeling Earth Systems*, **12 (2)**, https://doi.org/10.1029/2019MS001916.

Deser, C., A. S. Phillips, and M. A. Alexander, 2010: Twentieth century tropical sea surface temperature trends revisited. *Geophysical Research Letters*, **37 (10)**, https://doi.org/10.1029/2010GL043321.

Dong, Y., K. C. Armour, M. D. Zelinka, C. Proistosescu, D. S. Battisti, C. Zhou, and T. Andrews, 2020: Intermodel Spread in the Pattern Effect and Its Contribution to Climate Sensitivity in CMIP5 and CMIP6 Models. *Journal of Climate*, **33 (18)**, 7755–7775, https://doi.org/10.1175/JCLI-D-19-1011.1.

Dong, Y., C. Proistosescu, K. C. Armour, and D. S. Battisti, 2019: Attributing Historical and Future Evolution of Radiative Feedbacks to Regional Warming Patterns using a Green's Function Approach: The Preeminence of the Western Pacific. *Journal of Climate*, **32 (17)**, 5471–5491, https://doi.org/10.1175/JCLI-D-18-0843.1.

Dong, Y., and Coauthors, 2021: Biased Estimates of Equilibrium Climate Sensitivity and Transient Climate Response Derived From Historical CMIP6 Simulations. *Geophysical Research Letters*, **48 (24)**, https://doi.org/10.1029/2021GL095778.

Duffy, M. L., and Coauthors, 2026: Is the High ECS in CESM2 Degrading Transient Climate Change Projections Over the 21st Century? *Journal of Advances in Modeling Earth Systems*, **18 (1)**, e2025MS004 967, https://doi.org/10.1029/2025MS004967.

Dunne, J. P., and Coauthors, 2020: Comparison of Equilibrium Climate Sensitivity Estimates From Slab Ocean, 150-Year, and Longer Simulations. *Geophysical Research Letters*, **47 (16)**, e2020GL088 852, https://doi.org/10.1029/2020GL088852.

Dunne, J. P., and Coauthors, 2025: An evolving Coupled Model Intercomparison Project phase 7 (CMIP7) and Fast Track in support of future climate assessment. *Geoscientific Model Development*, **18 (19)**, 6671–6700, https://doi.org/10.5194/GMD-18-6671-2025.

Durack, P. J., K. E. Taylor, S. K. Ames, S. Po-Chedley, and C. Mauzey, 2025a: PCMDI AMIP SST and Sea-Ice Boundary Conditions Version 1.1.10. Tech. rep., input4MIPs. https://doi.org/10.25981/ESGF.input4MIPs.CMIP7/2575015.

Durack, P. J., M. D. Zelinka, and K. E. Taylor, 2025b: PCMDI-AMIP-ERSST5-1-0. Tech. rep., input4MIPs. https://doi.org/10.25981/ESGF.input4MIPs.CMIP7Plus/2584105.

Duran, B. M., and Coauthors, 2025: A new method for diagnosing effective radiative forcing from aerosol–cloud interactions in climate models. *Atmospheric Chemistry and Physics*, **25 (4)**, 2123–2146, https://doi.org/10.5194/acp-25-2123-2025.

Dvorak, M., K. C. Armour, R. Feng, V. T. Cooper, J. Zhu, N. Burls, and C. Proistosescu, 2025: Mid-Pliocene Climate Forcing, Sea Surface Temperature Patterns, and Implications for Modern-Day Climate Sensitivity. *Journal of Climate*, **38 (13)**, 3037–3053, https://doi.org/10.1175/JCLI-D-24-0410.1.

Embury, O., and Coauthors, 2024: Satellite-based time-series of sea-surface temperature since 1980 for climate applications. *Scientific Data*, **11 (1)**, 326, https://doi.org/10.1038/s41597-024-03147-w.

Eyring, V., S. Bony, G. A. Meehl, C. A. Senior, B. Stevens, R. J. Stouffer, and K. E. Taylor, 2016: Overview of the Coupled Model Intercomparison Project Phase 6 (CMIP6) experimental design and organization. *Geoscientific Model Development*, **9 (5)**, 1937–1958, https://doi.org/10.5194/gmd-9-1937-2016.

Fan, C., D. Paynter, R. J. Kramer, and P. Lin, 2025: Sensitivity of Earth's Radiation Budget to Lower Boundary Condition Data Sets in Historical Climate Simulations. *Geophysical Research Letters*, **52 (17)**, https://doi.org/10.1029/2025GL115914.

Forster, P., and Coauthors, 2021: The Earth's energy budget, climate feedbacks, and climate sensitivity. *Climate Change 2021: The Physical Science Basis. Contribution of Working Group I to the Sixth Assessment Report of the Intergovernmental Panel on Climate Change*, V. Masson-Delmotte, P. Zhai, A. Pirani, S. Connors, C. Péan, S. Berger, N. Caud, Y. Chen, L. Goldfarb, M. Gomis, M. Huang, K. Leitzell, E. Lonnoy, J. Matthews, T. Maycock, T. Waterfield, O. Yelekçi, R. Yu, and B. Zhou, Eds., Cambridge University Press, Cambridge, UK and New York, NY, chap. 7, https://doi.org/10.1017/9781009157896.009.

Forster, P. M., and Coauthors, 2025: Indicators of Global Climate Change 2024: annual update of key indicators of the state of the climate system and human influence. *Earth System Science Data*, **17 (6)**, 2641–2680, https://doi.org/10.5194/essd-17-2641-2025.

Foster, G., and S. Rahmstorf, 2026: Global Warming Has Accelerated Significantly. *Geophysical Research Letters*, **53 (5)**, e2025GL118 804, https://doi.org/10.1029/2025GL118804.

Fredericks, L., and Coauthors, 2026: Quantifying the Radiative Response to Surface Temperature Variability: A Critical Comparison of Current Methods. *Journal of Climate*, **39 (14)**, 4101–4116, https://doi.org/10.1175/JCLI-D-25-0612.1.

Freeman, E., and Coauthors, 2017: ICOADS Release 3.0: a major update to the historical marine climate record. *International Journal of Climatology*, **37 (5)**, 2211–2232, https://doi.org/10.1002/joc.4775.

Fueglistaler, S., 2019: Observational Evidence for Two Modes of Coupling Between Sea Surface Temperatures, Tropospheric Temperature Profile, and Shortwave Cloud Radiative Effect in the Tropics. *Geophysical Research Letters*, **46 (16)**, 9890–9898, https://doi.org/10.1029/2019GL083990.

Fueglistaler, S., and L. Silvers, 2021: The Peculiar Trajectory of Global Warming. *Journal of Geophysical Research: Atmospheres*, **126 (4)**, 1–15, https://doi.org/10.1029/2020JD033629.

Gebbie, G., and P. Huybers, 2019: The Little Ice Age and 20th-century deep Pacific cooling. *Science*, **363 (6422)**, 70–74, https://doi.org/10.1126/science.aar8413.

Gelman, A., and J. Hill, 2006: *Data Analysis Using Regression and Multilevel/Hierarchical Models*. Cambridge University Press, https://doi.org/10.1017/CBO9780511790942.

Glassmeier, F., F. Hoffmann, J. S. Johnson, T. Yamaguchi, K. S. Carslaw, and G. Feingold, 2021: Aerosol-cloud-climate cooling overestimated by ship-track data. *Science*, **371 (6528)**, 485–489, https://doi.org/10.1126/science.abd3980.

Good, P., T. Andrews, R. Chadwick, J.-L. Dufresne, J. M. Gregory, J. A. Lowe, N. Schaller, and H. Shiogama, 2016: nonlinMIP contribution to CMIP6: model intercomparison project for non-linear mechanisms: physical basis, experimental design and analysis principles (v1.0). *Geoscientific Model Development*, **9 (11)**, 4019–4028, https://doi.org/10.5194/gmd-9-4019-2016.

Gregory, J. M., and T. Andrews, 2016: Variation in climate sensitivity and feedback parameters during the historical period. *Geophysical Research Letters*, **43 (8)**, 3911–3920, https://doi.org/10.1002/2016GL068406.

Gregory, J. M., T. Andrews, P. Ceppi, T. Mauritsen, and M. J. Webb, 2020: How accurately can the climate sensitivity to CO2 be estimated from historical climate change? *Climate Dynamics*, **54 (1-2)**, 129–157, https://doi.org/10.1007/s00382-019-04991-y.

Gregory, J. M., T. Andrews, and P. Good, 2015: The inconstancy of the transient climate response parameter under increasing CO2. *Philosophical Transactions of the Royal Society A: Mathematical, Physical and Engineering Sciences*, **373 (2054)**, 20140 417, https://doi.org/10.1098/rsta.2014.0417.

Gregory, J. M., R. J. Stouffer, S. C. B. Raper, P. A. Stott, and N. A. Rayner, 2002: An Observationally Based Estimate of the Climate Sensitivity. *Journal of Climate*, **15 (22)**, 3117–3121, https://doi.org/10.1175/1520-0442(2002)015⟨3117:AOBEOT⟩2.0.CO;2.

Gregory, J. M., and Coauthors, 2004: A new method for diagnosing radiative forcing and climate sensitivity. *Geophysical Research Letters*, **31 (3)**, L03 205, https://doi.org/10.1029/2003GL018747.

Gregory, J. M., and Coauthors, 2024: A new conceptual model of global ocean heat uptake. *Climate Dynamics*, **62 (3)**, 1669–1713, https://doi.org/10.1007/s00382-023-06989-z.

Günther, M., H. Schmidt, C. Timmreck, and M. Toohey, 2022: Climate Feedback to Stratospheric Aerosol Forcing: The Key Role of the Pattern Effect. *Journal of Climate*, **35 (24)**, 7903–7917, https://doi.org/10.1175/JCLI-D-22-0306.1.

Günther, M., H. Schmidt, C. Timmreck, and M. Toohey, 2024: Why does stratospheric aerosol forcing strongly cool the warm pool? *Atmospheric Chemistry and Physics*, **24 (12)**, 7203–7225, https://doi.org/10.5194/acp-24-7203-2024.

Hartmann, D. L., 2022: The Antarctic ozone hole and the pattern effect on climate sensitivity. *Proceedings of the National Academy of Sciences*, **119 (35)**, https://doi.org/10.1073/pnas.2207889119.

Haugstad, A. D., K. C. Armour, D. S. Battisti, and B. E. J. Rose, 2017: Relative roles of surface temperature and climate forcing patterns in the inconstancy of radiative feedbacks. *Geophysical Research Letters*, **44 (14)**, 7455–7463, https://doi.org/10.1002/2017GL074372.

He, H., B. Soden, and R. J. Kramer, 2025: Improved Estimates of Equilibrium Climate Sensitivity from Non-Equilibrated Climate Simulations. *ESS Open Archive*, https://doi.org/10.22541/essoar.175157564.42459435/v1.

He, J., and B. J. Soden, 2016: Does the Lack of Coupling in SST-Forced Atmosphere-Only Models Limit Their Usefulness for Climate Change Studies? *Journal of Climate*, **29 (12)**, 4317–4325, https://doi.org/10.1175/JCLI-D-14-00597.1.

Held, I. M., and Coauthors, 2019: Structure and Performance of GFDL's CM4.0 Climate Model. *Journal of Advances in Modeling Earth Systems*, **11 (11)**, 3691–3727, https://doi.org/10.1029/2019MS001829.

Hirahara, S., M. Ishii, and Y. Fukuda, 2014: Centennial-Scale Sea Surface Temperature Analysis and Its Uncertainty. *Journal of Climate*, **27 (1)**, 57–75, https://doi.org/10.1175/JCLI-D-12-00837.1.

Hodnebrog, O., and Coauthors, 2024: Recent reductions in aerosol emissions have increased Earth's energy imbalance. *Communications Earth & Environment*, **5 (1)**, 166, https://doi.org/10.1038/s43247-024-01324-8.

Hoffman, M. D., and A. Gelman, 2014: The No-U-Turn Sampler: Adaptively Setting Path Lengths in Hamiltonian Monte Carlo. *Journal of Machine Learning Research*, **15**, 1593–1623.

Huang, B., and Coauthors, 2017: Extended Reconstructed Sea Surface Temperature, Version 5 (ERSSTv5): Upgrades, Validations, and Intercomparisons. *Journal of Climate*, **30 (20)**, 8179–8205, https://doi.org/10.1175/JCLI-D-16-0836.1.

Hurrell, J. W., J. J. Hack, D. Shea, J. M. Caron, and J. Rosinski, 2008: A New Sea Surface Temperature and Sea Ice Boundary Dataset for the Community Atmosphere Model. *Journal of Climate*, **21 (19)**, 5145–5153, https://doi.org/10.1175/2008JCLI2292.1.

Hurrell, J. W., and K. E. Trenberth, 1999: Global Sea Surface Temperature Analyses: Multiple Problems and Their Implications for Climate Analysis, Modeling, and Reanalysis. *Bulletin of the American Meteorological Society*, **80 (12)**, 2661–2678, https://doi.org/10.1175/1520-0477(1999)080⟨2661:GSSTAM⟩2.0.CO;2.

Huusko, L., A. Modak, and T. Mauritsen, 2022: Stronger Response to the Aerosol Indirect Effect Due To Cooling in Remote Regions. *Geophysical Research Letters*, **49 (21)**, https://doi.org/10.1029/2022GL101184.

Hwang, Y.-T., S.-P. Xie, P.-J. Chen, H.-Y. Tseng, C. Deser, K. Mcmonigal, and M. J. Mcphaden, 2024: Contribution of anthropogenic aerosols to persistent La Niña-like conditions in the early 21st century. *Proceedings of the National Academy of Sciences*, **121 (5)**, 2315124 121, https://doi.org/10.1073/PNAS.2315124121.

Kang, S. M., and S. P. Xie, 2014: Dependence of Climate Response on Meridional Structure of External Thermal Forcing. *Journal of Climate*, **27 (14)**, 5593–5600, https://doi.org/10.1175/JCLI-D-13-00622.1.

Kang, S. M., Y. Yu, C. Deser, X. Zhang, I.-S. Kang, S.-S. Lee, K. B. Rodgers, and P. Ceppi, 2023: Global impacts of recent Southern Ocean cooling. *Proceedings of the National Academy of Sciences*, **120 (30)**, https://doi.org/10.1073/pnas.2300881120.

Kawaguchi, K., and P. Ceppi, 2025: Responses to Lower-Tropospheric Stability Dominate Intermodel Differences in the Historical Pattern Effect. *Geophysical Research Letters*, **52 (17)**, https://doi.org/10.1029/2025GL117015.

Kennedy, J. J., N. A. Rayner, C. P. Atkinson, and R. E. Killick, 2019: An Ensemble Data Set of Sea Surface Temperature Change From 1850: The Met Office Hadley Centre HadSST.4.0.0.0 Data Set. *Journal of Geophysical Research: Atmospheres*, **124 (14)**, 7719–7763, https://doi.org/10.1029/2018JD029867.

Klein, S. A., and D. L. Hartmann, 1993: The Seasonal Cycle of Low Stratiform Clouds. *Journal of Climate*, **6 (8)**, 1587–1606, https://doi.org/10.1175/1520-0442(1993)006⟨1587:TSCOLS⟩2.0.CO;2.

Kramer, R. J., H. He, B. J. Soden, L. Oreopoulos, G. Myhre, P. M. Forster, and C. J. Smith, 2021: Observational Evidence of Increasing Global Radiative Forcing. *Geophysical Research Letters*, **48 (7)**, e2020GL091 585, https://doi.org/10.1029/2020GL091585.

Lewis, N., 2023: Objectively combining climate sensitivity evidence. *Climate Dynamics*, **60 (9-10)**, 3139–3165, https://doi.org/10.1007/s00382-022-06468-x.

Lewis, N., and J. A. Curry, 2015: The implications for climate sensitivity of AR5 forcing and heat uptake estimates. *Climate Dynamics*, **45 (3-4)**, 1009–1023, https://doi.org/10.1007/s00382-014-2342-y.

Lewis, N., and T. Mauritsen, 2021: Negligible Unforced Historical Pattern Effect on Climate Feedback Strength Found in HadISST-Based AMIP Simulations. *Journal of Climate*, **34 (1)**, 39–55, https://doi.org/10.1175/JCLI-D-19-0941.1.

Lin, Y.-J., G. V. Cesana, C. Proistosescu, M. D. Zelinka, and K. C. Armour, 2025: The Relative Importance of Forced and Unforced Temperature Patterns in Driving the Time Variation of Low-Cloud Feedback. *Journal of Climate*, **38 (2)**, 513–529, https://doi.org/10.1175/JCLI-D-24-0014.1.

Loeb, N. G., S.-H. Ham, R. P. Allan, T. J. Thorsen, B. Meyssignac, S. Kato, G. C. Johnson, and J. M. Lyman, 2024: Observational Assessment of Changes in Earth's Energy Imbalance Since 2000. *Surveys in Geophysics*, **45 (6)**, 1757–1783, https://doi.org/10.1007/s10712-024-09838-8.

Loeb, N. G., and Coauthors, 2018: Clouds and the Earth's Radiant Energy System (CERES) Energy Balanced and Filled (EBAF) Top-of-Atmosphere (TOA) Edition-4.0 Data Product. *Journal of Climate*, **31 (2)**, 895–918, https://doi.org/10.1175/JCLI-D-17-0208.1.

Lutsko, N. J., 2018: The Relationship Between Cloud Radiative Effect and Surface Temperature Variability at El Niño-Southern Oscillation Frequencies in CMIP5 Models. *Geophysical Research Letters*, **45 (19)**, https://doi.org/10.1029/2018GL079236.

Mackie, A., M. P. Byrne, E. K. Van de Koot, and A. I. L. Williams, 2025: Circulation and Cloud Responses to Patterned SST Warming. *Geophysical Research Letters*, **52 (8)**, e2024GL112 543, https://doi.org/10.1029/2024GL112543.

Marvel, K., G. A. Schmidt, R. L. Miller, and L. S. Nazarenko, 2016: Implications for climate sensitivity from the response to individual forcings. *Nature Climate Change*, **6 (4)**, 386–389, https://doi.org/10.1038/nclimate2888.

Marvel, K., and M. Webb, 2025: Towards robust community assessments of the Earth's climate sensitivity. *Earth System Dynamics*, **16 (1)**, 317–332, https://doi.org/10.5194/esd-16-317-2025.

Mauritsen, T., and Coauthors, 2019: Developments in the MPI-M Earth System Model version 1.2 (MPI-ESM1.2) and Its Response to Increasing CO2. *Journal of Advances in Modeling Earth Systems*, **11 (4)**, 998–1038, https://doi.org/10.1029/2018MS001400.

Mauritsen, T., and Coauthors, 2025: Earth's Energy Imbalance More Than Doubled in Recent Decades. *AGU Advances*, **6 (3)**, https://doi.org/10.1029/2024AV001636.

McKim, B., S. Bony, and J.-L. Dufresne, 2024: Weak anvil cloud area feedback suggested by physical and observational constraints. *Nature Geoscience*, **17 (5)**, 392–397, https://doi.org/10.1038/s41561-024-01414-4.

Meier, W. N., F. Fetterer, A. K. Windnagel, and J. S. Stewart, 2021: NOAA/NSIDC Climate Data Record of Passive Microwave Sea Ice Concentration, Version 4. Tech. rep., NSIDC: National Snow and Ice Data Center, Boulder, Colorado USA. https://doi.org/10.7265/efmz-2t65.

Menemenlis, S., G. A. Vecchi, W. Yang, S. Fueglistaler, and S. P. Raghuraman, 2025: Consequential differences in satellite-era sea surface temperature trends across datasets. *Nature Climate Change*, **15 (8)**, 897–903, https://doi.org/10.1038/s41558-025-02362-6.

Michibata, T., C. J. Wall, N. Hirota, B. M. Duran, and T. Nozawa, 2025: Recent Advances in the Observation and Modeling of Aerosol-Cloud Interactions, Cloud Feedbacks, and Earth's Energy Imbalance: A Review. *Current Pollution Reports*, **11 (1)**, 50, https://doi.org/10.1007/s40726-025-00382-6.

Mitevski, I., Y. Dong, L. M. Polvani, M. Rugenstein, and C. Orbe, 2023: Non-Monotonic Feedback Dependence Under Abrupt CO2 Forcing Due To a North Atlantic Pattern Effect. *Geophysical Research Letters*, **50 (14)**, https://doi.org/10.1029/2023GL103617.

Miyamoto, A., S.-P. Xie, and C. Deser, 2026: Unforced Interannual-to-Decadal Variability of Global Radiation Imbalance: Role of Low Clouds. *Journal of Climate*, **39 (10)**, 2751–2765, https://doi.org/10.1175/JCLI-D-25-0320.1.

Modak, A., and T. Mauritsen, 2023: Better-constrained climate sensitivity when accounting for dataset dependency on pattern effect estimates. *Atmospheric Chemistry and Physics*, **23 (13)**, 7535–7549, https://doi.org/10.5194/acp-23-7535-2023.

Neale, R. B., J. Richter, S. Park, P. H. Lauritzen, S. J. Vavrus, P. J. Rasch, and M. Zhang, 2013: The Mean Climate of the Community Atmosphere Model (CAM4) in Forced SST and Fully Coupled Experiments. *Journal of Climate*, **26 (14)**, 5150–5168, https://doi.org/10.1175/JCLI-D-12-00236.1.

Neale, R. B., and Coauthors, 2012: Description of the NCAR Community Atmosphere Model (CAM 5.0) (NCAR/TN-486+STR). Tech. rep., NCAR. https://doi.org/10.5065/wgtk-4g06.

Newsom, E., L. Zanna, S. Khatiwala, and J. M. Gregory, 2020: The Influence of Warming Patterns on Passive Ocean Heat Uptake. *Geophysical Research Letters*, **47 (18)**, https://doi.org/10.1029/2020GL088429.

Olonscheck, D., and M. Rugenstein, 2024: Coupled Climate Models Systematically Underestimate Radiation Response to Surface Warming. *Geophysical Research Letters*, **51 (6)**, https://doi.org/10.1029/2023GL106909.

Osborn, T. J., P. D. Jones, D. H. Lister, C. P. Morice, I. R. Simpson, J. P. Winn, E. Hogan, and I. C. Harris, 2021: Land Surface Air Temperature Variations Across the Globe Updated to 2019: The CRUTEM5 Data Set. *Journal of Geophysical Research: Atmospheres*, **126 (2)**, https://doi.org/10.1029/2019JD032352.

Otto, A., and Coauthors, 2013: Energy budget constraints on climate response. *Nature Geoscience*, **6 (6)**, 415–416, https://doi.org/10.1038/ngeo1836.

Park, C., B. J. Soden, R. J. Kramer, T. S. L'Ecuyer, and H. He, 2025: Observational constraints suggest a smaller effective radiative forcing from aerosol–cloud interactions. *Atmospheric Chemistry and Physics*, **25 (13)**, 7299–7313, https://doi.org/10.5194/acp-25-7299-2025.

Paynter, D., T. L. Frölicher, L. W. Horowitz, and L. G. Silvers, 2018: Equilibrium Climate Sensitivity Obtained From Multimillennial Runs of Two GFDL Climate Models. *Journal of Geophysical Research: Atmospheres*, **123 (4)**, 1921–1941, https://doi.org/10.1002/2017JD027885.

Penland, C., and P. D. Sardeshmukh, 1995: The Optimal Growth of Tropical Sea Surface Temperature Anomalies. *Journal of Climate*, **8 (8)**, 1999–2024, https://doi.org/10.1175/1520-0442(1995)008⟨1999:TOGOTS⟩2.0.CO;2.

Persad, G. G., and K. Caldeira, 2018: Divergent global-scale temperature effects from identical aerosols emitted in different regions. *Nature Communications*, **9 (1)**, 3289, https://doi.org/10.1038/s41467-018-05838-6.

Philips, A., and I. Simpson, 2026: CAM6 Prescribed SST AMIP Ensembles. Tech. rep., NSF National Center for Atmospheric Research. https://doi.org/10.26024/800d-nj44.

Pincus, R., P. M. Forster, and B. Stevens, 2016: The Radiative Forcing Model Intercomparison Project (RFMIP): experimental protocol for CMIP6. *Geoscientific Model Development*, **9 (9)**, 3447–3460, https://doi.org/10.5194/gmd-9-3447-2016.

Poletti, A. N., D. M. W. Frierson, and K. C. Armour, 2024: Why Do CO2 Quadrupling Simulations Warm More Than Twice as Much as CO2 Doubling Simulations in CMIP6? *Geophysical Research Letters*, **51 (10)**, https://doi.org/10.1029/2023GL107320.

Pope, V. D., M. L. Gallani, P. R. Rowntree, and R. A. Stratton, 2000: The impact of new physical parametrizations in the Hadley Centre climate model: HadAM3. *Climate Dynamics*, **16 (2-3)**, 123–146, https://doi.org/10.1007/s003820050009.

Possner, A., R. Eastman, F. Bender, and F. Glassmeier, 2020: Deconvolution of boundary layer depth and aerosol constraints on cloud water path in subtropical stratocumulus decks. *Atmospheric Chemistry and Physics*, **20 (6)**, 3609–3621, https://doi.org/10.5194/acp-20-3609-2020.

Proistosescu, C., and P. J. Huybers, 2017: Slow climate mode reconciles historical and model-based estimates of climate sensitivity. *Science Advances*, **3 (7)**, https://doi.org/10.1126/sciadv.1602821.

Proistosescu, C., P. Paul, N. J. Lutsko, A. I. L. Williams, and M. F. Stuecker, 2026: The forgotten role of wave dynamics in modulating the low cloud response to warm pool warming. *arXiv*, https://doi.org/10.48550/arXiv.2603.24488.

Raghuraman, S. P., B. Medeiros, and A. Gettelman, 2024a: Observational Quantification of Tropical High Cloud Changes and Feedbacks. *Journal of Geophysical Research: Atmospheres*, **129 (7)**, https://doi.org/10.1029/2023JD039364.

Raghuraman, S. P., D. Paynter, and V. Ramaswamy, 2021: Anthropogenic forcing and response yield observed positive trend in Earth's energy imbalance. *Nature Communications*, **12 (1)**, 4577, https://doi.org/10.1038/s41467-021-24544-4.

Raghuraman, S. P., B. Soden, A. Clement, G. Vecchi, S. Menemenlis, and W. Yang, 2024b: The 2023 global warming spike was driven by the El Niño–Southern Oscillation. *Atmospheric Chemistry and Physics*, **24 (19)**, 11 275–11 283, https://doi.org/10.5194/acp-24-11275-2024.

Rayner, N. A., D. E. Parker, E. B. Horton, C. K. Folland, L. V. Alexander, D. P. Rowell, E. C. Kent, and A. Kaplan, 2003: Global analyses of sea surface temperature, sea ice, and night marine air temperature since the late nineteenth century. *Journal of Geophysical Research: Atmospheres*, **108 (D14)**, 4407, https://doi.org/10.1029/2002JD002670.

Reynolds, R. W., N. A. Rayner, T. M. Smith, D. C. Stokes, and W. Wang, 2002: An Improved In Situ and Satellite SST Analysis for Climate. *Journal of Climate*, **15 (13)**, 1609–1625, https://doi.org/10.1175/1520-0442(2002)015⟨1609:AIISAS⟩2.0.CO;2.

Richardson, M., K. Cowtan, E. Hawkins, and M. B. Stolpe, 2016: Reconciled climate response estimates from climate models and the energy budget of Earth. *Nature Climate Change*, **6 (10)**, 931–935, https://doi.org/10.1038/nclimate3066.

Richardson, M. T., 2022: Prospects for Detecting Accelerated Global Warming. *Geophysical Research Letters*, **49 (2)**, e2021GL095 782, https://doi.org/10.1029/2021GL095782.

Roach, L. A., and L. M. Polvani, 2026: Persistent Antarctic Sea Ice Biases in CMIP6 Models in spite of the Recent Decadelong Sharp Decline. *Journal of Climate*, **39 (7)**, 1669–1679, https://doi.org/10.1175/JCLI-D-25-0477.1.

Roi-Cohen, O., G. Hadary, C. J. Wall, P. Ceppi, and G. Dagan, 2026: Systematic Observation-Based Estimate of Effective Radiative Forcing from Aerosol–Cloud Interactions. *EGUsphere*, https://doi.org/10.5194/egusphere-2026-3075.

Rugenstein, M., M. Zelinka, K. Karnauskas, P. Ceppi, and T. Andrews, 2023: Patterns of Surface Warming Matter for Climate Sensitivity. *Eos*, **104**, https://doi.org/10.1029/2023EO230411.

Rugenstein, M., and Coauthors, 2020: Equilibrium Climate Sensitivity Estimated by Equilibrating Climate Models. *Geophysical Research Letters*, **47 (4)**, https://doi.org/10.1029/2019GL083898.

Rugenstein, M. A., and K. C. Armour, 2021: Three Flavors of Radiative Feedbacks and Their Implications for Estimating Equilibrium Climate Sensitivity. *Geophysical Research Letters*, **48 (15)**, https://doi.org/10.1029/2021GL092983.

Rugenstein, M. A. A., J. M. Gregory, N. Schaller, J. Sedláček, and R. Knutti, 2016: Multiannual Ocean–Atmosphere Adjustments to Radiative Forcing. *Journal of Climate*, **29 (15)**, 5643–5659, https://doi.org/10.1175/JCLI-D-16-0312.1.

Salvi, P., P. Ceppi, and J. M. Gregory, 2022: Interpreting Differences in Radiative Feedbacks From Aerosols Versus Greenhouse Gases. *Geophysical Research Letters*, **49 (8)**, https://doi.org/10.1029/2022GL097766.

Salvi, P., J. M. Gregory, and P. Ceppi, 2023: Time-Evolving Radiative Feedbacks in the Historical Period. *Journal of Geophysical Research: Atmospheres*, **128 (20)**, https://doi.org/10.1029/2023JD038984.

Santer, B. D., T. M. L. Wigley, J. S. Boyle, D. J. Gaffen, J. J. Hnilo, D. Nychka, D. E. Parker, and K. E. Taylor, 2000: Statistical significance of trends and trend differences in layer-average atmospheric temperature time series. *Journal of Geophysical Research: Atmospheres*, **105 (D6)**, 7337–7356, https://doi.org/10.1029/1999JD901105.

Schmidt, G. A., and Coauthors, 2023: CERESMIP: a climate modeling protocol to investigate recent trends in the Earth's Energy Imbalance. *Frontiers in Climate*, **5**, https://doi.org/10.3389/fclim.2023.1202161.

Screen, J. A., 2011: Sudden increase in Antarctic sea ice: Fact or artifact? *Geophysical Research Letters*, **38 (13)**, https://doi.org/10.1029/2011GL047553.

Senior, C. A., and J. F. B. Mitchell, 2000: The time-dependence of climate sensitivity. *Geophysical Research Letters*, **27 (17)**, 2685–2688, https://doi.org/10.1029/2000GL011373.

Sherwood, S. C., and Coauthors, 2020: An Assessment of Earth's Climate Sensitivity Using Multiple Lines of Evidence. *Reviews of Geophysics*, **58 (4)**, https://doi.org/10.1029/2019RG000678.

Shindell, D. T., 2014: Inhomogeneous forcing and transient climate sensitivity. *Nature Climate Change*, **4 (4)**, 274–277, https://doi.org/10.1038/nclimate2136.

Smith, C., and Coauthors, 2025: Indicators of Global Climate Change 2024. *Zenodo*, https://doi.org/10.5281/zenodo.15744430.

Sokol, A. B., C. J. Wall, and D. L. Hartmann, 2024: Greater climate sensitivity implied by anvil cloud thinning. *Nature Geoscience*, **17 (5)**, 398–403, https://doi.org/10.1038/s41561-024-01420-6.

Stevens, B., S. C. Sherwood, S. Bony, and M. J. Webb, 2016: Prospects for narrowing bounds on Earth's equilibrium climate sensitivity. *Earth's Future*, **4 (11)**, 512–522, https://doi.org/10.1002/2016EF000376.

Stevens, B., and Coauthors, 2026: Earth's net incoming energy-flux imbalance (and its implications for understanding climate change). *Reports on Earth System Science (2026 Ringberg Workshop, MPI-M)*, https://doi.org/10.17617/2.3711842.

Tam, R. Y. S., T. A. Myers, M. D. Zelinka, C. Proistosescu, Y.-J. Lin, and K. Marvel, 2026: Meteorological drivers of the low-cloud radiative feedback pattern effect and its uncertainty. *Atmospheric Chemistry and Physics*, **26 (6)**, 4289–4311, https://doi.org/10.5194/acp-26-4289-2026.

Titchner, H. A., and N. A. Rayner, 2014: The Met Office Hadley Centre sea ice and sea surface temperature data set, version 2: 1. Sea ice concentrations. *Journal of Geophysical Research: Atmospheres*, **119 (6)**, 2864–2889, https://doi.org/10.1002/2013JD020316.

Tsuchida, K., Y. Kosaka, and S. Minobe, 2026: Multi-year La Niña–El Niño transition influenced Earth's extreme energy uptake in 2022–2023. *Nature Geoscience*, **19 (4)**, 432–438, https://doi.org/10.1038/s41561-026-01921-6.

Tsuchida, K., T. Mochizuki, R. Kawamura, and T. Kawano, 2023: Interdecadal Variations of Radiative Feedbacks Associated With the El Niño and Southern Oscillation (ENSO) in CMIP6 Models. *Geophysical Research Letters*, **50 (23)**, e2023GL106 127, https://doi.org/10.1029/2023GL106127.

Vaccaro, A., J. Emile-Geay, D. Guillot, R. Verna, C. Morice, J. Kennedy, and B. Rajaratnam, 2021: Climate Field Completion via Markov Random Fields: Application to the HadCRUT4.6 Temperature Dataset. *Journal of Climate*, **34 (10)**, 4169–4188, https://doi.org/10.1175/JCLI-D-19-0814.1.

Van Loon, S., M. Rugenstein, and E. A. Barnes, 2025: Observation-based estimate of Earth's effective radiative forcing. *Proceedings of the National Academy of Sciences*, **122 (24)**, e2425445 122, https://doi.org/10.1073/pnas.2425445122.

Van Loon, S., M. Rugenstein, M. D. Zelinka, and T. Andrews, 2026: Recent Weakening of the Global Radiative Feedback. *arXiv*, https://doi.org/10.48550/arXiv.2603.12515.

Wall, C. J., J. R. Norris, A. Possner, D. T. McCoy, I. L. McCoy, and N. J. Lutsko, 2022: Assessing effective radiative forcing from aerosol–cloud interactions over the global ocean. *Proceedings of the National Academy of Sciences*, **119 (46)**, e2210481 119, https://doi.org/10.1073/pnas.2210481119.

Watanabe, M., S. M. Kang, M. Collins, Y.-T. Hwang, S. McGregor, and M. F. Stuecker, 2024: Possible shift in controls of the tropical Pacific surface warming pattern. *Nature*, **630 (8016)**, 315–324, https://doi.org/10.1038/s41586-024-07452-7.

Webb, M. J., and Coauthors, 2017: The Cloud Feedback Model Intercomparison Project (CFMIP) contribution to CMIP6. *Geoscientific Model Development*, **10 (1)**, 359–384, https://doi.org/10.5194/gmd-10-359-2017.

Wilks, D. S., 2019: *Statistical Methods in the Atmospheric Sciences*. Elsevier, https://doi.org/10.1016/C2017-0-03921-6.

Williams, A. I. L., N. Jeevanjee, and J. Bloch-Johnson, 2023: Circus Tents, Convective Thresholds, and the Non-Linear Climate Response to Tropical SSTs. *Geophysical Research Letters*, **50 (6)**, e2022GL101 499, https://doi.org/10.1029/2022GL101499.

Wills, R. C. J., Y. Dong, C. Proistosecu, K. C. Armour, and D. S. Battisti, 2022: Systematic Climate Model Biases in the Large-Scale Patterns of Recent Sea-Surface Temperature and Sea-Level Pressure Change. *Geophysical Research Letters*, **49 (17)**, e2022GL100 011, https://doi.org/10.1029/2022GL100011.

Wood, R., and C. S. Bretherton, 2006: On the Relationship between Stratiform Low Cloud Cover and Lower-Tropospheric Stability. *Journal of Climate*, **19 (24)**, 6425–6432, https://doi.org/10.1175/JCLI3988.1.

Wu, Q., J. M. Gregory, L. Zanna, and S. Khatiwala, 2025: Time-varying global energy budget since 1880 from a reconstruction of ocean warming. *Proceedings of the National Academy of Sciences*, **122 (20)**, https://doi.org/10.1073/pnas.2408839122.

Yang, K., C. Liu, J. Li, N. Cao, R. P. Allan, and M. Mayer, 2025: Update of the radiation fluxes at the top of atmosphere and net surface energy flux: DEEPC v5.1. https://doi.org/10.57760/sciencedb.28002.

Yang, Q., and S. Fueglistaler, 2026: Anomalous energy fluxes and feedback parameter over the course of ENSO events. *Authorea Preprints*, https://doi.org/10.22541/essoar.177171298.84394752/v1.

Yuan, T., H. Song, R. Kramer, L. Oreopoulos, S. P. Raghuraman, R. Wood, and M. Chin, 2026: Aerosol effective radiative forcing increases Earth's energy imbalance in recent decades. *Nature Communications*, **17 (1)**, 6322, https://doi.org/10.1038/s41467-026-72926-3.

Zanna, L., S. Khatiwala, J. M. Gregory, J. Ison, and P. Heimbach, 2019: Global reconstruction of historical ocean heat storage and transport. *Proceedings of the National Academy of Sciences*, **116 (4)**, 1126–1131, https://doi.org/10.1073/pnas.1808838115.

Zehrung, A., A. D. King, Z. Nicholls, M. D. Zelinka, and M. Meinshausen, 2025: Standardising the Gregory method for calculating equilibrium climate sensitivity. *Geosci. Model Dev*, **18**, 9433–9450, https://doi.org/10.5194/gmd-18-9433-2025.

Zelinka, M. D., C. J. Smith, Y. Qin, and K. E. Taylor, 2023: Comparison of methods to estimate aerosol effective radiative forcings in climate models. *Atmospheric Chemistry and Physics*, **23 (15)**, 8879–8898, https://doi.org/10.5194/acp-23-8879-2023.

Zelinka, M. D., and Coauthors, 2026: Recent cloud trends and extremes reaffirm established bounds on cloud feedback and aerosol-cloud interactions. *Communications Earth & Environment*, https://doi.org/10.1038/s43247-026-03461-8.

Zhang, B., M. Zhao, and Z. Tan, 2023: Using a Green's Function Approach to Diagnose the Pattern Effect in GFDL AM4 and CM4. *Journal of Climate*, **36 (4)**, 1105–1124, https://doi.org/10.1175/JCLI-D-22-0024.1.

Zhou, C., M. D. Zelinka, and S. A. Klein, 2016: Impact of decadal cloud variations on the Earth's energy budget. *Nature Geoscience*, **9 (12)**, 871–874, https://doi.org/10.1038/ngeo2828.

Zhou, C., M. D. Zelinka, and S. A. Klein, 2017: Analyzing the dependence of global cloud feedback on the spatial pattern of sea surface temperature change with a Green's function approach. *Journal of Advances in Modeling Earth Systems*, **9 (5)**, 2174–2189, https://doi.org/10.1002/2017MS001096.

Zhu, J., C. J. Poulsen, and B. L. Otto-Bliesner, 2024: Modeling Past Hothouse Climates as a Means for Assessing Earth System Models and Improving the Understanding of Warm Climates. *Annual Review of Earth and Planetary Sciences*, https://doi.org/10.1146/annurev-earth-032320.

Zhu, J., and Coauthors, 2022: LGM Paleoclimate Constraints Inform Cloud Parameterizations and Equilibrium Climate Sensitivity in CESM2. *Journal of Advances in Modeling Earth Systems*, **14 (4)**, e2021MS002 776, https://doi.org/10.1029/2021MS002776.

Supplemental Information for "Historical Pattern Effects and Climate Sensitivity Revisited with Novel Constraints on Past Warming Patterns"

Vincent T. Cooper,[a] Kyle C. Armour,[b,c] Jonathan M. Gregory,[d,e] Timothy Andrews,[e,f] Moritz Günther,[g] Chongxing Fan[h]

[a] *Department of Earth, Atmospheric, and Planetary Sciences, Massachusetts Institute of Technology, Cambridge, MA, USA*

[b] *Department of Atmospheric and Climate Science, University of Washington, Seattle, WA, USA*

[c] *School of Oceanography, University of Washington, Seattle, WA, USA*

[d] *National Centre for Atmospheric Science, University of Reading, UK*

[e] *Met Office Hadley Centre, Exeter, UK*

[f] *School of Earth, Environment and Sustainability, University of Leeds, Leeds, UK*

[g] *Climate Dynamics Department, Max Planck Institute for Meteorology, Hamburg, Germany*

[h] *Atmospheric and Oceanic Sciences Program, Princeton University, Princeton, New Jersey, USA*

Corresponding author: Vincent T. Cooper, vcooper@mit.edu

Supplemental Text S1: Early Twentieth Century Cooling

One recent explanation of the cooling in estimates of global-mean T and SST over c. 1900–1910 focuses on biases in bucket measurements of SST: the core idea in Sippel et al. (2024) is that global-mean T inferred from SST data is colder than global-mean T inferred from land T data, indicating that the SST data has a cold bias from changes in bucket-measurement methods. Chan et al. (2026), shown in Fig. 2a, agrees with the SST-bias interpretation and applies an adjustment that makes 1900–1910 relatively warm (compared to its own mean over 1850–1900 and compared to C25 and IPCC AR6 over 1900–1910).

However, gridded reconstructions that assimilate only proxies show c. 1905–1915 as a slightly colder decade, especially in the southern extratropics (Stiller and Hakim 2026; Meng et al. 2025). A cooling with similar timing appears in nighttime-only marine air temperature (Cornes et al. 2025), and it is stronger in a recent analysis of near-surface air temperature data (which includes both nighttime and bias-adjusted daytime observations over oceans) instead of bucket measurements of SST (Morice et al. 2025). Brönnimann et al. (2024) report that 1908–1911 is a local minimum in global-mean T due to cooling in the Southern Hemisphere, supported by recently digitized ship data over the Southern Ocean (the additional data span 1903–1916). Cooper et al. (2025) find regional SST cooling over the Southern Ocean (50–70°S) over 1900–1910 (and over 1875–1910), but C25's global-mean T c. 1910 is only slightly colder than the 1850–1900 mean (Fig. 2a).

More work is needed to obtain a thorough explanation for the colder temperatures (or lack thereof) at the start of the twentieth century for both SST and near-surface air temperature. Some regional SST cooling could be present alongside some SST biases, or there could be a simultaneous bias in both SST and marine-air temperatures. Importantly, the transient nature of any cooling c. 1910 in C25, whether from bias or not, precludes it from impacting estimates of the $\Delta\lambda$ that we use for ECS constraints (Section 6).

Supplemental Figures

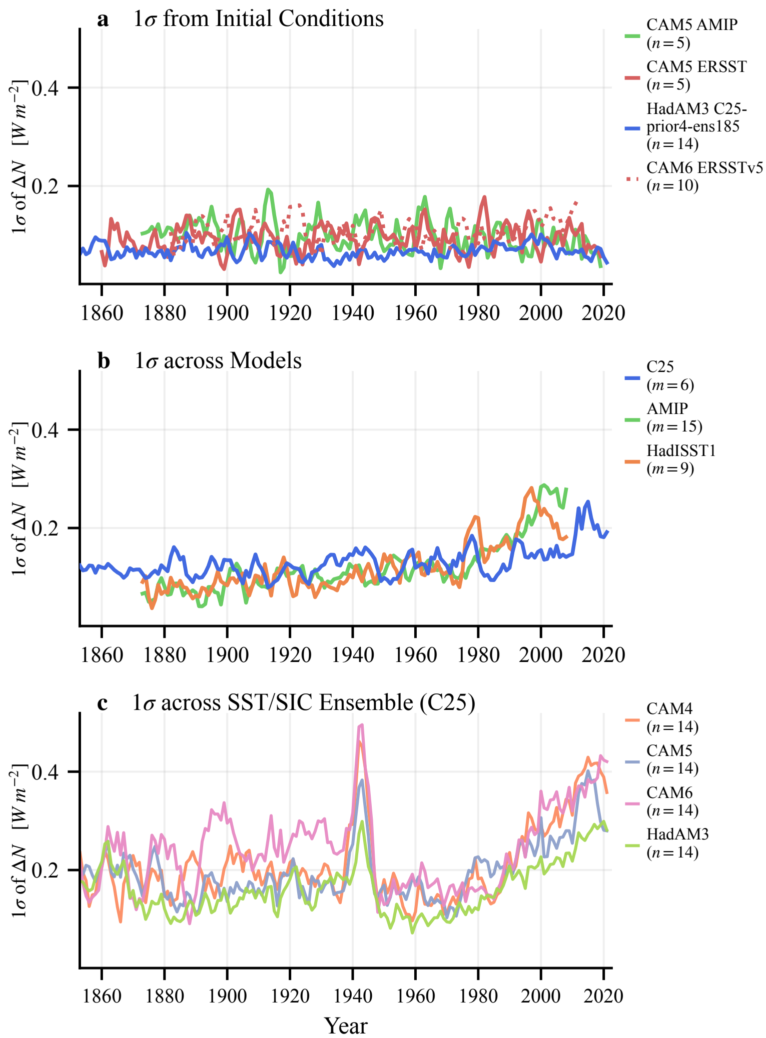

FIG. S1. **Sources of spread in top-of-atmosphere radiation (ΔN).** Anomalies are expressed relative to the 1850–1900 mean, and a 5-year rolling mean is applied to ΔN before calculating the sample standard deviation (1σ). Note that the spread appears largest at the end of the record because anomalies are relative to 1850–1900 means; if we instead subtract the 1980–2010 mean, the spread is large at the beginning and small at the end because the ensemble members have different anomalies (between the early and recent periods). **(a)** is the spread across initial-condition (IC) ensembles, **(b)** is the spread across models with a common SST/SIC boundary condition, and **(c)** is the spread across SST/SIC in the C25 ensemble (Cooper et al. 2025). Note that the spread from ICs cannot be removed from the spread in **b** and **c**, but the IC contribution is not likely to be large because the uncertainties approximately add in quadrature.

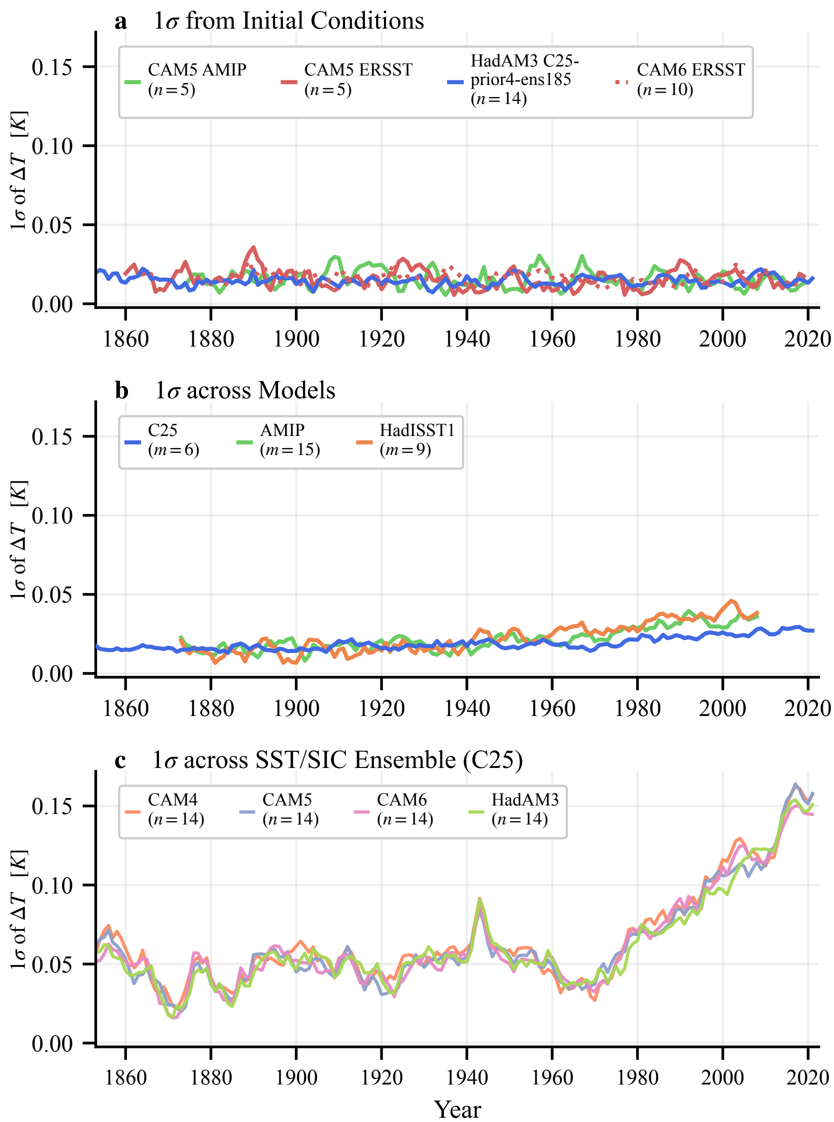

FIG. S2. **Sources of spread in near-surface air temperature (ΔT).** Anomalies are expressed relative to the 1850-1900 mean, and a 5-year rolling mean is applied to ΔT before calculating the sample standard deviation (1σ). Note that the spread appears largest at the end of the record because anomalies are relative to 1850–1900 means; if we instead subtract the 1980–2010 mean, the spread is large at the beginning and small at the end because the ensemble members have different anomalies (between the early and recent periods). **(a)** is the spread across initial-condition (IC) ensembles, **(b)** is the spread across models with a common SST/SIC boundary condition, and **(c)** is the spread across SST/SIC in the C25 ensemble. Note that the spread from ICs cannot be removed from the spread in **b** and **c**, but the IC contribution is not likely to be large because the uncertainties approximately add in quadrature.

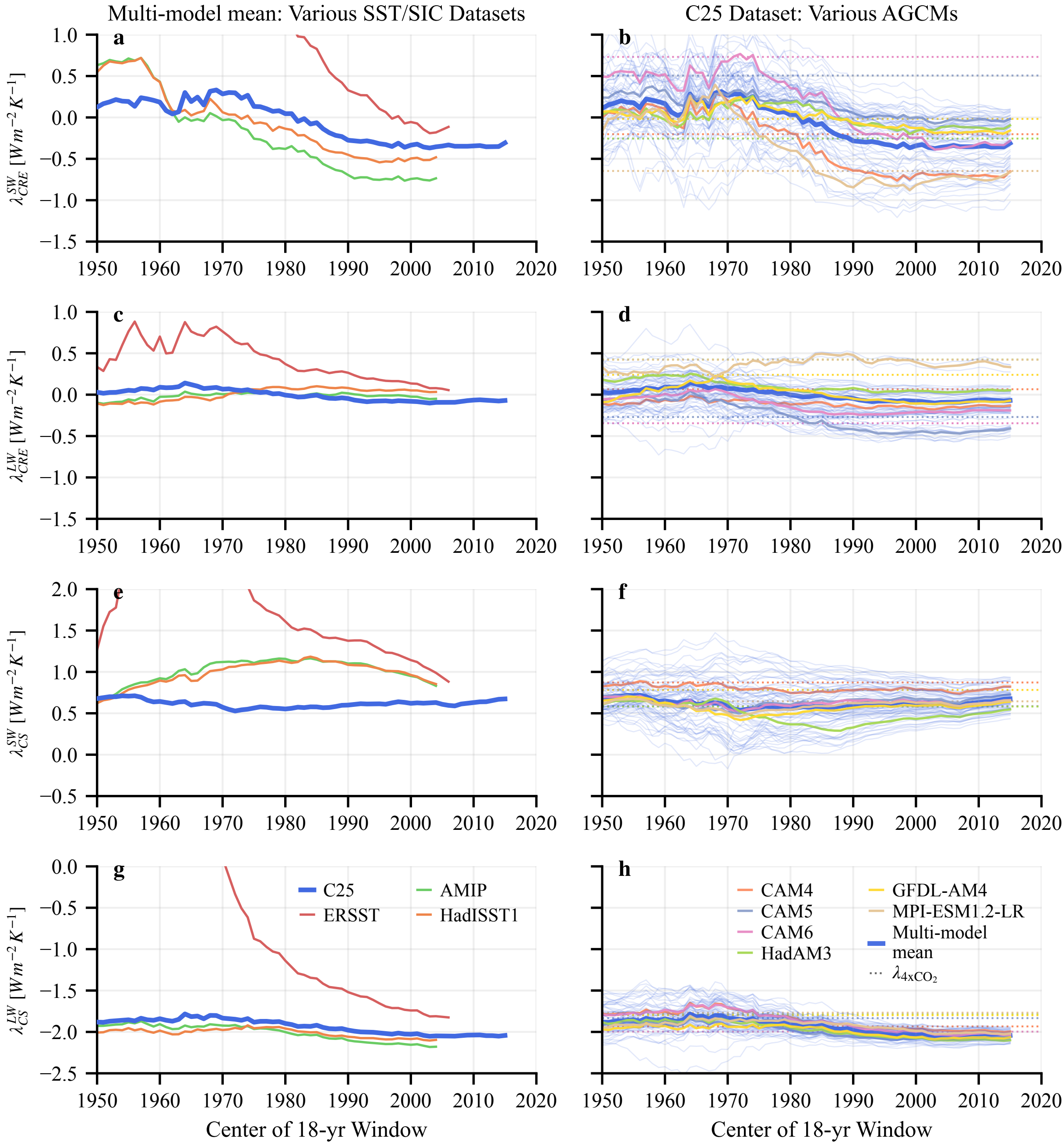

58 Fig. S3. **Components of the effective feedback (λ) from shortwave (SW) and longwave (LW) cloud radiative effects (CRE) and clear-sky (CS) radiation over 18-yr windows from AGCM *piForcing* simulations.** See corresponding figure in the main text (Fig. 5).

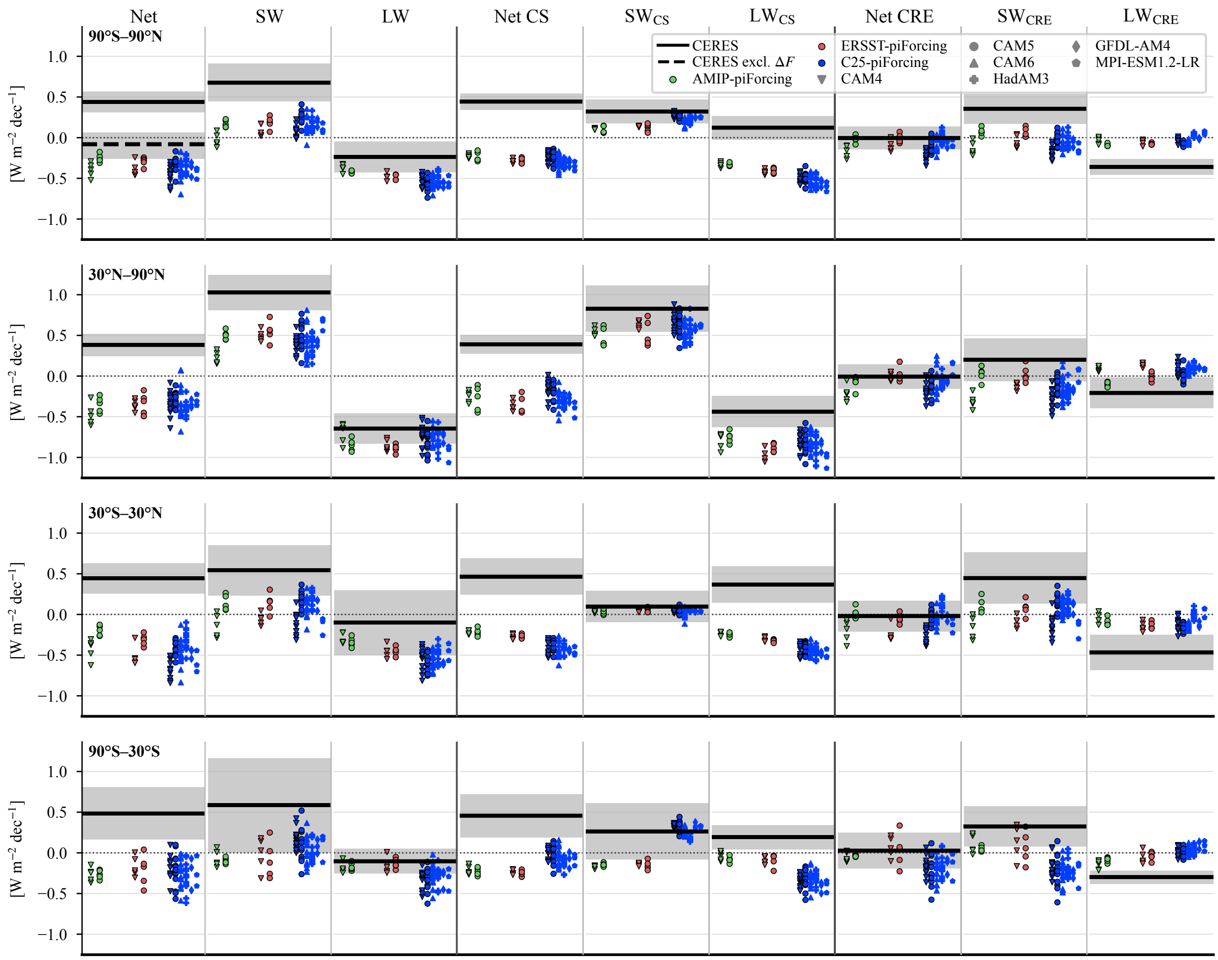

FIG. S4. **Trends in Earth's energy imbalance (EEI) from CERES versus *piForcing* simulations in AGCMs.** These results are not directly comparable because CERES measures EEI including forcing (as $\Delta N = \Delta F + \lambda\Delta T$), whereas *piForcing* simulations estimate only the radiative response to changes in surface temperature (as $\lambda\Delta T$, with $\Delta F = 0$). Dots represent ensemble members from different initial conditions, AGCMs (indicated by symbols), and SST/SIC boundary conditions (indicated by shapes). Note that C25 has different boundary conditions for each ensemble member, whereas AMIP and ERSST are initial-condition ensembles. In the upper left (global-mean net radiation), we subtract Forster et al. (2025)'s ΔF trend from the CERES ΔN trend to provide an approximate direct comparison with AGCMs. Error bars on CERES only represent regression uncertainty (90% range) and are estimated using the effective degrees of freedom from lag-1 autocorrelation of residuals. Note there may be errors and/or drifts in CERES SW/LW CRE (Park and Soden 2026).

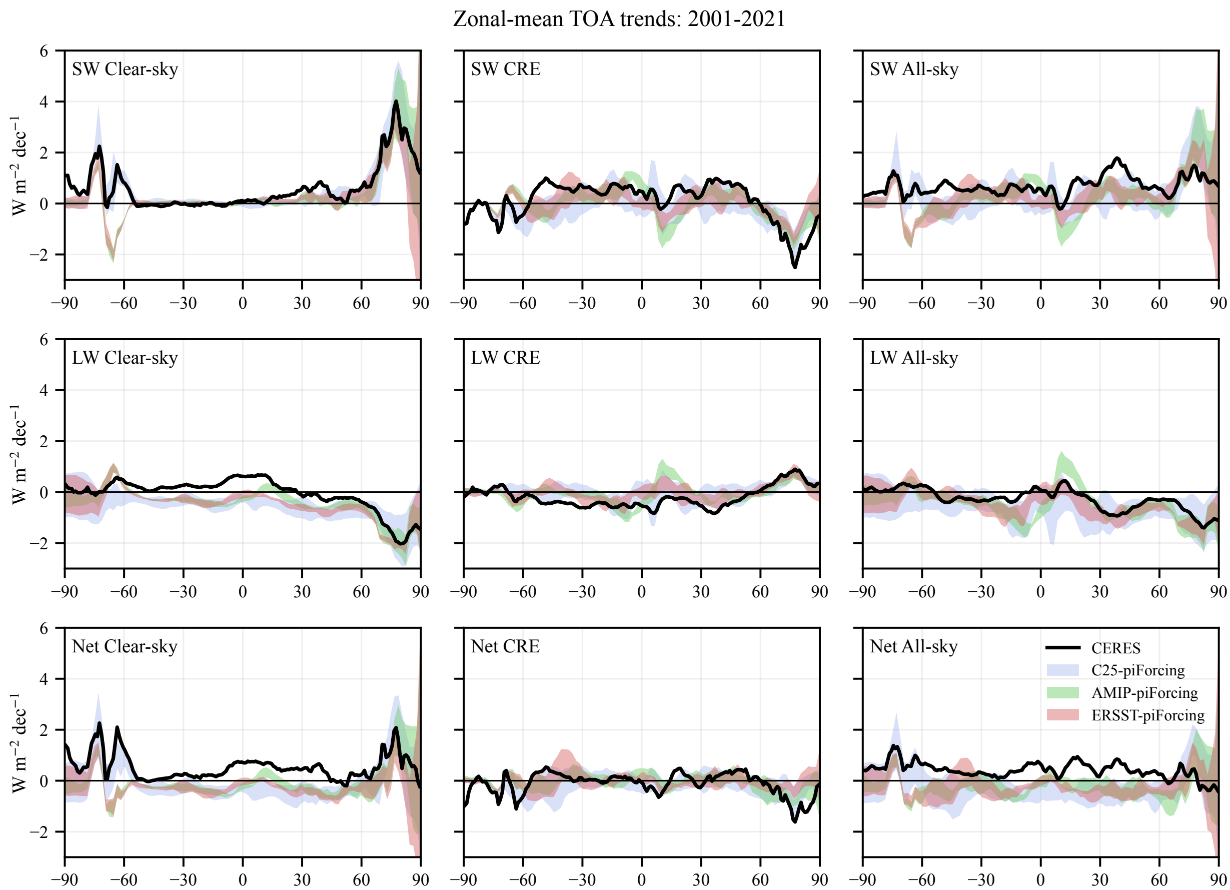

FIG. S5. **Zonal-mean trends in TOA radiation from CERES and *piForcing* simulations in CAM5 over 2001–2021.** Note that CERES trends are expected to differ from *piForcing* trends because *piForcing* intentionally excludes the component of TOA radiation from radiative forcing. CERES measures $\Delta N = \Delta F + \lambda\,\Delta T$ whereas piForcing estimates only $\lambda\,\Delta T$. Trends are shown for shortwave (SW), longwave (LW), and net TOA radiation for clear-sky, cloud radiative effect (CRE), and all-sky conditions. Shaded regions show the full ensemble range from CAM5's *piForcing* simulations with SST/SIC from C25 (14 members), AMIP (5 members), and ERSST (5 members); note that ERSST uses AMIP's SIC. Fluxes are defined such that positive heats the Earth while negative cools. In this convention, Net = SW + LW, and all-sky trends equal the sum of clear-sky and CRE. Note there may be errors and/or drifts in CERES SW/LW CRE (Park and Soden 2026). CAM5 results are shown because CAM5 has *piForcing* simulations over 2001–2021 for C25, AMIP, and ERSST; comparisons are broadly similar with CAM4.

References

Brönnimann, S., Y. Brugnara, and C. Wilkinson, 2024: Early 20th century Southern Hemisphere cooling. *Climate of the Past*, **20 (3)**, 757–767, https://doi.org/10.5194/cp-20-757-2024.

Chan, D., and Coauthors, 2026: DCENT-I: A Globally Infilled Extension of the Dynamically Consistent ENsemble of Temperature Dataset. *Geoscience Data Journal*, **13 (2)**, 70 054, https://doi.org/10.1002/gdj3.70054.

Cooper, V. T., G. J. Hakim, and K. C. Armour, 2025: Monthly Sea Surface Temperature, Sea Ice, and Sea Level Pressure over 1850–2023 from Coupled Data Assimilation. *Journal of Climate*, **38 (19)**, 5461–5490, https://doi.org/10.1175/JCLI-D-25-0021.1.

Cornes, R. C., T. Cropper, and E. C. Kent, 2025: CLASSnmat version 2: monthly, global, gridded night marine air temperature data. *NERC EDS Centre for Environmental Data Analysis*, https://doi.org/10.5285/306246329ae04eb3b2299446d911530a.

Forster, P. M., and Coauthors, 2025: Indicators of Global Climate Change 2024: annual update of key indicators of the state of the climate system and human influence. *Earth System Science Data*, **17 (6)**, 2641–2680, https://doi.org/10.5194/essd-17-2641-2025.

Meng, Z., G. J. Hakim, and E. J. Steig, 2025: Coupled Seasonal Data Assimilation of Sea Ice, Ocean, and Atmospheric Dynamics over the Last Millennium. *Journal of Climate*, **38 (23)**, 7229–7247, https://doi.org/10.1175/JCLI-D-25-0048.1.

Morice, C. P., and Coauthors, 2025: An observational record of global gridded near-surface air temperature change over land and ocean from 1781. *Earth System Science Data*, **17 (12)**, 7079–7100, https://doi.org/10.5194/essd-17-7079-2025.

Park, C., and B. Soden, 2026: Reconciling Discrepancies Between Observed and Model-Simulated Cloud Radiative Trends and Their Implications for Earth's Energy Imbalance. *Research Square*, https://doi.org/10.21203/rs.3.rs-9054442/v2.

Sippel, S., and Coauthors, 2024: Early-twentieth-century cold bias in ocean surface temperature observations. *Nature*, **635 (8039)**, 618–624, https://doi.org/10.1038/s41586-024-08230-1.

Stiller, D., and G. J. Hakim, 2026: Top-of-atmosphere radiation over the last millennium reconstructed from proxies. *arXiv*, https://doi.org/10.48550/arXiv.2510.09896.